

Beamforming for 3D Transesophageal Echocardiography

Bundelvorming voor 3D transoesofagale echocardiografie

Deep Bera

2018

Colophon

Deep Bera

Beamforming for 3D Transesophageal Echocardiography

Thesis, Erasmus Medical Center
June 12, 2018.

ISBN 978-94-028-1034-9

All rights reserved. No part of this publication may be reproduced, stored in a retrieval system, or transmitted, in any form, or by any means, electronic, mechanical, photocopying, recording, or otherwise, without the prior consent from the author, or when appropriate, from the publishers of the publications.

© 2018, D. Bera except for the following chapters:

Chapter 2, 4: ©2014 IEEE

Chapter 3, 6: ©2017, 2018 Institute for Physics and Engineering in Medicine (IPEM)

Cover designed by: Ilya Skachkov

Printed in the Netherlands by IPSKAMP Printing

For a printed version please contact:

Secretary Biomedical Engineering (June 2018: room Ee 2302)

Erasmus Medical Center

P.O. Box 2040

3000 CA Rotterdam

the Netherlands

Beamforming for 3D Transesophageal Echocardiography

Bundelvorming voor 3D transoesofagale echocardiografie

Thesis

to obtain the degree of Doctor from the
Erasmus University Rotterdam
by command of the
rector magnificus

Prof.dr. H.A.P. Pols

and in accordance with the decision of the Doctorate Board.

The public defence shall be held on
Tuesday 12 June 2018 at 09.30 hrs

by

Deep Bera
born in Kolkata, India

Doctoral Committee

Promotors: Prof.dr.ir. N. de Jong
 Prof.dr.ir. A.F.W. van der Steen

Other members: Prof.dr. A.J.J.C. Bogers
 Prof.dr. J. D'hooge
 Prof.dr. P. Tortoli

Co-promotors: Dr. ir. J.G. Bosch
 Dr. ir. H.J. Vos

The work described in this thesis was performed at the research group Biomedical Engineering of the department of Cardiology, Thorax center, Erasmus MC, the Netherlands. This work is part of the Open Technology Programme with project number 12405 which is (partly) financed by the Netherlands Organisation for Scientific Research (NWO).

Financial support by the Dutch Heart Foundation for the publication of this thesis is gratefully acknowledged

Financial Support



Contents

Chapter 1 Introduction	7
Chapter 2 Synthetic aperture sequential beamforming for phased array imaging	23
Chapter 3 Dual stage beamforming in absence of front-end receive focusing ...	33
Chapter 4 A Front-end ASIC with Receive Sub-Array Beamforming Integrated with a 32×32 PZT Matrix Transducer for 3-D Transesophageal Echocardiography	57
Chapter 5 Acoustic characterization of a miniature matrix transducer for pediatric 3D transesophageal echocardiography	85
Chapter 6 Multiline 3D beamforming using micro-beamformed datasets for pediatric transesophageal echocardiography	109
Chapter 7 Fast volumetric imaging using a matrix TEE probe with partitioned transmit-receive array.....	135
Chapter 8 Discussion and Conclusions	163
Summary	173
Samenvatting.....	175
Publications	177
Curriculum Vitae	179
Acknowledgment	181
PhD Portfolio	185

Chapter 1

Introduction

Chapter 1

The work in this thesis concentrates on 3D imaging techniques suitable for a miniaturized transducer designed for pediatric transesophageal echocardiography (TEE). Hence, this chapter focuses on the related background and clinical applications of such a transducer.

1.1. The heart

The heart is a muscular pump that circulates the blood through the human body. It consists of four chambers: the left and right atria (LA and RA) and the left and right ventricles (LV and RV) as shown in Figure 1(a). The blood with low oxygen concentration is collected from the body in the RA. The tricuspid valve (TV) is positioned between the RA and RV and prevents backflow of blood from the RV to the RA. From the RA the blood is passed to the RV. The RV transports this blood to the pulmonary system through the pulmonary valve and the pulmonary artery. After oxygenation in the lungs, the blood flows to the LA through the pulmonary veins. From the LA, this blood flows through the mitral valve (MV) to the LV, which pumps the oxygenated blood into the systemic circulation via the aortic valve.

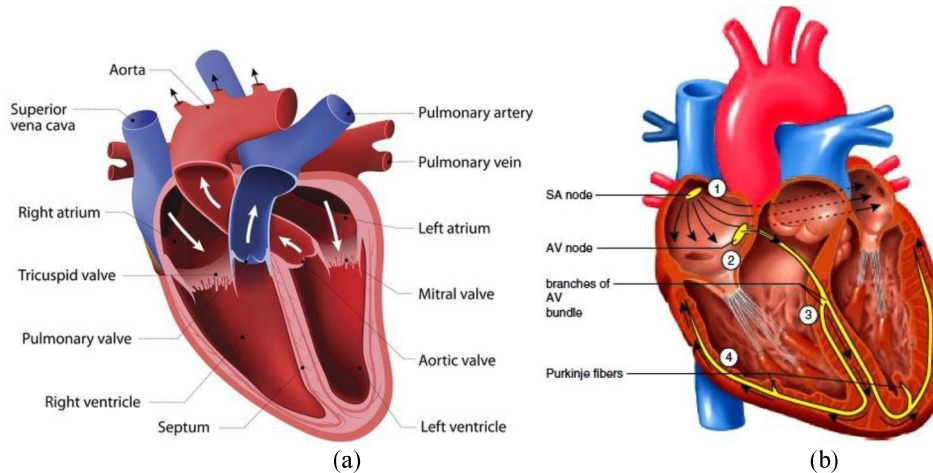


Figure 1: The heart and its electrical conduction path. (a) the structures of the heart [https://bodytomy.com/how-does-heart-work] and (b) the electrical conduction path from SA node to the Purkinje fibers fiber [http://encyclopedia.lubopitko-bg.com/Physiology_of_the_Heart.html].

The heart generates its own rhythm using the conduction system that conducts the electrical signals necessary for coordinated contraction of the atria and ventricles. As shown in Figure 1(b), the main components of the cardiac conduction system are the sinoatrial (SA) node, atrioventricular (AV) node, bundle of His, bundle branches, and Purkinje fibers. The cardiac rhythm is determined by a group of pacemaker cells in the SA node. These cells generate an electrical signal that spreads across the atria. In response to this signal, both the LA and RA contract and pump the blood into the ventricles. This electrical signal then travels from the AV node, through the bundle of His, down the bundle branches, and through the Purkinje fibers, stimulating the ventricles to contract. In response to the electrical signal conducted by these fibers, the cardiac muscle cells contract in a coordinated manner to efficiently pump the blood out of the ventricles into the pulmonary and systemic circulation [1].

1.2. Cardiovascular disease

Cardiovascular disease (CVD) is an umbrella term that includes a complete range of diseases related to the heart and the blood vessels. A distinction can be made between acquired and congenital CVD. The most important acquired CVDs include atherosclerosis, degenerative valvular disease, rheumatic heart diseases and arrhythmias [2]. Congenital CVD is characterized by structural cardiovascular defects.

In all CVD, echocardiography plays a key role; not only to diagnose a specific disease but also to check the progression of disease, and for support of interventional procedures.

1.2.1. Atrial Fibrillation

One of the predominant atrial arrhythmias is atrial fibrillation (AF), characterized by an uncoordinated electrical activity of the atria. In presence of AF, the conduction does not follow the established pathways from SA node to the AV-node anymore. This causes an irregular cardiac rhythm. At present, AF is the most prevalent arrhythmia across the world. More than 2.5 million American adults and 4.5 million people in the European Union (EU) are affected by AF [3]. Patients with AF account for approximately one-third of hospitalizations for cardiac rhythm disturbances in both the USA and the EU [3]. Therefore, AF has become a considerable challenge to the modern healthcare system.

Presently, transesophageal echocardiography (TEE) plays an important diagnostic role in certain stages of the treatment of patients with AF. In several studies, TEE has proven to be useful in determining the presence of thrombus in patients with the requirements of rapid cardioversion of AF or RF-ablation, especially in situations when the patient is found to be underanticoagulated or at high risk for stroke [1].

1.2.2. Congenital Heart Disease

Congenital heart diseases (CHDs) are problems of the heart's structure that are present at the time of birth. Every year, more than 32,000 children in the USA and approximately 36,000 children in the EU are born with CHD [4], [5]. Therefore, an improvement in CHD diagnosis and treatment procedure will have a significant impact on the healthcare system.

Patients with CHD may need medication, surgery, or cardiac catheter intervention to reduce the effects of and/or repair the defects. In CHD patients, TEE has shown to be very useful for assessment of the often very complex, abnormal 3D anatomy prior to and during cardiac surgery or intervention [1]. Since these surgeries often need to be performed at a very young age or even directly after birth, pediatric TEE probes need to be smaller in size than adult TEE probes.

Chapter 1

1.3. Ultrasound imaging

In medical ultrasound imaging, high-frequency sound waves are used to view organs inside the body. Generally, in ultrasound imaging, an acoustic wave propagates through the body and reflects back from several tissue boundaries and scattering tissues. These reflected sound waves also known as echoes represent (changes in) the acoustical properties (e.g. density) of the medium and thus, they contain information about both the depth and physical properties of the reflectors.

The use of ultrasound in medicine started during the Second World War in 1942 by K. T. Dussik [6]. After that, medical ultrasound imaging was further developed in various centers around the world. There are three classical ways to display ultrasound echoes: A-mode, M-mode and B-mode. In A-mode (amplitude mode), the scanning is performed using a single transmission and reception along a scanline and the receive amplitudes are plotted as a graph with respect to the depth. In B-mode (brightness mode), the echo amplitude per position is shown as a pixel brightness. This allows to form a 2D image of organs by sweeping the scanlines over the region. For live imaging, the image is continuously updated for the defined imaging region. Thus, it can show the movement of the body's internal organs. In M-mode (motion mode), along one chosen scanline, the movement of structures over time is represented as a continuous image.

With ultrasound, we can also measure and image the velocities of blood and tissues. This is called Doppler ultrasound. It employs the Doppler effect: A moving reflector causes a shift in the frequency of the reflected ultrasound. This shift can be measured and presented in several ways, e.g. as an audible tone, a spectrum or a color overlay in the image. It is widely used for visualizing blood flow, and important in assessing valves, flow abnormalities, obstructions, septal defects etc.

1.4. Ultrasound transducer

A transducer is a device that transforms energy from one form to another. An ultrasound transducer typically contains one or more piezoelectric elements that convert electrical energy into acoustic energy and vice versa. A piezoelectric material (such as Lead Zirconate Titanate or PZT) produces electrical signals when a mechanical force (strain) is applied to them. The produced voltage is proportional to the applied force and changes sign with it. It also exhibits the converse effect: it contracts and expands when positive and negative voltages are applied to it. This vibration in PZT elements produces an acoustic wave in the surrounding medium. In medical ultrasound imaging, ultrasound transducers are used to generate acoustic waves and to detect the waves scattered by the tissue.

1.4.1. Characteristics of the sound field of a transducer

A transducer has a natural resonance frequency that is determined by the thickness of the PZT elements. The resonance frequency of a transducer is the frequency at which the energy-conversion efficiency of the transducer is maximum. The frequency response of a piezoelectric ultrasound transducer has a band-pass shape. The bandwidth determines the range of frequencies over which the transducer can operate with relatively high energy conversion efficiency.

An ultrasound wave is characterized by its wavelength (λ) given by

$$\lambda = c/f \quad (1)$$

where f is the frequency at the source and c is the wave propagation speed in the medium. The wave propagation speed in soft tissues is about 1540 ms^{-1} .

Figure 2 shows the amplitude of the pressure field when a disk transducer vibrates at a single frequency. The sound field of a transducer is divided into the near field and the far field. In the near field, i.e. close to the transducer, the echo amplitude shows many maxima and minima due to interference effects of waves originating in different sections of the transducer surface. At a sufficient distance, all these partial waves start to sum coherently and form a strong maximum. This point is called the natural focus of the transducer. The distance between the transducer and the natural focus is known as the near field distance or focal distance (F). The area beyond F is called the far field. In the far field, as we move further from the transducer the sound field pressure gradually decreases to zero. The near field distance F is given by

$$F = D^2/4\lambda \quad (2)$$

where D is the element diameter, and λ is the wavelength.

The sensitivity of a transducer is determined by the beam diameter at the point of interest. The smaller the beam diameter, the greater the amount of reflected energy. The -6 dB pulse-echo beam diameter (BD) by

$$BD(-6 \text{ dB}) = 1.02Fc/fD \quad (3)$$

where f is the center frequency of the transducer.

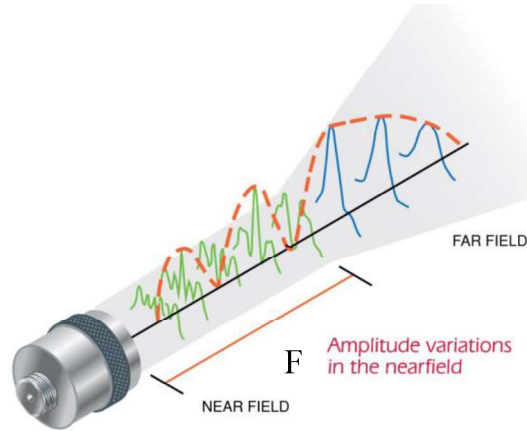


Figure 2: The near field and the far field of the sound field pressure generated from a disk transducer. Courtesy of Olympus.

Every transducer has a beam spread. Figure 3 gives a simplistic view of a sound beam for a disc transducer. The sound beam is narrow in the near field and focus and gets wider in the far field. The - 6 dB pulse-echo beam spread angle (α) is given by

$$\alpha/2 = \sin^{-1}(0.514cf/D) \quad (4).$$

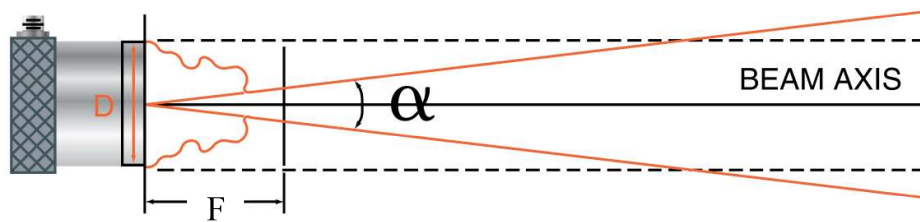


Figure 3: Pulse-echo beam spread for a disc transducer. Courtesy of Olympus.

1.4.2. 1D arrays

For creating a sharp (narrow) beam, a relatively large transducer diameter is needed. Such a single-element transducer generates a beam with a fixed direction and fixed focus. For beam steering/scanning, the transducer would need to be moved (translated/rotated) mechanically, which is impractical and slow. Hence, most medical transducers contain an array of small elements that offer the potential for electronic steering focusing. A very small single element transducer (compared to the ultrasound wavelength) will act as a point source (and detector).

Introduction

Beam spread angle for such a transducer will be very wide. A transducer with an array of small elements can be electronically steered and focused by appropriately delaying the transmit excitations and the received signals. Array transducers provide variable focusing and aperture control facilitating far better imaging than fixed-focus single-element transducers. In medical imaging, generally, there are three types of 1D arrays: linear array, phased array and curved linear array.

A linear array has a large footprint and contains hundreds of relatively large elements ($\geq \lambda$). It generates parallel beams with no or minimal steering. As shown in Figure 4(a), the linear array produces rectangular images almost as wide as the physical size of the transducer. This type of transducers provides a good overall image quality and is mainly used for imaging shallow organs and vessels. A phased array transducer is relatively smaller in footprint and contains relatively small elements ($< \lambda/2$). As depicted in Figure 4(b), the phased array performs sectorial scanning producing a pie-shaped image. The main difference between linear array imaging and phased array imaging is the steering of the beam. A common application for this type of arrays is cardiac imaging, which requires a smaller footprint of the transducer to fit in the spaces between the ribs (intercostal spaces). Despite the small physical size, phased array transducers can image a large region within the body. A curved linear array can be seen as a linear array on a curved surface. This type of transducers realizes the advantage of a larger angular image sector without the need for electronic steering. As shown in Figure 4(c), a curved linear array performs a line sequencing similar to a linear array, except that its physical curvature guides the scanlines into different angular directions. This type of arrays is useful in fetal imaging, or imaging internal organs such as the liver and kidney.

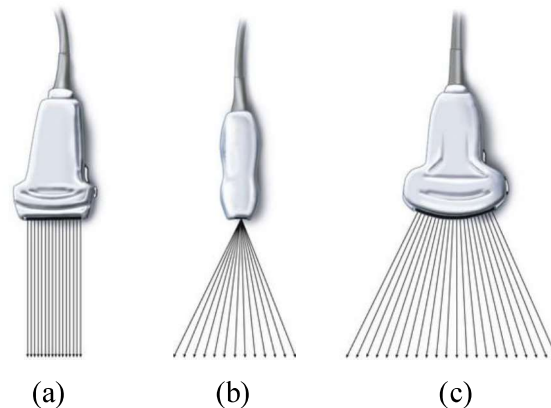


Figure 4: Different 1D arrays: (a) Linear array, (b) Phased array and (c) Curved linear array. [<https://aneskey.com/ultrasound-guided-regional-anesthesia/>]

1.4.3. General beamforming for B-mode imaging

Beamforming refers to the different techniques used to organize the many signals of the individual elements of an array transducer into time sequences of coherent echoes (beams) for creating each image line. Classically, this involves delaying and summing element signals to align the signals for different points in space. In B-mode ultrasound imaging, typically, static

Chapter 1

focusing is used for transmitting and dynamic focusing is applied in receive. In order to produce a scanline that is focused at all depths in receive, receive delays are dynamically adjusted before summing. Consequently, a 2D image is generated by repeating the above steps and combining the scanlines collected from different directions.

As illustrated in Figure 5, in transmit beamforming, a signal generator sends a high-frequency pulse to all the elements of an array. Each element has an associated delay circuitry to add an adjustable delay to the pulse. The delays are chosen such that the ultrasound waves emitted from each element simultaneously arrive at the focal point. In receive beamforming, the principle of focusing is exactly the same, only the process is reversed. The reflected pressure waves are delayed in such a way that the signals originating from a focal point are aligned. The aligned signals are then summed to produce the scanline focused at that particular point. This beamforming technique is called Delay-and-Sum (DAS) beamforming. For dynamic focusing, this process is performed for several points at different depths within the region of imaging.

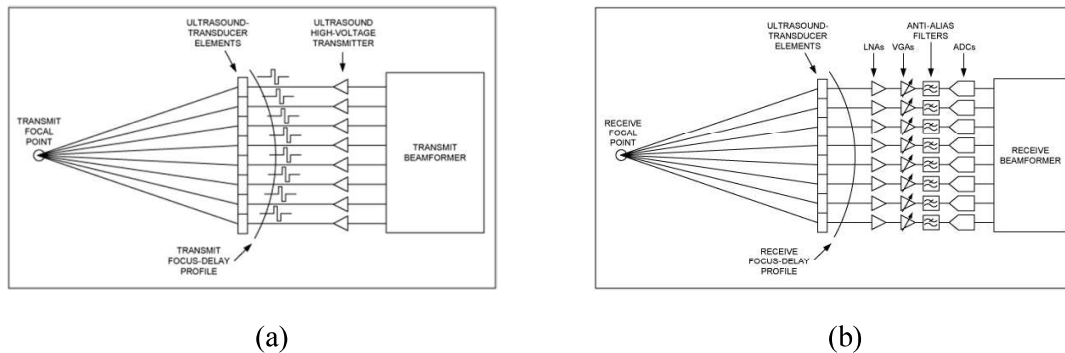


Figure 5: Illustration of beamforming: (a) transmit beamforming and (b) receive beamforming.
Courtesy of Maxim Integrated.

1.4.4. 3D imaging and 2D arrays

One of the drawbacks of 2D ultrasound imaging is that it demands skill and experience to acquire good quality images. In 2D imaging, one has to keep track of the spatial relationships in the anatomy and perform mental 3D reconstruction during an exam. The primary goal of 3D ultrasound imaging is to provide a direct 3D representation of the complex anatomy, together with a user-friendly presentation of the volumetric image with real-time interactive capabilities to examine anatomical structures of interest in any arbitrary plane or section. Thereby, 3D imaging has higher probability of finding an abnormality than 2D imaging.

For moving organs like the heart, real-time 3D imaging (also called 4D imaging) is required to capture the 3D motion of the heart chambers and valves. Real-time 3D imaging requires a 2D array which can acquire a volume of data rapidly using electronic focusing and steering in two

Introduction

orthogonal directions without moving the array.

Unlike 1D arrays, for 2D arrays (as shown in Figure 6), the ultrasound beams can be focused and steered in both lateral and elevation direction. A 2D array can be seen as an extension of the classical 1D array to both lateral and elevation directions. In a 2D array, small PZT elements are aligned on a regular grid in both lateral and elevation direction. Hence, the 2D arrays can produce volume images with uniform resolution in both the directions. A 2D array equivalent of a 1D array of 100 elements contains $100 \times 100 = 10,000$ elements. Consequently, connecting individual elements to control the ultrasound beam patterns becomes challenging as the number of channels in most of the present ultrasound scanners is not more than 256. Additionally, the realization of interconnect circuitry for such 2D arrays is cumbersome. This thesis addresses some of the possibilities to tackle this challenge by channel reduction.

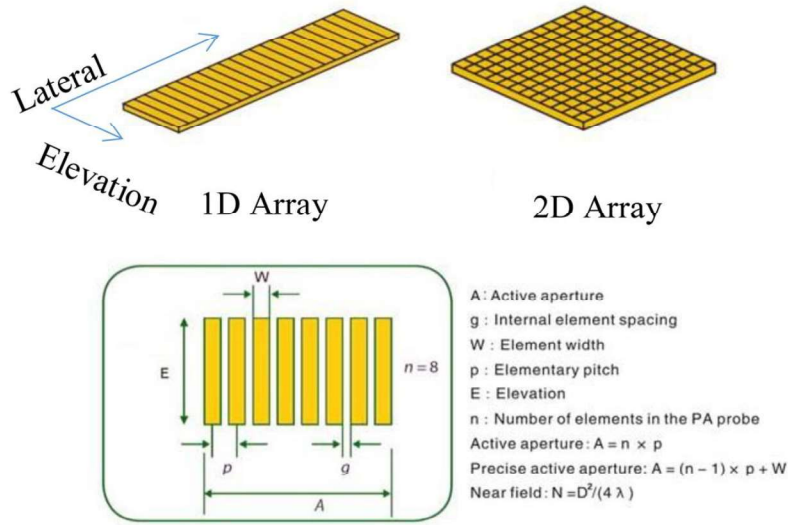


Figure 6: Structures of 1D and 2D transducers. Courtesy of Honesdom International (HK) Limited.

1.5. Echocardiography

Echocardiography (also called cardiac ultrasound) uses ultrasound for real-time imaging of the heart's chambers/walls (LA, RA, LV and RV), valves (MV, aortic valve etc.), and the blood vessels (aorta, vena cava, pulmonary artery and veins) connected with the heart. In 1953, I. Edler and C. H. Hertz were the first to observe heart wall motion [7] using A-mode scanning. Since then echocardiography as a technique has significantly evolved. The echocardiographic images show not only the size and shape of the heart and its components but also help the doctors to assess the heart's performance both qualitatively and quantitatively (by measuring chamber dimensions, cardiac output, ejection fraction, wall thickening etc.). The echo can also

Chapter 1

help in locating the areas of myocardium with poor contractility because of poor blood flow or injury from a previous heart attack. Additionally, echo images can effectively show possible blood clots inside the heart, fluid buildup inside the pericardium and many other cardiac problems. Hence, over the past decades, echo has become an indispensable diagnostic tool for cardiac examinations on patients suffering from CVD as well as for healthy subjects.

1.5.1. Transthoracic Echocardiography vs Transesophageal Echocardiography

Typically, there are two types of echocardiography routinely performed in the clinic: transthoracic echocardiography (TTE) and transesophageal echocardiography (TEE). In TTE, an ultrasound transducer is placed on the chest wall [as shown in Figure 7(a)] and the imaging of the heart is performed through the acoustic window in between the ribs of a patient. Images produced by TTE may suffer from poor quality because of the limited acoustic window and reflections or attenuation from the skin, ribs, lungs and fat, especially for obese patients. Additionally, in TTE, because of the large distance of the heart from the skin, the ultrasound signals are attenuated.

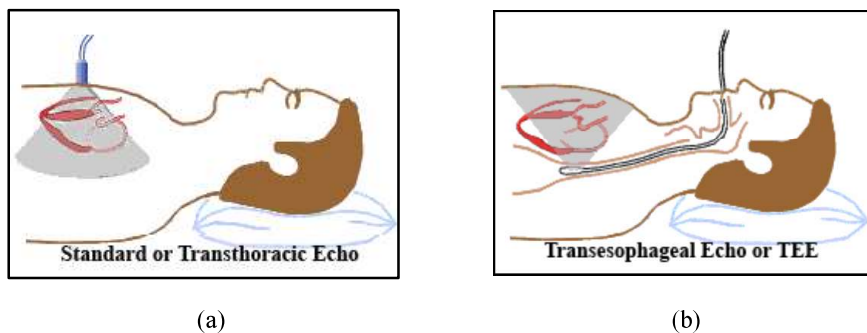


Figure 7: Two types of Echocardiography: (a) Transthoracic Echo and (b) Transesophageal Echo [<http://www.heartsite.com/html/tee.html>].

Unlike TTE, in TEE, a transducer is mounted on the tip of a gastroscopic tube and inserted via the mouth into the patient's esophagus to image the heart from there [as shown in Figure 7(b)]. Consequently, images produced by TEE are not deteriorated by the skin, fat, or ribs. Moreover, as the esophagus is located only a few millimeters away from the heart, the received ultrasound signals in TEE are not as attenuated as in TTE. Because of this lesser distance to be traversed, TEE can use a higher frequency than TTE and can produce images with better axial resolution. TEE, therefore, produces a superior image quality to TTE, especially for cardiac structures such as the aorta, pulmonary artery, valves, atria, atrial septum, appendages and even the coronary arteries.

Despite TTE being the keystone of diagnostic cardiac ultrasound, there are a number of clinical conditions where TEE is more valuable and more commonly used. At present, TEE is most

Introduction

commonly performed to evaluate endocarditis, native valvular disease, the cardiac source of embolism, prosthetic heart valve dysfunction, aortic dissection or aneurysm [1]. In addition, TEE is performed to evaluate left atrial appendage (LAA) clots in patients with AF [1]. In many cardiac surgical procedures, e.g. CHD or valve repair, TEE is performed both to verify the preoperative diagnosis and to monitor the success of repair [1]. Moreover, TEE is now commonly used as an intraoperative image guidance tool in combination with X-ray fluoroscopy, during several cardiac interventions including cardioversion, catheter ablation and prosthetic valve replacement, which are required for patients with AF and CHD [1].

1.5.2. MicroTEE

Recently, the microMulti TEE transducer (μ TEE) from Oldelft Ultrasound, Delft, The Netherlands [8] was introduced, primarily for neonatal and pediatric patients [shown in Figure 8 (a)]. The μ TEE probe has a phased array comprising of 32 elements. This probe can generate 2D images with an opening angle of 90° . The probe has proven to be very useful for performing 2D TEE in pediatric patients mainly because of its small size and excellent image [8]–[10]. Moreover, because of its small size, this probe is also very useful for monitoring adults undergoing minimally-invasive interventions, e.g. catheter ablation for atrial fibrillation and atrial septal defects, without sedation [11], [12]. Additionally, the μ TEE probe is useful for diagnosing hemodynamically unstable patients both in routine preoperative cases and in postoperative critical care [13].

1.5.3. 3D TEE

For 3D TEE in adults, there are a number of commercially available matrix array TEE probes (X7-2t from Philips Ultrasound, Bothell, WA [14], V5M TEE from Siemens Healthcare GmbH, Erlangen, Germany [15], and 6VT-D from General Electric Healthcare, Amersham, U.K. [16]). These matrix TEE probes are capable of real-time acquisition and live 3D display. However, they are much larger in size than the μ TEE probes and therefore cannot be used in pediatric patients. Also, without full anesthesia, they are not suitable for long-term monitoring in adults due to patient discomfort, whereas a transnasal insertion of the μ TEE probe has shown to be tolerated by patients for up to 24 hours [17], [18]. Therefore, if a matrix TEE probe with similar dimension to the μ TEE probe was available, it could be used both as a pediatric 3D TEE probe as well as a transnasal adult 3D TEE probe for long-term monitoring.

Several studies have shown that real-time 3D imaging is more beneficial than 2D imaging in most cardiac conditions [19], [20] because of its superior visualization of different 3D structures in the heart. Even though the μ TEE probe is very useful for real-time 2D imaging, it is incapable of performing real-time 3D imaging on the heart. It should be noted that it is possible to reconstruct a 3D image from 2D TEE images (also for the μ TEE probe) by rotating the imaging plane and recording over many heart cycles, but that procedure requires offline processing of sequential acquisitions gated to ECG [21]. These lengthy acquisitions and the

Chapter 1

post-processing of the acquired data increase the duration of the examination and also suffer from radial artifacts [22]. Therefore, it does not meet the needs for real-time 3D imaging.

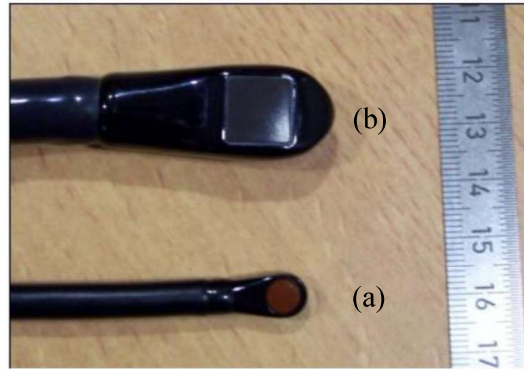


Figure 8: Two kinds of TEE probes: (a) Philips X7-2t, adult matrix TEE probe and (b) microMulti TEE probe from Oldelft

1.6. Challenges in real-time 3D imaging

There are primarily two challenges related to real-time 3D imaging using matrix array probes. The first challenge is to connect a huge number of elements (>1000) to the limited number of transmit/receive channels (max. 256) of the ultrasound scanner. The second challenge is to achieve adequately high volume rate. These two challenges are interrelated. The first challenge can be addressed in several ways such as by using sparse arrays, channel multiplexing and micro-beamforming (sub-array beamforming). Sparse arrays, in general, produce poor image quality, whereas channel multiplexing reduces the achievable volume rate. A 3D beamforming using micro-beamformers is a two-stage procedure. In the first stage, to achieve steering, the matrix array is sub-divided into groups of N neighboring elements called sub-arrays and micro-delays are applied to the signals received by the individual elements, before summing them. Thus, in the first stage, each sub-array produces a partially beamformed or micro-beamformed (also called pre-steered) RF signal, and thereby, achieves a factor of N reduction in channel count. This micro-beamforming step is typically performed within a front-end ASIC. In the second stage, traditional DAS digital beamforming is performed on these received micro-beamformed or pre-steered RF datasets by an external ultrasound system to produce final 3D volumes with dynamic receive focusing (DRF). Thus, this approach with micro-beamforming or sub-array beamforming [23], [24] reduces the receive channel count while maintaining the image quality and frame rate.

One other possibility for channel reduction is using synthetic aperture sequential beamforming [25], a dual-stage beamforming technique. In the first stage of this technique, instead of transferring the entire raw channel data received by individual elements, only a partially

beamformed (with fixed focusing in both transmit and receive) low resolution image (LRI) is transferred to an ultrasound system. In the second stage, DAS beamforming is applied on the LRI to produce the final high resolution image (HRI). In this way, dual-stage beamforming reduces both the channel count and the amount of data transfer. Although dual stage beamforming is very useful for 2D imaging using 1D linear or phased array transducers, its application to 3D imaging with matrix transducer is limited, mainly because of its requirement of a large number of transmissions. In 3D imaging, this will lead to a low volume rate.

The second challenge has been addressed since the beginning of 3D imaging by parallel beamforming [26]. Unlike conventional imaging, where each receive line is produced from a single transmission, in parallel beamforming, multiple receive lines are produced from a single transmit. Hence, an image or volume is reconstructed from a lower number of transmissions. Although parallel beamforming as proposed in [26] is suitable for achieving a high volume rate, it suffers from poor image quality for several reasons. The first reason is that it uses wide transmission beams for covering the extra scanlines, thereby producing images with a wider point spread function (PSF). Unfortunately, this is intrinsic to parallel beamforming as the resulting pulse-echo beam is a product of both the wide transmit beam and the receive beam. The second reason for poor image quality is that the scanlines that are co-aligned with transmit beams have the highest intensity, whereas the scanlines far from the transmit directions have decreased intensity. Thus, volumes produced using parallel beamforming suffer from amplitude variations. The third reason is that the scanlines from one transmission show higher correlation among themselves than scanlines from neighboring transmissions. This dependence on the transmit beam leads to an imaging artifact of sharp intensity changes at the transition between the scanlines from different transmissions. We refer to these artifacts as *crossover artifacts*. Until now, several approaches have been proposed to improve the image quality in parallel beamforming for 2D imaging using both linear array and phased array transducers by avoiding the latter two limitations [27], [28]. These results indicate that it is possible to improve the image quality in parallel beamforming by avoiding the crossover artifacts by combining the beamformed scanlines from neighboring transmissions.

1.7. Prototype of a miniaturized matrix array transducer for 3D TEE

We have recently designed and fabricated a miniaturized matrix transducer suitable for 3D TEE in pediatric patients as well as for transnasal use in adults for long-term monitoring. The prototype transducer consists of a receive aperture with an effective aperture area similar to the μ TEE ($5 \times 5 \text{ mm}^2$) and a very small central transmitter ($1.2 \times 1.2 \text{ mm}^2$) capable of producing wide transmit beams. It is integrated on an ASIC for applying micro-beamforming to pre-steer the receive beams in 3D space. Thus, the micro-beamformers help in connecting the required elements (~ 1000) using a limited number of cables (~ 130) that can fit in the gastroscopic tube and can be connected to any ultrasound system.

Chapter 1

1.8. Aim of this thesis

None of the previously proposed parallel beamforming techniques is directly suitable for the prototype matrix transducer with such a transmitter-receiver layout and receive micro-beamformers. Therefore, the aim of this thesis was to develop and study 3D parallel beamforming techniques appropriate for the prototype transducer that can produce volumes with good image quality at a sufficiently high frame rate (>200 Hz) suitable for pediatric patients.

1.9. In this thesis

To explore the possibilities of reducing channel count and improving image quality, we first studied dual stage beamforming. In Chapter 2, we evaluate the advantages of dual-stage beamforming applied in phased array imaging. We found that dual stage beamforming significantly outperformed the conventional DRF in improving the lateral resolution in phased array imaging. Chapter 3 describes a simplified front-end architecture and a corresponding dual-stage beamforming for linear array imaging. This study showed that, even with a very simple front-end, the proposed dual-stage beamforming can attain an image quality better than conventional DRF. In Chapter 4, we describe a front-end ASIC of a miniaturized matrix transducer for real-time 3D TEE with a system architecture that is optimized for the requirements of a pediatric probe as well as a transnasal adult probe for long-term monitoring. The ASIC successfully met all the required functionalities of micro-beamforming, including the power budget of a TEE probe. The transducer fabrication and acoustic characterization are described in Chapter 5. The experimental results showed that a successful prototype transducer was manufactured with fully functional micro-beamforming and capability of real-time 3D imaging. In Chapter 6, we describe the study of multiline 3D beamforming using micro-beamformed datasets suitable for the prototype transducer comprising limited receive pre-steering capability. Chapter 7 describes the acoustic characterization of a newly designed prototype matrix adult TEE probe as well as a multiline 3D beamforming technique similar to that in Chapter 6 but adapted for the adult TEE probe. With this probe, we managed to perform real-time 3D volume acquisition in an in vivo experiment on the heart of a healthy adult pig. In Chapter 8 we discuss our findings from all these studies as well as future work regarding real-time 3D imaging using the prototype miniaturized matrix TEE transducer.

References

- [1] D. L. Mann, D. P. Zipes, P. Libby, R. O. Bonow, and E. Braunwald, Braunwald's Heart Disease: A Textbook of Cardiovascular Medicine, 10th ed. 2015.
- [2] World Organization. World Heart Federation. World Stroke Organization, "Global Atlas on Cardiovascular disease prevention and control," *Glob. atlas Cardiovasc. Dis. Prev. Control.*, 2011.

Introduction

- [3] Heart Rhythm Society, “Burden of AFib.” [Online]. Available: <http://www.hrsonline.org/News/Atrial-Fibrillation-AFib-Awareness>. [Accessed: 12-Jul-2017].
- [4] G. H. Baker, G. Shirali, J. M. Ringewald, T. Y. Hsia, and V. Bandisode, “Usefulness of Live Three-Dimensional Transesophageal Echocardiography in a Congenital Heart Disease Center,” *Am. J. Cardiol.*, vol. 103, no. 7, pp. 1025–1028, 2009.
- [5] H. Dolk, M. Loane, and E. Garne, “Congenital heart defects in Europe: Prevalence and perinatal mortality, 2000 to 2005,” *Circulation*, vol. 123, no. 8, pp. 841–849, 2011.
- [6] R. S. C. Cobbold, “Foundations of Biomedical Ultrasound,” Oxford University Press, 2007, pp. 437–450, 416.
- [7] I. Edler and C. H. Hertz, “The use of ultrasonic reflectoscope for the continuous recording of the movements of heart walls. 1954.,” *Clin. Physiol. Funct. Imaging*, vol. 24, no. 3, pp. 118–136, 2004.
- [8] S. C. Zybiewski *et al.*, “Initial Experience With a Miniaturized Multiplane Transesophageal Probe in Small Infants Undergoing Cardiac Operations,” *Ann. Thorac. Surg.*, vol. 89, no. 6, pp. 1990–1994, 2010.
- [9] T. V Scohy, “Peri-operative Anesthetic Innovations During Pediatric Cardiac Surgery,” Erasmus University, Rotterdam, 2011.
- [10] K. Pushparajah, O. I. Miller, D. Rawlins, A. Barlow, K. Nugent, and J. M. Simpson, “Clinical application of a micro multiplane transoesophageal probe in congenital cardiac disease,” *Cardiol. Young*, vol. 22, no. 2, pp. 170–7, 2012.
- [11] S. Stec, B. Zaborska, M. Sikora-Frc, T. Kryski, and P. Kuakowski, “First experience with microprobe transoesophageal echocardiography in non-sedated adults undergoing atrial fibrillation ablation: Feasibility study and comparison with intracardiac echocardiography,” *Europace*, vol. 13, no. 1, pp. 51–56, 2011.
- [12] M. Taniguchi, T. Akagi, Y. Kijima, H. Ito, and S. Sano, “Transcatheter closure of a large atrial septal defect under microprobe transesophageal echocardiographic guidance,” *Echocardiography*, vol. 29, no. 4, 2012.
- [13] C. E. Wagner, J. S. Bick, B. H. Webster, J. H. Selby, and J. G. Byrne, “Use of a miniaturized transesophageal echocardiographic probe in the intensive care unit for diagnosis and treatment of a hemodynamically unstable patient after aortic valve replacement,” *J. Cardiothorac. Vasc. Anesth.*, vol. 26, no. 1, pp. 95–97, 2012.
- [14] I. S. Salgo, “Three-Dimensional Echocardiographic Technology,” *Cardiology Clinics*, vol. 25, no. 2, pp. 231–239, 2007.
- [15] Siemens, “syngo fourSight TEE view.” [Online]. Available: <https://www.healthcare.siemens.com/ultrasound/options-and-upgrades/clinical-applications/syngo-foursight-tee-view>. [Accessed: 25-Jul-2016].
- [16] GE Healthcare, “Vivid™ E9 XDclear™,” 2013.

Chapter 1

- [17] P. Zimmermann, C. Greim, H. Trautner, U. Sagmeister, K. Kraemer, and N. Roewer, "Echocardiographic Monitoring During Induction of General Anesthesia with a Miniaturized Esophageal Probe," *Anesth. Analg.*, vol. 96, no. 1, pp. 21–27, 2003.
- [18] T. Szili-torok and J. G. Bosch, "Transnasal transoesophageal ultrasound : the end of the intracardiac echocardiography age ?," *Europace*, vol. 13, pp. 7–8, 2011.
- [19] M. Montealegre-Gallegos, F. Mahmood, K. Owais, P. Hess, J. S. Jainandunsing, and R. Matyal, "Cardiac Output Calculation and Three-Dimensional Echocardiography," *J. Cardiothorac. Vasc. Anesth.*, vol. 28, no. 3, pp. 547–550, 2014.
- [20] P. M. Kapoor *et al.*, "An update on transesophageal echocardiography views 2016: 2D versus 3D tee views," *Ann. Card. Anaesth.*, vol. 19, no. Supplement, pp. S56–S72, 2016.
- [21] N. G. Pandian *et al.*, "Multiplane transesophageal echocardiography. Imaging planes, echocardiographic anatomy, and clinical experience with a prototype phased array OmniPlane probe," *Echocardiography*, vol. 9, no. 6, pp. 649–666, 1992.
- [22] L. Sugeng *et al.*, "Real-Time Three-Dimensional Transesophageal Echocardiography in Valve Disease: Comparison With Surgical Findings and Evaluation of Prosthetic Valves," *J. Am. Soc. Echocardiogr.*, vol. 21, no. 12, pp. 1347–1354, 2008.
- [23] B. Savord and R. Solomon, "Fully sampled matrix transducer for real time 3D ultrasonic imaging," in *IEEE Ultrasonics Symposium*, 2003, vol. 1, pp. 945–953.
- [24] S. Blaak, C. T. Lancée, J. G. Bosch, C. Prins, A. F. W. Van Der Steen, and N. De Jong, "A matrix transducer for 3D transesophageal echocardiography with a separate transmit and receive subarray," in *IEEE Ultrasonics Symposium*, 2011, pp. 2341–2344.
- [25] J. Kortbek, J. A. Jensen, and K. L. Gammelmark, "Sequential beamforming for synthetic aperture imaging," *Ultrasonics*, vol. 53, no. 1, pp. 1–16, 2013.
- [26] D. P. Shattuck, M. D. Weinshenker, S. W. Smith, and O. T. von Ramm, "Explososcan: a parallel processing technique for high speed ultrasound imaging with linear phased arrays," *J. Acoust. Soc. Am.*, vol. 75, no. 4, pp. 1273–1282, 1984.
- [27] T. Hergum, T. G. Bjåstad, K. Kristoffersen, and H. Torp, "Parallel Beamforming Using Synthetic Transmit Beams," *IEEE Trans. Ultrason. Ferroelectr. Freq. Control*, vol. 54, no. 2, pp. 271–280, 2007.
- [28] L. Tong, A. Ramalli, R. Jasaityte, P. Tortoli, and J. D'Hooge, "Multi-Transmit Beam Forming for Fast Cardiac Imaging — Experimental Validation and In Vivo Application," vol. 33, no. 6, pp. 1205–1219, 2014.

Chapter 2

Synthetic aperture sequential beamforming for phased array imaging

*D. Bera, J.G. Bosch, N. de Jong, and H.J. Vos, "Synthetic Aperture
Sequential Beamforming for phased array imaging," in IEEE
Ultrasonics Symposium, 2015, pp. 1–4.
DOI: 10.1109/ULTSYM.2015.0499*

Chapter 2

Synthetic Aperture Sequential Beamforming (SASB) is adapted for phased array ultrasound imaging. The primary advantage of using SASB is an improved lateral resolution without storing the raw channel data which can be realized on ultrasound systems with a relatively simple front-end. The performance of the beamforming technique is evaluated with simulations in Field II and by off-line processing of phantom data using a commercial ultrasound scanner. Results show that the lateral resolution improved by 20% in comparison to conventional dynamic receive beamforming.

2.1. Introduction

Conventional ultrasound imaging systems utilize delay and sum (DAS) beamforming with fixed transmit focusing and dynamic receive focusing (DRF). For phased array imaging the transmit beams are steered in different angles, also with a fixed depth of focusing. Therefore, the lateral resolution is optimal only at the depth of transmit focus. Improvement of lateral resolution in phased array imaging can be achieved by phase coherence imaging as shown in [1]. In this technique coherence of the raw channel data is analyzed to exclude signals with off-axis scattering. Suppressing signals from off-axis directions can also be attained using adaptive apodization, based on minimum variance beamforming as proposed in [2]. These methods improve lateral resolution by reducing the side lobes and narrowing the main lobe at the expense of high computational overhead and data transfer. To improve lateral resolution and contrast, Synthetic Aperture Focusing Technique (SAFT) can also be used. In SAFT, many transmit-receive events are combined to synthesize a High Resolution Image (HRI) in which both the transmit and the receive fields are focused throughout the entire image [3,4]. However, SAFT generally involves a high computational load, data transfer and data storage. Therefore, implementation of such systems is highly challenging and costly. For SAFT with single-element transmit, the depth of penetration is also limited due to the low energy transmission. To solve this issue a multi-element SAFT was proposed in [3] where a focused transmission from multiple elements is used. Using these transmit focal points as virtual sources to improve lateral resolution was showed in [4]. The concept of virtual sources to improve lateral resolution was later explored in [5-8]. In all these techniques raw channel data is used to achieve an isotropic lateral resolution at different depths. Synthetic Aperture Sequential Beamforming (SASB) was introduced in [9] for linear array imaging to apply SAFT for achieving depth-independent lateral resolution without storing raw channel data, while avoiding complexity of implementation in the front-end of the ultrasound machine. SASB shows significant improvement in lateral resolution compared to conventional imaging using DRF.

SASB is a two-stage beamforming procedure. In the first stage, a single focal point for both transmit and receive is used to create a set of beamformed RF lines. The second stage combines information from multiple RF lines of the first stage and produces the final HRI considering the transmit and the receive focal points as virtual sources. This results in a dynamic transmit focus, leading to optimized lateral resolution and signal-to-noise ratio, and clutter reduction.

In this paper we have extended SASB to phased array imaging. We named it Phased array Synthetic Aperture Sequential Beamforming (PSASB). PSASB is evaluated using numerical simulations and measurement with a tissue mimicking phantom using a conventional ultrasound scanner.

Chapter 2

2.2. Method

In the first stage of PSASB a set of beamformed RF lines are obtained using a fixed depth of focus in both transmit and receive. Fig. 1 shows the ultrasound wave propagation path considered to compute the time-of-flight for transmission at an angle of θ_i in the first stage beamforming. The blue-shaded area represents a transmit wave field and the position of low resolution line is shown using a dashed red line. The delay for the receive element positioned at \vec{r}_r , with respect to the center of the transmit aperture (\vec{r}_t) can be represented as the round trip time-of-flight calculated as

$$t_d(\vec{r}_r) = \frac{1}{c} (|\vec{r}_{tf} - \vec{r}_t| \pm 2 \cdot |\vec{r}_{ip} - \vec{r}_{tf}| + |\vec{r}_r - \vec{r}_{tf}|) \quad (1)$$

where \vec{r}_{tf} is the transmit/receive focal point and \vec{r}_{ip} represents the image point on the low resolution line. The \pm sign in (1) depends on the position of the image point. If the image point is situated below the virtual source (transmit/receive focal point) then the delay has to be added, otherwise it has to be subtracted. The virtual source is presumed to transmit a spherical wave confined by the opening angle (α) of the transmitted wave field:

$$\alpha \approx 2 \arctan\left(\frac{L_a \cdot \cos \theta_i}{2r_{tf}}\right) \quad (2)$$

where L_a represents the physical width of the transmit aperture and r_{tf} is the depth of the virtual source. Because of the wide beam, many locations in the field can produce a scattering signal that will be projected onto the low-resolution image line. This is exemplified by the arc A in Fig.1, with center point r_{tf} , which represents the set of spatial positions of which the echoes are projected onto the low resolution line.

Fig. 2 shows the geometry of second stage beamforming with three consecutive focused transmit beams. The areas with blue shades represent the transmit wave fields and low resolution lines are shown using solid/dashed red lines. Each image point (shown as the blue dot in Fig. 2) is projected onto multiple low resolution lines (denoted by red dots in Fig. 2) lying on the white arc B in Fig. 2.

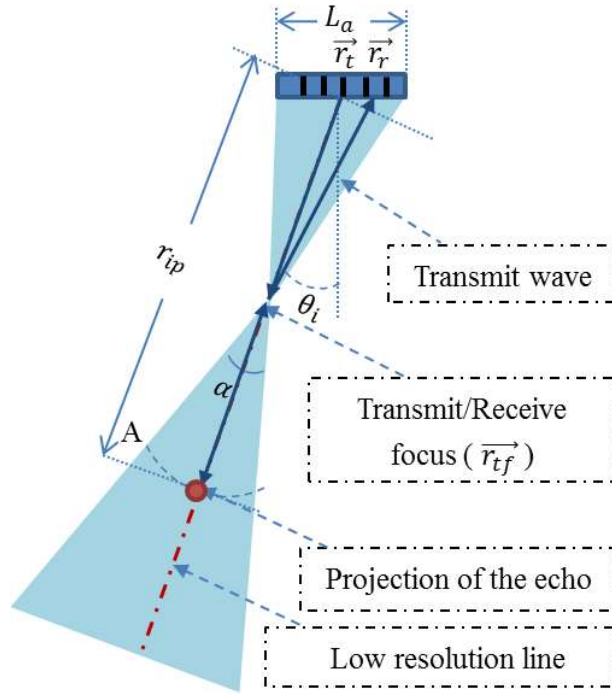


Figure 1: Sound wave propagation path to compute time-of-flight for a fixed focused transmit and receive in the first stage beamforming

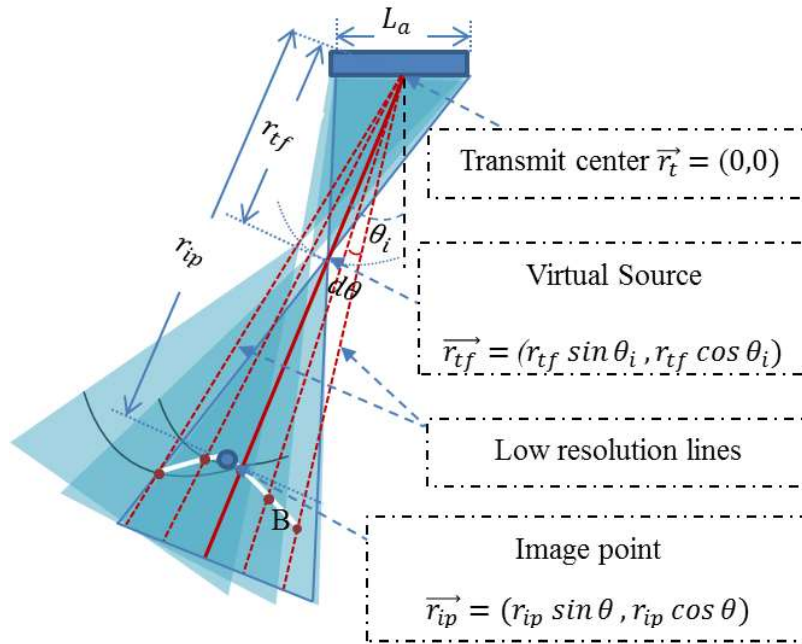


Figure 2: Geometry of three consecutive transmit beams used for time-of-flight and apodization weight calculation in second stage beamforming

In the second stage, high resolution points are formed by weighted summing of the points from

Chapter 2

multiple low resolution lines. A single high resolution point (*hrp*) at location \vec{r}_{ip} , is calculated as

$$hrp(\vec{r}_{ip}) = \sum_{n=-N/2}^{N/2} W(\vec{r}_{ip}, l_{\theta_n}) \cdot l_{\theta_n}(t_{d_n}(\vec{r}_{ip})) \quad (3)$$

where $l_{\theta_n}(t_{d_n}(\vec{r}_{ip}))$ is the sample at time t_{d_n} from the low resolution line l at an angle θ_n . The variable W is the apodization function for N low resolution lines and is chosen to be a Hanning window [9]. N is determined by depth (r_{ip}) of the *hrp* and the size of N is given by

$$N(r_{ip}) \approx 2 \cdot (\arctan \left[\frac{|r_{tf} - r_{ip}| \cdot \tan \frac{\alpha}{2}}{r_{ip}} \right]) / d\theta \quad (4)$$

where r_{tf} is the distance between the virtual source and the center of the aperture, α is the opening angle of the transmit wave field at the virtual source given by (2) and $d\theta$ is the angle between two consecutive transmit events. N is the size of the synthesized aperture of the PSASB technique at a certain depth. In (4) the value of N increases as the distance of the image point r_{ip} increases. However, N is limited by the number of low resolution lines from the first stage beamforming. Therefore, for high resolution points located far (both above and below) from the virtual source the size of synthesized aperture will not be able to increase any more. N decreases towards the lateral extremities of the image, caused by the limited physical aperture size of the transducer. Therefore, the best lateral resolution could presumably be achieved in the central region.

The time delay t_{d_n} with respect to the center of the transmit aperture \vec{r}_t for the contributory low resolution lines is found from the round trip time-of-flight,

$$t_{d_n}(\vec{r}_{ip}) = \frac{2}{c} (|\vec{r}_{tf} - \vec{r}_t| \pm |\vec{r}_{ip} - \vec{r}_{tf}|) \quad (5)$$

where \vec{r}_{tf} is the position of the virtual source. With reference to Fig. 2, the distances in (5) correspond to

$$|\vec{r}_{tf} - \vec{r}_t| = r_{tf} \quad (6)$$

and, for every

$$|\vec{r}_{ip} - \vec{r}_{tf}| = \sqrt{[r_{tf} \cdot \sin(\theta_n) - r_{ip} \cdot \sin \theta]^2 + [r_{tf} \cdot \cos(\theta_n) - r_{ip} \cdot \cos \theta]^2} \quad (7)$$

where $\{n \in \mathbb{Z} | -N/2 \leq n \leq N/2\}$ and θ is the angle of the high resolution image line in polar coordinates. Equation (7) represents the geometric distance between the image point and virtual source of the low resolution lines, fully analogous to SASB for linear arrays, but now expressed in polar coordinates as used in sector scanning.

2.3. Results

The performance of PSASB is investigated using FieldII [10] simulations and by off-line processing of data acquired with a Verasonics Vantage System (Verasonics Inc., Washington, USA) using a Philips ATL P4-1 phased array ultrasound probe (Philips Ultrasound, Washington, USA). The lateral resolution at different depths are compared with conventional B-mode imaging using fixed transmit focus and DRF. The numerical simulation is performed with a model of the phased array transducer with properties similar to the Philips ATL P4-1 probe which is used for the measurements (Table 1). Ten point scatters were positioned between 20mm to 100mm depth and -10mm to 10mm laterally.

Table 1: Default imaging parameters for the simulations and experiments

Parameters		Value
Sampling frequency in simulation		200 MHz
Centre frequency		2.5 MHz
Wavelength (λ)		0.6 mm
Pitch		$\lambda/2$
Number of elements		96
Excitation pulse		2 cycle sinusoid
First stage	Transmit focus	40 mm
	Transmit aperture	96
	Tx/Rx Apodization	Hanning
	Number of scan lines	128
	Scan angle	$\pm 45^\circ$
Second stage	Receive aperture	96
	Apodization	Hanning
	Number of scan lines	128

Fig. 3 shows the images with DRF and PSASB side by side for the configuration mentioned in Table 1 and Fig. 4 shows the quantified lateral resolution of these images. The transmit focus was 40 mm in both cases. The axial resolution is very similar for both, as this primarily depends on the spatial pulse length which is equal in all cases. The quantified lateral point spread function at -6dB (full width half maximum) for different depths show that PSASB consistently outperforms DRF in terms of lateral resolution, with a maximum reduction of the PSF of 25%.

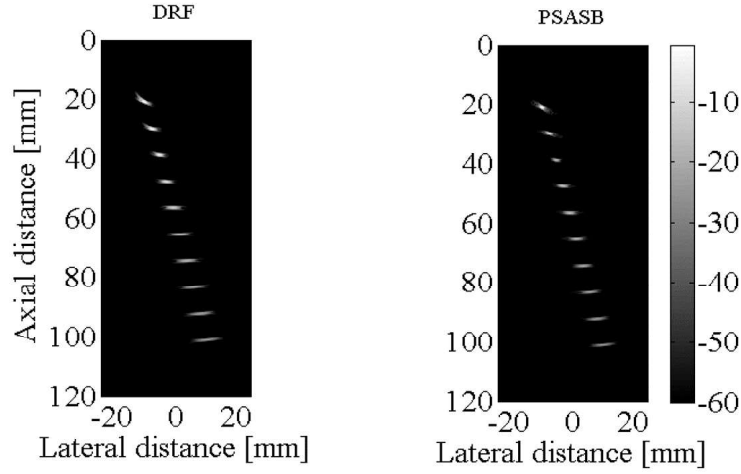


Figure 3: Conventional dynamic receive focusing image (left) and two-stage sequentially beamformed synthetic aperture image (right).

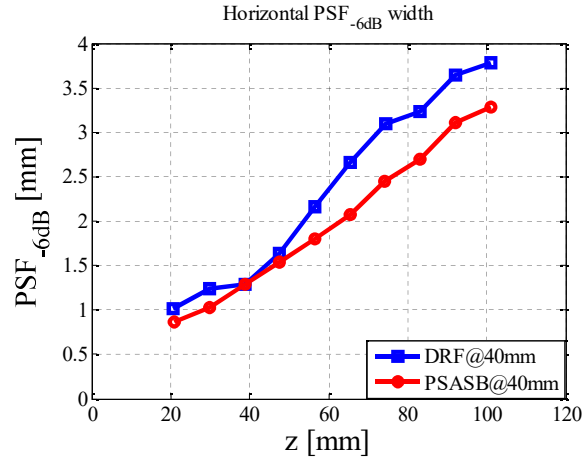


Figure 4: Quantified lateral width of the point spread function at -6 dB of the DRF and the PSASB images of Fig. 3, as function of depth.

In the experiments a tissue mimicking phantom (multi-purpose multi-tissue ultrasound phantom 040-GSE, CIRS, Virginia, USA) with 0.5 dB/MHz/cm attenuation and containing wire targets was used. DRF and PSASB along with envelope detection and log compression were done offline. A comparison of images produced by both methods is shown in Fig. 5 and the lateral PSF width in these images is quantified in Fig. 6. It is observed that at the center of the image PSASB produces improved lateral resolution over DRF, similar to the simulation results. PSASB has improved the -6dB width of the point spread function by 20% when compared to DRF throughout almost the entire depth.

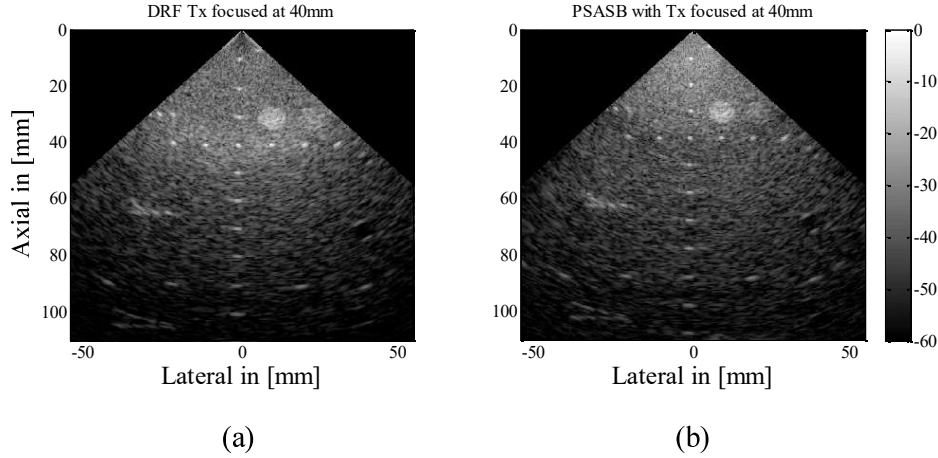


Figure 5: Image produced by a) Dynamic Receive Focusing and b) Phased array synthetic aperture sequential beamforming using a P4-1 phased array probe with a Verasonics Vantage ultrasound scanner. For both the cases transmit focus was at 40mm.

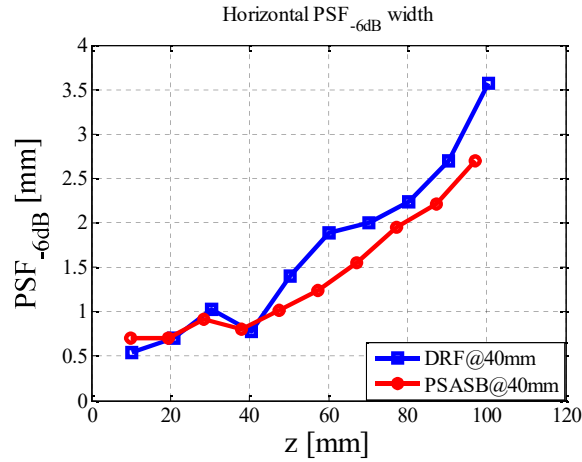


Figure 6: Quantified lateral resolution at -6dB for the above images

2.4. Conclusion

In this paper we successfully extended synthetic aperture sequential beamforming for phased array imaging. The PSASB technique has been examined using FieldII simulations and by off-line processing of data acquired using a commercial ultrasound scanner. Experimental and numerical experiments indicate that PSASB produces images with up to 25% better lateral point spread function than conventional DRF both in near and far field. Therefore, this technique is capable of yielding phased array images with better lateral resolution with limited acoustic front-end complexity and can be potentially useful for 3D/4D imaging.

Chapter 2

Acknowledgment

This research is supported by the Dutch Technology Foundation STW, which is part of the Netherlands Organization for Scientific Research (NWO) and partly funded by the Ministry of Economic Affairs (project number 12405).

References

- [1] J. Camacho, Montserrat Parrilla and Carlos Fritsch. "Phase coherence imaging.", IEEE transactions on ultrasonics, ferroelectrics, and frequency control, 56.5 (2009): 958-974.
- [2] J. F. Synnevåg, , Andreas Austeng and Sverre Holm. "Adaptive beamforming applied to medical ultrasound imaging.", IEEE Transactions on Ultrasonics, Ferroelectrics, and Frequency Control, 54.8 (2007): 1606-1613.
- [3] M. Karaman and M. O'Donnell, Synthetic aperture imaging for small scale systems. IEEE Transactions on Ultrasonics, Ferroelectrics and Frequency Control, 1995. 42: p. 429-442.
- [4] R.Y. Chiao, L.J. Thomas and S.D. Silverstein, Sparse array imaging with spatially-encoded transmits. IEEE Ultrasonics Symposium Proceedings 1997. vol.2. p.1679 – 1682.
- [5] C. H. Frazier and W.D. O'Brien, Synthetic aperture techniques with a virtual source element. IEEE Transactions on Ultrasonics, Ferroelectrics, and Frequency Control, 1998. 45: p. 196-207.
- [6] S. I. Nikolov and J. A. Jensen. "3D synthetic aperture imaging using a virtual source element in the elevation plane." IEEE Ultrasonics Symposium, 2000. Vol. 2. p.1743 – 1747.
- [7] S. I. Nikolov, and J. A. Jensen. "Virtual ultrasound sources in high-resolution ultrasound imaging." Proc. SPIE 4687, Medical Imaging 2002: Ultrasonic Imaging and Signal Processing, 395 (April 12, 2002); doi:10.1117/12.462178.
- [8] M. H. Bae and M.K. Jeong, A study of synthetic-aperture imaging with virtual source elements in B-mode ultrasound imaging systems. IEEE Transactions on Ultrasonics, Ferroelectrics, and Frequency Control, 2000. 47: p. 1510-1519.
- [9] J. Kortbek, J. A. Jensen, and K.L. Gammelmark, Sequential beamforming for synthetic aperture imaging. Ultrasonics, 2013. 53: p. 1-16.
- [10] J. A. Jensen, Field: A Program for Simulating Ultrasound Systems. Medical & Biological Engineering & Computing, 1996. 34: p. 351-353.

Chapter 3

Dual stage beamforming in absence of front-end receive focusing

D. Bera, J.G. Bosch, M.D. Verweij, N. de Jong, and H.J. Vos, "Dual stage beamforming in the absence of front-end receive focusing," Phys. Med. Biol., vol. 62, no. 16, pp. 6631–6648, 2017.

Chapter 3

Ultrasound front-end receive designs for miniature, wireless, and/or matrix transducers might be simplified considerably by direct element summation in receive. In this paper we develop a dual-stage beamforming technique which is able to produce a high quality image from scanlines that are produced with focused transmit, and simple summation in receive (no delays). We call this Non-Delayed Sequential Beamforming (NDSB). In the first stage, low-resolution RF scanlines are formed by simple summation of element signals from a running sub-aperture. In the second stage, delay-and-sum beamforming is performed in which the delays are calculated considering the transmit focal points as virtual sources emitting spherical waves, and the sub-apertures as large unfocused receive elements. The NDSB method is validated with simulations in Field II. For experimental validation, RF channel data were acquired with a commercial research scanner using a 5 MHz linear array, and were subsequently processed offline. For NDSB, good average lateral resolution (0.99 mm) and low grating lobe levels (<-40 dB) were achieved by choosing the transmit $F_{\#}$ as 0.75 and the transmit focus at 15 mm. NDSB was compared with conventional dynamic receive focusing (DRF) and Synthetic Aperture Sequential Beamforming (SASB) with their own respective optimal settings. The full width at half maximum (FWHM) of the NDSB point spread function was on average 20% smaller than that of DRF except for the depths <30 mm and 10% larger than SASB considering all the depths. NDSB showed only a minor degradation in contrast-to-noise ratio and contrast ratio compared to DRF and SASB when measured on an anechoic cyst embedded in a tissue mimicking phantom. In conclusion, using simple receive electronics front-end, NDSB can attain an image quality better than DRF and slightly inferior to SASB.

3.1. Introduction

3.1.1. Background

In conventional ultrasound imaging systems, typically all transducer elements are individually wired out to the ultrasound system front-end, which performs transmit focusing, receive signal amplification, and delay-and-sum (DAS) beamforming with dynamic receive focusing (DRF). The DRF ensures an optimal receive focusing over the entire image depth, but needs pre-set time delay profiles for each reconstructed pixel in the image. Further image optimization needs either static or dynamic receive apodization. Obviously, the complexity of the DRF receive beamformer in the front-end scales roughly linearly with the number of elements. In miniaturized, handheld and/or wearable (wireless) 2D imaging systems, it is desirable to shift part of the front-end processing to the transducer, to reduce the data rate or the number of channels to connect the transducer to a main frame. This also is a necessity for 3D/4D (matrix) transducers, where the number of elements is too large to wire out individually to the ultrasound system. In addition, miniaturized, handheld and/or wearable systems need a minimized front-end size and power consumption, to allow integration into the probe. Both power consumption and physical size will be reduced if the front-end processing consists only of a simple operation such as per-element switching, in contrary to the more complex operations of per-element amplification, temporary signal storage, and/or signal delay.

To demonstrate the relative simplicity of a front-end consisting of mainly switches, we show a possible architecture in Fig. 1. Each transducer element is connected to a tri-state pulser for transmission and a switch (Rx_select) for receive. A logic control unit can fully control each element via two signals. During transmit (when TxEN is set to high), the tri-state pulsers are enabled and transmit focusing is achieved by selecting a group of elements (sub-aperture) and activating each element's pulser at the desired time. During receive, TxEN is set to low and all pulsers are in high impedance state. Each element's Rx_select switch is used to select/deselect the element during reception. This allows controlling the receive sub-aperture size, albeit without any delays within the sub-aperture. RF signals received by the sub-aperture are sent through a single receive path (containing one low-noise amplifier (LNA) and one voltage-controlled gain amplifier (VGA) to implement time-gain compensation) to the ultrasound system at relatively low data rate. By generating sliding sub-aperture windows, this architecture effectively generates a line scan with fixed transmit focusing and no receive focusing, and a single-channel RF output. Provided that a second-stage beamformer can be defined that generates acceptable image quality from the first-stage line scanning, this very simple front-end circuit architecture will be very suitable for the implementation of portable/wireless imaging devices. In this paper we describe details of the dual-stage beamforming for this simplified architecture.

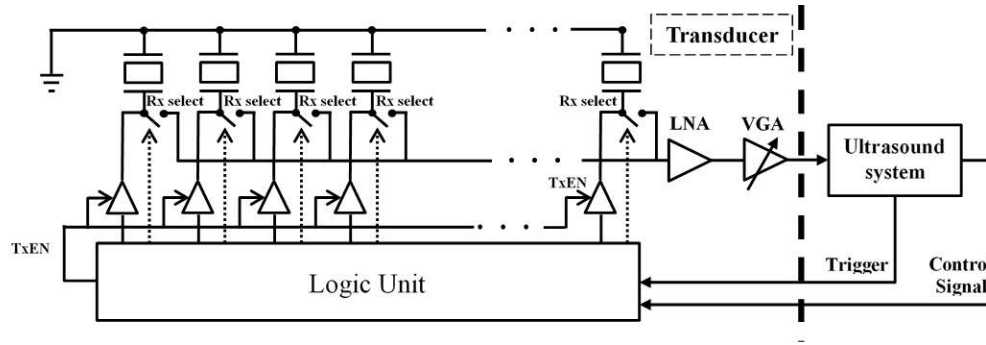


Figure 1: Example of simplified front-end architecture with no delays in receive

3.1.2. Synthetic aperture focusing techniques

The proposed architecture has the obvious limitation that no focusing is possible during receive. Without further processing, this would result in poor image quality. Fortunately, synthetic aperture focusing technique (SAFT) can combine multiple transmit/receive events to synthesize the pixel values in an image. The aim of SAFT is to synthetically focus both the transmit and the receive fields throughout the entire image, as opposed to dynamic receive focusing, in which only the receive field is focused throughout the entire image. Examples of SAFT are found in [1]–[4] where a single element in the transducer aperture transmits a spherical wave that illuminates the full image region. For each transmission, the backscattered echoes are received by the full aperture or a sub-aperture, and the RF channel data are stored to build a low resolution image (LRI) using DAS with DRF. The LRIs from subsequent transmit events are coherently summed to form a high resolution image (HRI). The HRI produced using SAFT has a better lateral resolution than the image using DRF, albeit at lower signal-to-noise ratio because of the use of a single element in transmission, and dramatically increased system complexity because of all-channel simultaneous data capture, transfer, storage, and processing [3], [4]. Several variations of SAFT have further been described [5]–[7] to either improve frame rate and penetration depth, or reduce front-end complexity. A hardware implementation of real-time imaging utilizing single-element transmission SAFT with an array of transducer elements and a multiplexer was described in [5]. In [3] it was proposed to use the same element as both transmitter and receiver, i.e., by using mechanical scanning of a single element across the recording line. The single-element transmit/receive approach is widely used in Non-Destructive Testing (NDT) and radar, but when applied to a single element in an ultrasound array, it may suffer from limited penetration depth, due to the low energy emission. In the handheld ultrasound system using a multi-element transmit and receive aperture for SAFT explored in [1], front-end complexity was an issue. Yet another form of SAFT uses coherent plane wave imaging [8], [9], which potentially produces high signal-to-noise ratio and high frame rate, at the cost of front-end complexity. A sparse SAFT

using fewer transmit pulses was proposed in [6] for real-time 3D imaging with a mechanically scanned linear phased array. However, because of the transmission by a single element at a time, the signal-to-noise ratio is relatively low. Therefore, implementation of such techniques is highly challenging and costly. Overall, none of the aforementioned cases can simultaneously improve penetration depth, front-end complexity and data transfer rate.

3.1.3. Dual-stage beamforming approaches

A way to accommodate the conflicting requirements of front-end simplicity and image quality can be found in so-called dual-stage beamforming approaches, where a simple pre-beamforming is applied in the probe to reduce the number of channels or the data transfer rate, and the final beamforming is performed in the main system. One of these approaches is based on synthetic aperture imaging: Synthetic Aperture Sequential Beamforming (SASB) [10], [11]. SASB considers the transmit focal points as virtual sources in a synthesized aperture. The idea of utilizing the transmit focal point as a virtual source was introduced in [12]. Further studies found that a near depth-independent lateral resolution can be achieved by using a synthesized receive aperture of virtual receivers coinciding with the transmit focal points [13]–[16]. In the first stage of SASB, RF line data are produced by a focused transmission, and single-focus beamforming in receive. The beamformed line data are transferred to the mainframe and stored, yielding a low resolution image. The second stage combines information from multiple RF lines from the first stage and produces the final high resolution image, considering the transmit/receive focal points as virtual source/receivers in the delay calculations. This method differs from prior art on SAFT, as SASB works on beamformed RF data and achieves deeper penetration depth than single-element transmissions, with very similar resolution as SAFT. SASB has already been implemented in hand-held devices for 2D ultrasound imaging with fixed focus beamforming capabilities integrated in the transducer handle [17]. Beamforming with a fixed (non-dynamic) delay pattern simplifies the delay control circuitry compared to SAFT or DRF, and hence reduces the complexity of front-end electronics, but would still not be suitable for the proposed simple front-end architecture above because even the realization of full-aperture fixed time delays requires circuits that are too complex for miniature and/or matrix transducers.

3.1.4. Content outline

In this paper we propose Non-Delayed Sequential Beamforming (NDSB), which is an adapted implementation of SASB, now suited for the described architecture. Similar to SASB, this method employs two stage beamforming and a main-frame memory for storage of intermediately summed RF lines. The appropriate delays in the second stage are calculated by considering the transmit focus as a virtual source, and each receive sub-aperture as one large unfocused element. The primary objective of NDSB is to achieve a similar image quality as conventional DRF, despite NDSB's simpler front-end. Hence, in this paper, we compare the performance in terms of resolution, contrast, and grating lobes of NDSB against DRF and

Chapter 3

SASB.

Section 3.2 presents a detailed description of the NDSB method. Section 3.3 describes the setup of numerical simulations, and experimental validation with an ultrasound research scanner. Section 3.4 presents the performance results. The paper ends with a discussion and conclusion.

3.2. Theory

The NDSB technique is a two-stage procedure. The low resolution RF scan lines of the first stage are used as an input to the second stage to generate the final high resolution image. This second stage can be implemented in programmable hardware or software in the back end of the system. The key point of the NDSB algorithm is finding the appropriate delays that are needed to coherently sum the contribution from scatterers as present in the subsequent RF scan lines. This section therefore first describes the time-of-flight (TOF) of scattered ultrasound pulses within the NDSB framework, and second describes the coherent DAS in the second stage to reconstruct the final high resolution image.

Figure 2 describes the wave propagation path used to compute the TOF for the i^{th} scanline and for two example scatterers positioned at \mathbf{s}_1 and \mathbf{s}_2 . The TOF consists of three components. The first component is the time it takes for the transmitted wave to travel the distance z_v from the center of the transmit aperture to the virtual source \mathbf{v}_i . The second component is the time for the transmit wave to reach a scatterer (e.g. positioned at \mathbf{s}_1) from the virtual source. The third component is the time it takes for the backscattered signal to travel the distance (z_{s_1}) from this scatterer position (\mathbf{s}_1) to the closest element of the receive aperture. This is consistent with the assumption of a forward looking receive sub-aperture, effectively created by having no delays in receive.

Mathematically, the TOF τ for the i^{th} scanline for any scatterer position \mathbf{s} is calculated by

$$\tau(\mathbf{s}, i) = \frac{1}{c} \cdot (z_v \pm |\mathbf{s} - \mathbf{v}_i| + z_s) \quad (1)$$

and

$$|\mathbf{s} - \mathbf{v}_i| = \sqrt{[(x_s - x_{v_i})^2 + (z_s - z_v)^2]} \quad (2)$$

where c is the speed of sound, $\mathbf{v}_i = (x_{v_i}, z_v)$ is the virtual source position and $\mathbf{s} = (x_s, z_s)$ is the scatterer position. The \pm sign in (1) depends on the position of \mathbf{s} . If \mathbf{s} is situated below the virtual source then the delay is added with respect to the virtual source position, otherwise it is subtracted. The TOFs computed for the i^{th} scanline and for the scatterers at \mathbf{s}_1 and \mathbf{s}_2 , determine the positions of the RF samples \mathbf{s}'_1 and \mathbf{s}'_2 , containing the projections of these scatterers. Due to the transmit focus in NDSB, individual RF samples in the first stage signals contain information from a set of spatial positions. This is exemplified in Fig. 2, where the RF samples

Dual stage beamforming in absence of front-end receive focusing

at s'_1 and s'_2 on the i^{th} LRI line will contain the information from all the scatterers located on the two red arcs.

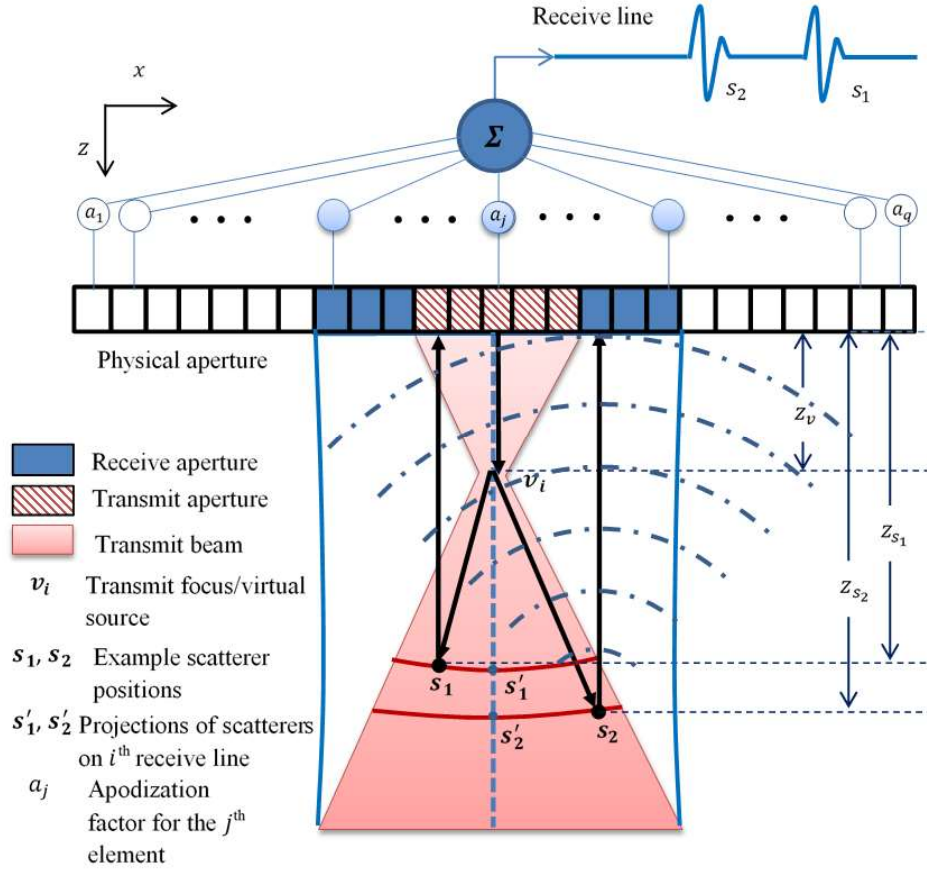


Figure 2: the transmit/receive geometry and wave propagation paths for two scatterers during the first stage beamforming in NDSB

Whereas Fig. 2 shows the TOF of the pulse scattered from the scatterers at s_1 and s_2 producing the RF samples on the i^{th} LRI line, Fig. 3 explains how the information in the LRIs is recombined to produce the final image at every image point p , which is the actual second stage beamforming step. In Fig. 3, the RF samples at positions indicated by the blue and black dots on different LRI lines (l_m to l_n including l_i) contain the projections of a scatterer located close to the image point p . Therefore, to reconstruct the image point p (black dot in Fig. 3) during the second stage imaging, the RF samples from the set of LRI lines (the blue dots in Fig. 3) are summed to produce the final value.

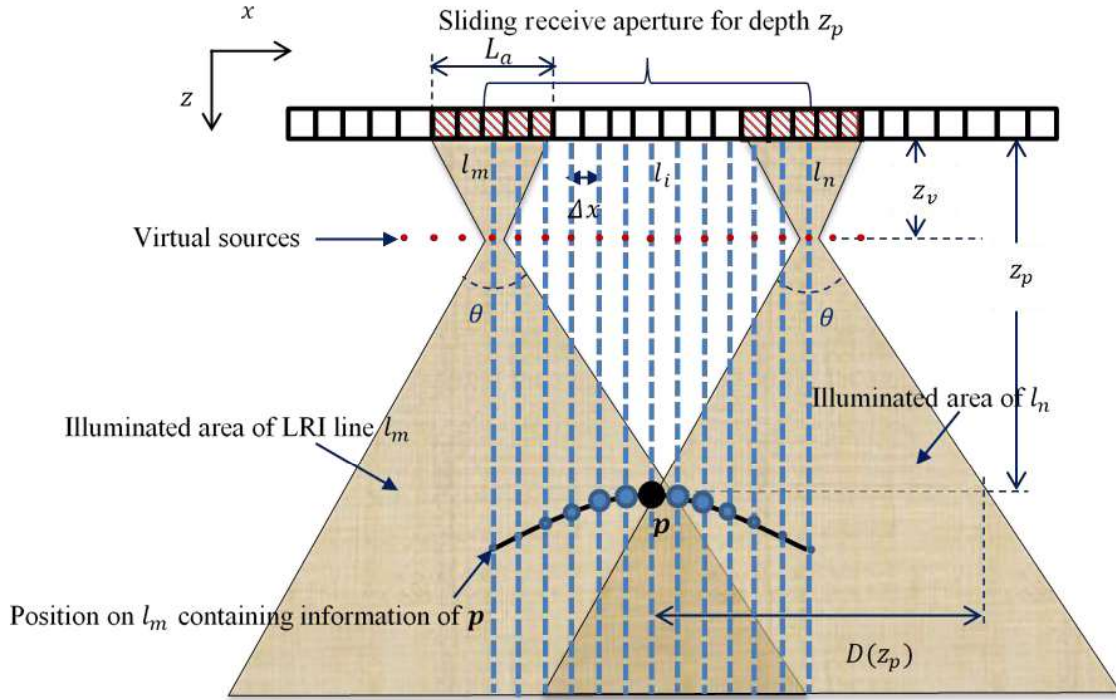


Figure 3: The geometry underlying the second stage beamforming. An image point \mathbf{p} (black dot) is reconstructed using the RF values from low resolution lines located on the solid black hyperbola, calculated by Eqs. (1) and (2).

The RF samples in the second stage processing are weighted before summing. Thus, a point in the high resolution image HRI at $\mathbf{p} = (x_p, z_p)$ is computed according to

$$HRI(\mathbf{p}) = \sum_{k=-N(z_p)/2}^{N(z_p)/2} W(k, z_p) \cdot l_{(i+k)}(\tau(\mathbf{p}, i+k)) \quad (3)$$

where l_i is the time trace of the closest LRI line to \mathbf{p} , which corresponds to the i^{th} transmit beam. The function W corresponds to a depth dependent apodization function controlling the weighting. Here, W is chosen as a Hanning window centered at $k = 0$. The domain of W is limited by $N(z_p)$ (in Fig. 3, $N(z_p) = n - m + 1$). The term $N(z_p)$ represents the range of LRI lines that contribute to the second stage imaging at a depth z_p . For the image point \mathbf{p} , $N(z_p)$ can be computed from the geometry shown in Fig. 3 as

$$N(z_p) = \frac{D(z_p)}{\Delta x} = \frac{2 \cdot (|z_p - z_v|) \tan(\theta/2)}{\Delta x} \quad (4)$$

where $D(z_p)$ denotes the lateral width of the transmit beam at depth z_p , Δx is the distance

between two consecutive low resolution lines, and θ the opening angle of the beam. Therefore, $D(z_p)$ depends on the transmit opening angle θ and the depth of virtual source z_v . The opening angle of the transmit beam is related to the physical width of the sub-aperture L_a and the depth of virtual source z_v by

$$\theta = 2 \cdot \arctan\left(\frac{L_a}{2z_v}\right) \quad (5).$$

Now the ratio of z_v and L_a is expressed as $F_{\#}$ and given by

$$F_{\#} = \frac{z_v}{L_a} \quad (6).$$

From Eqs. (5) and (6), we can see that θ is inversely related to $F_{\#}$ in transmit: decreasing the $F_{\#}$ increases the opening angle and hence the image area covered by the transmit wave. This in turn increases the number of LRI lines that are used in the second stage beamforming, which is expected to improve the lateral resolution in the reconstructed image. Therefore, depth of virtual source z_v and size of the sub-aperture L_a are two critical parameters in NDSB. Because only two of the three quantities L_a , z_v and $F_{\#}$ are independent, in the following we choose to investigate the influence of z_v and $F_{\#}$ on the image quality.

3.3. Simulations and Measurements

The NDSB technique was examined using simulations and verified by offline processing of channel data acquired with a commercial programmable ultrasound system. The resolution of this technique was tested on a number of point targets with a range of $F_{\#}$ values and virtual source depths. Secondly, an anechoic cyst was used for evaluating image contrast. Lateral resolution, contrast-to-noise ratio (CNR) and contrast ratio (CR) were compared to those of conventional B-mode imaging (i.e. using fixed transmit focus and DRF), and of SASB. The simulation was performed with a model of a 5 MHz linear array transducer with properties similar to the commercial L14-5 transducer [18] that was used in the measurements.

3.3.1. Simulation setup

We have investigated NDSB using simulations in Field II [19] with the transducer parameters and imaging parameters as shown in Table 1. For all the methods DRF, SASB and NDSB the receive sub-aperture size was kept constant over time (non-dynamic). An element count of 64 in the sub-apertures corresponds to the number of receive channels in the SonixTouch internal ultrasound engine.

The transducer excitation was a 2 cycle, 5 MHz sinusoid tone burst. Next to that, the impulse response of the transducer was simulated with a 2 cycle sinusoid. Thus, the actual simulated round-trip signal is characterized by a 40% fractional -6 dB bandwidth. The lateral point spread function was determined by six point scatterers placed along the central line of the image at

Chapter 3

depths ranging from 10 mm to 60 mm with 10 mm distance. The image contrast was evaluated by imaging an anechoic cyst surrounded by randomly placed scatterers (mimicking a homogeneous tissue with 0.5 dB/MHz/cm attenuation and 1540 m/s ultrasound velocity). The diameter of the cyst was 4.5 mm and it was placed at a depth of 45 mm.

Table 1: Default imaging parameters for the simulations

Parameters		Value
Sampling frequency in simulation		100 MHz
Centre frequency		5 MHz
Wavelength (λ)		308 μm
Pitch		308 μm (λ)
Number of elements in the probe		128
Excitation pulse		2 cycle sinusoid
Baffle condition		Rigid
First stage	Transmit focus (\mathbf{z}_v)	1, 5, 10, 15 and 20 mm
	Transmit sub-aperture elements (max)	64
	Receive sub-aperture elements	64
	Transmit $F_{\#}$	0.5, 0.75, 1.0 and 2.0
	Tx/Rx Apodization	Hanning
	Number of image lines	128
	Distance between lines (Δx)	308 μm (λ)
Second stage	Apodization	Hanning
	Number of image lines	128
	Distance between lines (Δx)	308 μm (λ)

3.3.2. Measurement setup

For data acquisition, a commercial programmable ultrasound system SonixTouch (BK Ultrasound, Richmond BC, Canada) with linear array transducer L14-5 [18] (pitch: 300 μm and frequency range: 5-14 MHz) was used. The SonixTouch has no option for transmit apodization. A SonixDAQ (BK Ultrasound) captured raw RF channel data with a fixed gain at 40 MHz sampling rate, and saved the data for offline processing. Before image reconstruction the channel data was filtered with a band pass filter with -6 dB cut-off frequencies 2.5 MHz and 7.5 MHz. Envelope detection and logarithmic compression were performed to generate the final images for all the methods after the final stage of beamforming. A commercial tissue phantom (multi-purpose multi-tissue ultrasound phantom 040-GSE, CIRS, Virginia, USA) [20] with 0.5 dB/MHz/cm attenuation and containing wire targets and anechoic cysts, was used as imaging object.

3.4. Results

3.4.1. Simulation results

3.4.1.1. Appropriate imaging parameters for NDSB

To start the simulation series, we first used a transmit $F_{\#}$ of 2.0 and virtual source at 20 mm to produce an image of scatterers with the NDSB technique. These settings are copied from the SASB technique according to [10] and would yield, for SASB, an optimal resolution throughout depth, without grating lobes, given a λ scan line spacing. Fig. 4 shows the results for this choice of parameters, at a dynamic range of 40 dB. Qualitatively, similar to SASB, the PSFs for NDSB appear relatively constant over depth, and no grating lobes are visible. However, because of absence of receive focusing, the resolution may be sub-optimal. In

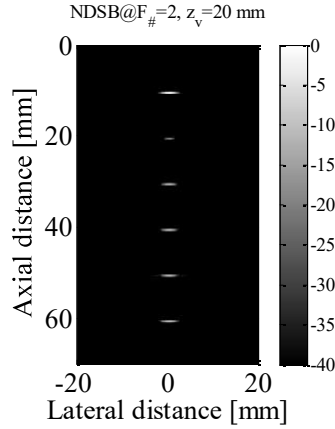


Figure 4: Image after second stage beamforming using NDSB, with sub-optimal settings of a transmit $F_{\#} = 2.0$ and a virtual source at $z_v = 20$ mm.

general, a higher resolution should be obtained if, for fixed z_v , we would increase $F_{\#}$ up to the point where L_a becomes so small that grating lobes occur. This, therefore, is the approach for changing the imaging parameters in the sections below.

To find better imaging settings, various simulations were performed with the NDSB method to optimize the lateral resolution (as defined by the -6dB and -20 dB width of the main lobe in the point spread function) while keeping the grating lobes < -40 dB. We performed simulations with wider transmit opening angles (transmit $F_{\#}=1.0, 0.75$ and 0.5) for different virtual source depths (1, 5, 10, 15 and 20 mm) and studied the effect on lateral resolution at different imaging depths. Settings that would exceed 64 active elements were discarded, which happened for low $F_{\#}$ and large focal depth. Lateral resolutions for all simulated images were determined at different depths from the response of the point scatterers at the central image line. A point spread function (PSF) with broader main lobe or higher side lobes translates to poorer lateral resolution. The lobe width is computed at -6 dB, i.e. the full width at half maximum (FWHM), and at -20 dB. The dynamic range for the displayed images was chosen to be 40 dB, as a grating lobe level of 30 to 40 dB below the main lobe level is considered acceptable in practice [21].

Chapter 3

Therefore, in the following images, any grating lobes below -40 dB are not visible.

Fig. 5 shows the quantified lateral resolution at -6 dB for the NDSB images with $F_{\#} = 1.0, 0.75$ and 0.5 and a range of virtual source depths. From Fig. 5 it is concluded that for a fixed $F_{\#}$, the lateral resolution improves as the depth of virtual source is increased. For a fixed $F_{\#}$, increasing the depth of the virtual source also increases the sub-aperture size. Therefore, the best resolution is produced by the max sub-aperture size (64 elements). From these three sub-figures three best settings ($F_{\#} = 1.0$ with $z_v = 20$ mm, $F_{\#} = 0.75$ with $z_v = 15$ mm and $F_{\#} = 0.5$ with $z_v = 10$ mm) were chosen for the final comparison.

The quantified resolution of the images with the three best settings mentioned above is shown in Fig. 6. Fig. 6 shows that $F_{\#} = 1.0$ and virtual source at 20 mm produces slightly better lateral resolution at larger depth (>40 mm), whereas $F_{\#} = 0.5$ and virtual source at 10 mm produces better lateral resolution at shallower depth (<40 mm). An $F_{\#} = 0.75$ and virtual source at 15 mm yields a good overall performance for NDSB considering the lateral resolution at all depths, and was chosen as the best settings for NDSB in the remainder of the analysis.

3.4.1.2. Quantitative comparison of lateral resolution of NDSB with DRF and SASB

We compared the overall achievable best image quality of NDSB with that of conventional DRF and SASB. Each method has its specific focusing characteristics and will require quite different settings of $F_{\#}$ and depth of transmit focus for achieving a good image quality (in terms of lateral resolution and grating lobe level). Therefore, for a realistic comparison, the image obtained using SASB was generated with the best known configuration (virtual source depth of 20 mm and $F_{\#} = 2.0$) as stated in [10]. DRF was simulated with $F_{\#} = 2.0$ and the transmit focus was kept at 30 mm (the average image depth).

For completeness, we also compared the methods for identical settings and report the results in Appendix A. This confirms that it is more useful to present comparisons of each method with their own respective best settings.

Fig. 7 shows the images with DRF, SASB and NDSB. The quantified lateral resolution for these images is shown in Fig. 8. For depths >30 mm, the FWHM (-6 dB) of the PSFs for NDSB is on average 20% smaller than for DRF, but 40% larger than for SASB. NDSB is limited by its receive aperture for those depths. However, until 30 mm depth, the FWHM of PSFs for NDSB is on average 20% smaller than that of SASB, which can be explained by the higher transmit $F_{\#}$ applied in SASB leading to a worse resolution. The FWHM of PSFs for NDSB is on average 10% broader than SASB considering all depths. Similar trends are visible in the resolution at -20 dB level.

Dual stage beamforming in absence of front-end receive focusing

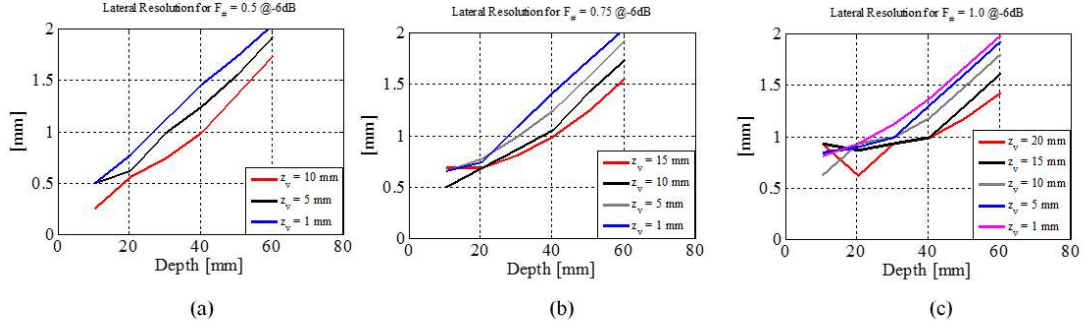


Figure 5: Lateral resolution at -6 dB as a function of depth for NDSB images with (a) $F_{\#} = 0.5$, (b) $F_{\#} = 0.75$ and (c) $F_{\#} = 1.0$ for different virtual source depths z_v .

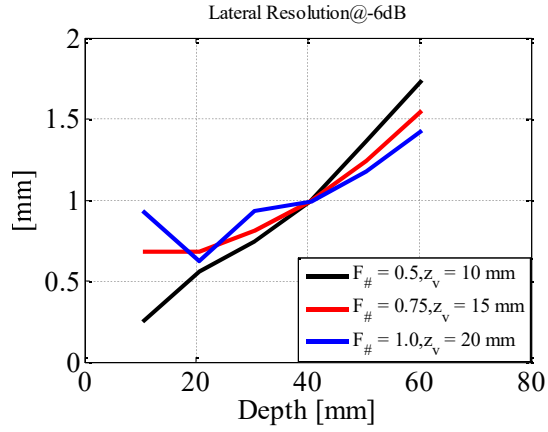


Figure 6: Lateral resolution at -6 dB as a function of depth for NDSB images with the best settings from Fig. 5.

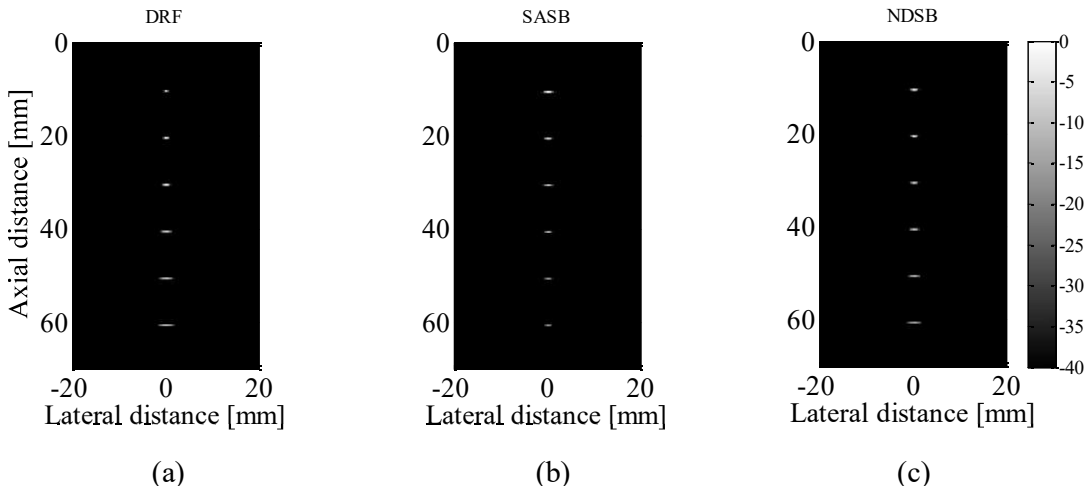


Figure 7: Images using (a) DRF ($F_{\#} = 2.0, z_v = 30$ mm), (b) SASB ($F_{\#} = 2.0, z_v = 20$ mm) and (c) NDSB ($F_{\#} = 0.75, z_v = 15$ mm)

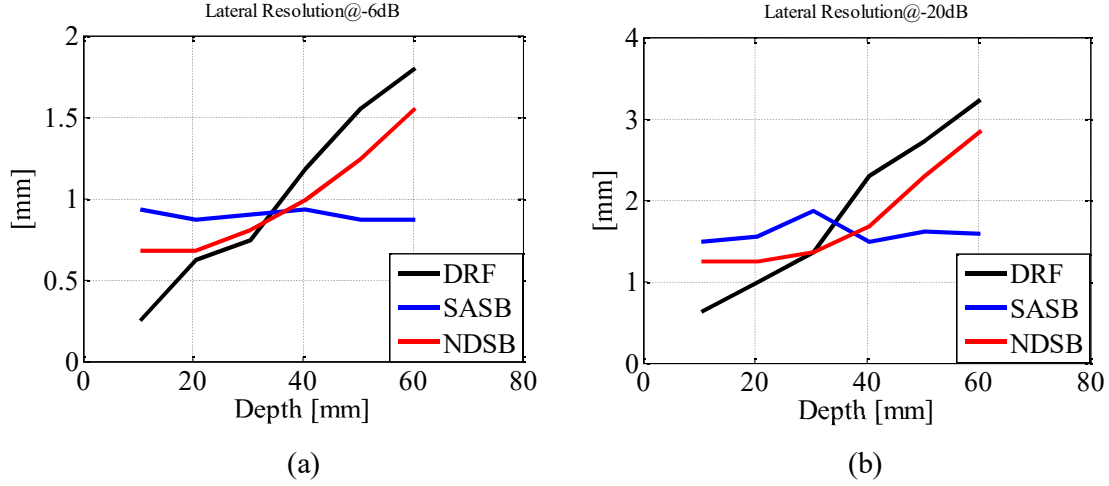


Figure 8: Lateral resolution (a) at -6 dB and (b) at -20 dB as function of depth of the DRF, SASB and NDSB images of Fig. 7.

3.4.1.3. Comparison of contrast of NDSB with DRF and SASB

The performance of NDSB on the cysts is estimated using the CNR and CR as defined in [22], which are given by

$$CNR = \frac{\mu_s - \mu_c}{\sqrt{(\sigma_s^2 + \sigma_c^2)/2}} \quad (6)$$

$$CR = \frac{\mu_s - \mu_c}{(\mu_s + \mu_c)/2} \quad (7)$$

where μ_s and μ_c are the mean amplitudes of a speckle region and a cyst region, respectively, and σ_s^2 and σ_c^2 represent the variances of the speckle and cyst region. Both CNR and CR are calculated using 1.5 mm x 1.5 mm square regions on the envelope of the RF data before log-compression. The cyst region is selected at the center of the cyst. The speckle region is selected at the same depth, 7 mm to the right. Fig. 9 shows the images of the simulated cyst using DRF, SASB and NDSB using the same imaging parameters as used for the simulations of Fig. 7. The CNR values calculated from these images were 2.7, 2.6 and 2.4, respectively. The CR values for these images were 1.9, 1.9 and 1.8, respectively (where 2 is the asymptotic limit of zero signal level in the cyst). These CNR and CR values indicate that NDSB performs only slightly inferior to DRF and SASB in these simulations.

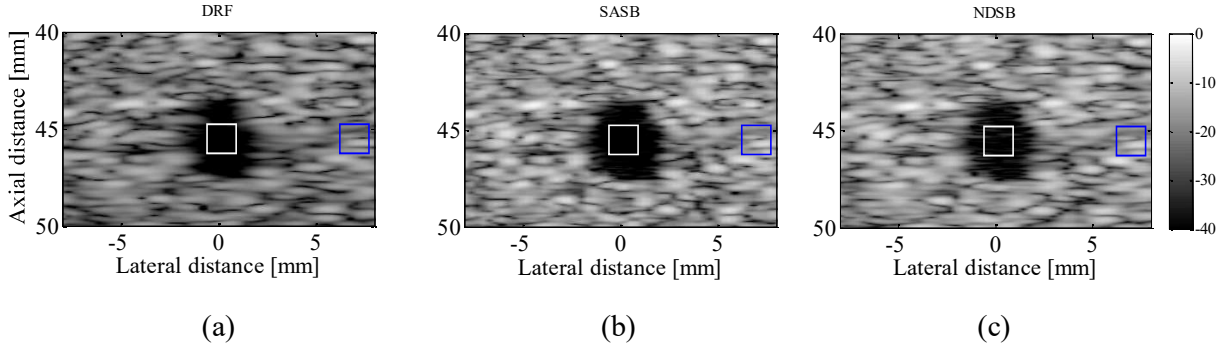


Figure 9: Simulated images of an anechoic cyst using (a) DRF, (b) SASB and (c) NDSB. The same settings have been used as for Fig. 7.

3.4.1.4. Measurement Results

A. Performance on lateral resolution

Fig. 10 shows the images of the tissue mimicking phantom using the first stage and the second stage beamforming of both SASB and NDSB, and using DRF, on the experimentally acquired data. Fig. 11 quantifies the -6 dB PSF width derived from the DRF image and the second stage images of SASB and NDSB. We kept the same settings of the imaging parameters (transmit $F_{\#}$ and transmit focus/virtual source depth z_v) for the three methods as we have used in simulations. As expected, the PSFs in the LRI produced by NDSB (in Fig. 10 (b)) is wider and flatter than the PSFs in the LRI produced by SASB (in Fig. 10 (a)). The lateral resolution is better in the HRI-NDSB (Fig. 10(c)) than in the DRF image (Fig. 10(a)) except for the depths nearby the transducer. From the quantified lateral resolution at -6 dB in Fig. 10 it can be observed that the NDSB method consistently outperforms DRF in terms of lateral resolution at depths ≥ 20 mm. For depths ≥ 30 mm the lateral resolution of HRI-SASB (Fig. 10(b)) is better than for HRI-NDSB. Both for NDSB and SASB one can see degradation in lateral resolution near the lateral edges of the images. Fig. 11 shows similar values for lateral resolution at -6 dB as those shown in Fig. 8(a) for simulated data, confirming the good correspondence of measurements and simulations.

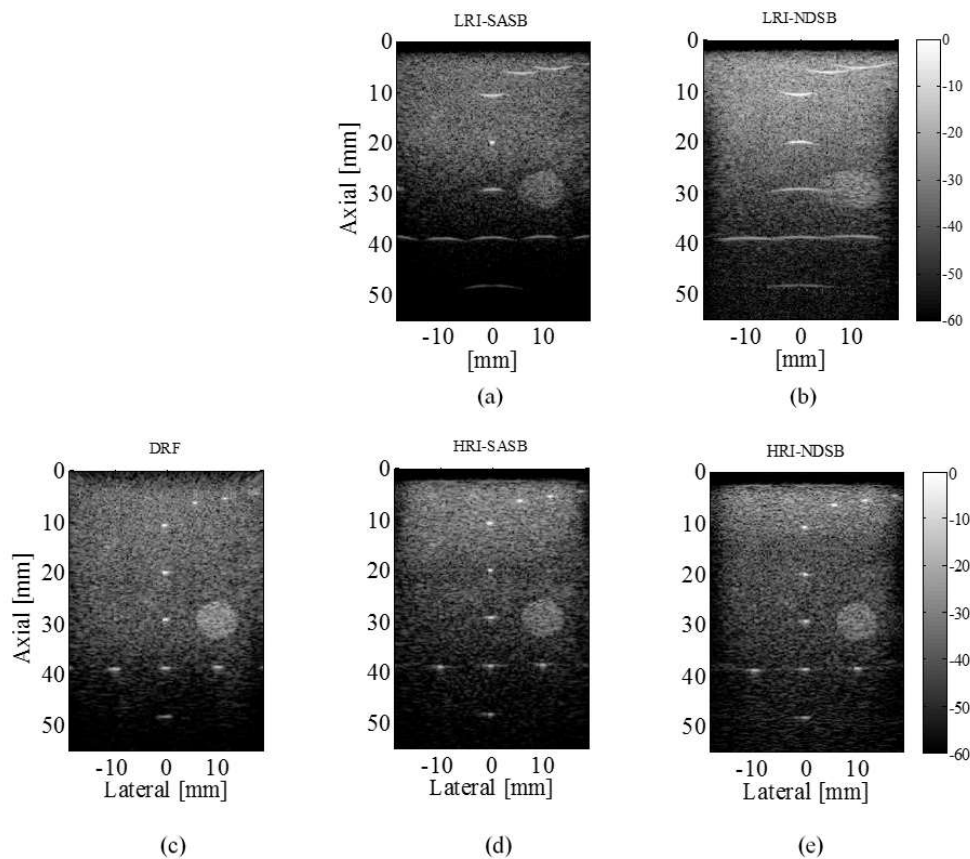


Figure 10: Images from measurement data: (a) LRI using SASB, (b) LRI using NDSB, (c) DRF, (d) HRI using SASB and (e) HRI using NDSB

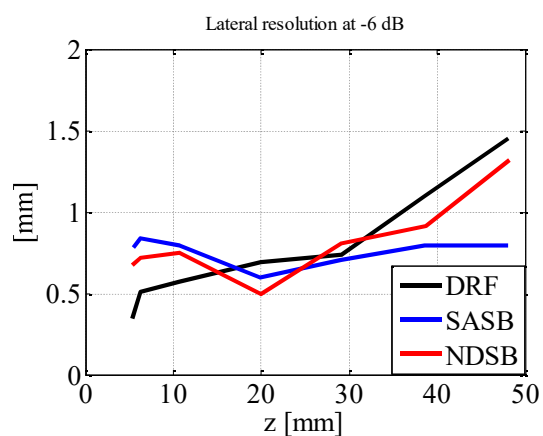


Figure 11: Lateral resolution at -6 dB as a function of depth for the images using DRF, SASB and NDSB of Fig. 10

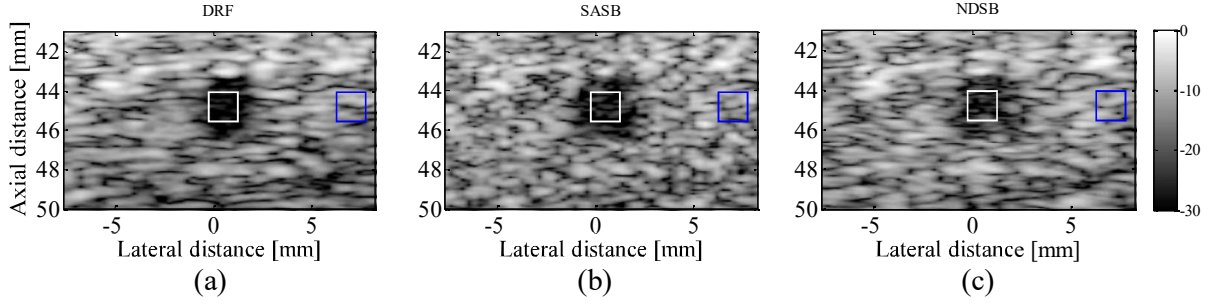


Figure 12: Images of anechoic cyst of the CIRS tissue mimicking phantom using (a) DRF, (b) SASB and (c) NDSB

B. Performance on cyst image

Fig. 12 shows the cyst images using DRF, SASB and NDSB. Images were cropped to highlight the cyst region. The cysts are well recognizable for all the images. To compare the performance of NDSB with other methods we computed CNR and CR as defined in Eq. (6) and (7) for these images using 1.5 mm x 1.5 mm square windows. The CNR for DRF, SASB and NDSB were 2.5, 2.4 and 2.3, respectively. The CR values for these images were 1.5, 1.3 and 1.2, respectively. Given these CNR and CR values we can conclude that NDSB performs only slightly inferior to DRF and SASB.

3.5. Discussion

3.5.1. General findings

The motivation for NDSB is to make the advantages of techniques like SAFT and SASB available for an ultrasound system with highly reduced complexity and limited capabilities for computation, storage and data transfer in the front-end electronics. The objective is to achieve similar lateral resolution to conventional DRF with a simple receive front-end which only sums the non-delayed RF signals received by some or all elements. No beamforming strategy was available to produce a high-quality image using the data produced by such a simple receive front-end. Both in simulation and measurement, the results show that NDSB can yield images with even better lateral resolution at larger depths compared to DRF.

The overall image quality (in terms of lateral resolution and grating lobe level) for NDSB is determined by the transmit $F_{\#}$, the virtual source depth, the line pitch (inverse of line density) and receive sub-aperture size in the first stage of beamforming. The NDSB method was assessed using numerical simulations and by offline processing of data acquired with a commercial ultrasound scanner. From [10] we already know that the larger effective opening angle of the beam (by lowering the $F_{\#}$, either by reducing the depth of the virtual source or by increasing the transmit sub-aperture size), leads to an improved lateral resolution in the final image, as it increases the number of LRI lines that are coherently combined in the second stage

Chapter 3

beamforming. Again, as explained in [10] the opening angle (determined by the $F_{\#}$) at the virtual source and the line density together influence the level of the grating lobes. Due to the absence of receive focusing in NDSB, it is intrinsically less sensitive to the grating lobes compared to SASB. Therefore, even with λ line spacing, we can still use larger transmit opening angle for NDSB to improve the lateral resolution without producing significant grating lobe levels. With respect to the receive sub-aperture size, the large transmit opening angle can only be fully used if the transmit field overlaps the receive field. An increase in receive aperture size in the first stage beamforming will lead to a better overlap between transmit and receive field and therefore will improve the lateral resolution. However, a larger receive aperture will also receive more energy from the grating lobes produced during transmit. Therefore, grating lobe energy will increase for a larger receive aperture in NDSB. With the present constraint of the receive sub-aperture size it was observed that $F_{\#} = 0.75$ and virtual source at 15 mm produced a good overall lateral resolution and grating lobe levels < -40 dB, which motivates our choice of settings.

The performance of NDSB is compared to conventional DRF and SASB with their respective best settings as was mentioned in 4.1.2. Simulations show that the FWHM of the PSFs i.e. lateral resolution for NDSB is on average 20% narrower than DRF except at depths close to the transducer. However, the FWHM for NDSB PSFs is slightly broader (10% on average) than SASB. SASB suffers from a relatively poor lateral resolution at lower depth (depth < 30 mm) due to the large $F_{\#}$. To estimate the imaging performance of NDSB, the CNR and CR were computed for a simulated cyst of 4.5 mm diameter at 45 mm depth. Based on the CNR and CR values, we can conclude that NDSB performs only slightly inferior to DRF and SASB.

When applied to the data acquired with the commercial scanner and the tissue phantom with scattering wires and a cyst region, NDSB yielded images which support the results from the simulations. Quantified lateral PSF in measured data was slightly larger than in simulations. That could be due to the fact that for the measured data we used a boxcar window for the transmit apodization instead of a Hanning window, because of system limitations. The differences in CNR and CR values between simulation and measured data could be due to higher noise introduced by the acquisition system of the ultrasound scanner. Apart from using the raw channel data using SonixDAQ, NDSB could also be implemented by utilizing the built-in beamformer (Texo) of the SonixTouch. To produce a LRI, the first stage of NDSB can be performed in Texo by disabling the DRF. The LRI can then be used in the second stage of NDSB to produce the final HRI. Our current implementation using the SonixDAQ, however, allowed a full control of signal processing and thus allowed comparison of different processing techniques (SASB, NDSB and DRF) based on the same original raw dataset.

The proposed simplified front-end architecture can easily be extended for matrix transducers by expanding the transmit/receive aperture in the other dimension, without any significant increase in the hardware complexity. To use such a matrix transducer for 3D/4D imaging,

NDSB can be applied in either row wise or column wise fashion. The absence of delays allows highly desirable savings in the power budget and silicon area which can facilitate realizing more in-transducer building blocks with enriched functionalities (e.g. digitization, channel multiplexing/de-multiplexing, signal compression, etc.) A front-end architecture similar to this was already proposed in a row-column parallel [23] architecture for designing a matrix transducer with a front-end ASIC.

Although for the proposed front-end architecture in Fig. 1 we did not show any block for apodization, we believe that it can be easily implemented with a slight increase in complexity: the switch can be replaced by a simple circuit (basically a field-effect transistor) where the (analog) control signal linearly controls the attenuation of the element signal.

3.5.2. Limitations

There are some limitations that apply to NDSB and to this study. Due to the limited physical aperture of the transducer the performance of NDSB is expected to deteriorate near the lateral edge of the scanning area. This limitation also holds for SASB but due to the lower $F_{\#}$ it is more severe for NDSB. The NDSB method was investigated with static phantom objects so, tissue motion, aberration artifacts etc. were not studied. However, NDSB is not intended to overcome such challenges and will suffer from similar artifacts as SAFT.

We reported the effects of $F_{\#}$ and transmit focal depth on lateral resolution, grating lobes, and contrast for the NDSB technique, since we thought that they are the primary quality measures that really depend on the beamforming algorithm itself. There are other general quality measures that can be provided, of which signal-to-noise ratio (SNR) (and resulting penetration depth) and axial resolution are the most important. With respect to the SNR, the NDSB algorithm combines multiple transmit/receive lines to generate the final HRI. Therefore, an increase in SNR in the final image is expected compared to DRF, but not compared to SASB which similarly combines multiple transmit/receive lines. Moreover, other effects such as the limited number of electronic components in the signal chain and possible apodization may also affect the final SNR. Therefore, the final effect of implementation of the NDSB algorithm on SNR is a subject for further exploration. On the other hand, the axial resolution is mainly determined by the acoustic transducer and pulse characteristics. As expected, we found in initial analysis that the beamforming algorithms did not lead to any difference in axial width of the PSFs, and we therefore left out its analysis in this paper. Moreover, the effect of line density in the first stage beamforming on grating lobe levels for NDSB were not explored in this study, as NDSB has shown to be less sensitive to grating lobes than SASB. In initial simulations, we found that the current choice of λ pitch produced sufficiently low (<40 dB) grating lobes in the second stage beamforming to be a good practical choice. As such, we think that the current choices of settings and quality parameters are the most relevant to demonstrate the capabilities of the NDSB algorithm compared to DRF and SASB. The NDSB is a two-stage beamforming method similar in data processing to SASB. Therefore, it has a similar data transfer rate and

Chapter 3

frame rate as SASB.

3.6. Conclusion

Simulation and measurement results confirm that Non-Delayed Sequential Beamforming (NDSB) can be considered a useful beamforming technique for miniaturized linear/matrix array and/or wireless systems with a large number of elements and/or simple front-end electronics. With the chosen settings, NDSB provides better lateral resolution than conventional dynamic receive focusing (DRF), except nearby the transducer and slightly worse than that of the Synthetic Aperture Sequential Beamforming (SASB) image. The CNR and CR values for NDSB were only slightly inferior to DRF and SASB while imaging an anechoic cyst.

Appendix A.

Comparison of NDSB to SASB for identical parameter settings

In the main text we showed that a transmit $F_{\#} = 0.75$ and focus depth of $z_v = 15$ mm yields a good overall lateral resolution and low grating lobe levels at all depths for the proposed NDSB technique. We compared the lateral resolution of NDSB to that of conventional dynamic receive focusing and to that of earlier proposed SASB as a reference. Yet, in that comparison we used different transmit $F_{\#}$ and focus depth for each method, separately selected for their optimal performance. For completeness and further understanding of the effect of parameter settings on image quality for NDSB versus SASB, this appendix compares the lateral resolution and grating lobe levels when the transmit $F_{\#}$ and focus depth are set equally for the two techniques.

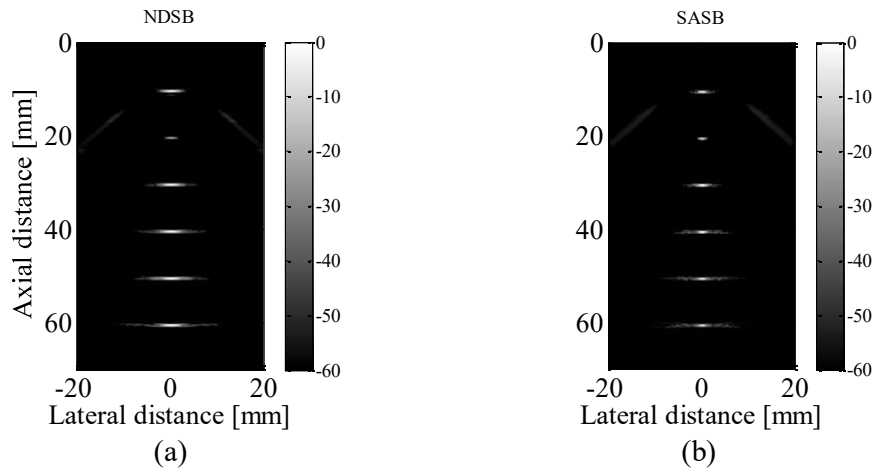


Figure A1: Image after second stage beamforming using (a) NDSB and (b) SASB for transmit $F_{\#} = 2.0$ and a virtual source at 20 mm.

Fig. A1 shows simulated images in which the settings are optimal for SASB, as reported by Kortbek et al. [10], which are $F_{\#} = 2.0$ and virtual source depth at 20 mm. The point scatterers

Dual stage beamforming in absence of front-end receive focusing

are located at depths ranging from 10 mm to 60 mm. From Fig. A1, it can be observed that the lateral resolution of NDSB across all depths is worse than SASB. By quantifying the full width at half maximum (FWHM) across all depths, it can be seen that the main lobe width of NDSB is twice as wide as that of SASB, on average. This is due to the lack of focusing upon receive in NDSB. Grating lobe levels for both the images are lower than -40 dB.

Fig. A2 shows the images formed by NDSB and SASB using the optimal parameter settings for NDSB ($F_{\#} = 0.75$ and virtual source depth at 15 mm). From Fig. A2, it can be observed that the lateral resolution of NDSB is now better than before (Fig. A1(a)). After quantification of FWHM at all depths, it can be observed that the average main lobe width of NDSB (in Fig. A2(a)) is at least 1.5 times smaller than in Fig. A1(a) and comparable to Fig. A1(b). Yet, the average main lobe width of NDSB is now 2.5 times worse than SASB (Fig. A2(b)). On the other hand, the grating lobes in SASB are at a level on the order of -20 dB, which is unacceptably high in medical imaging, unlike NDSB for this settings. This is in line with the observation in [10] that lateral resolution of SASB can be improved by reducing transmit $F_{\#}$ but that it will introduce unacceptably high grating lobes, yielding images with poor CNR and CR values. The lack of receive focusing in NDSB led to limited overlap between the receive fields and the transmission grating lobes, thus lowering the grating lobes for NDSB. From Figs. A1 and A2, it is clear that both NDSB and SASB have their own optimal parameter settings, implying that the best comparison of lateral resolution and grating lobe levels is done when the techniques are implemented with their own respective optimal settings.

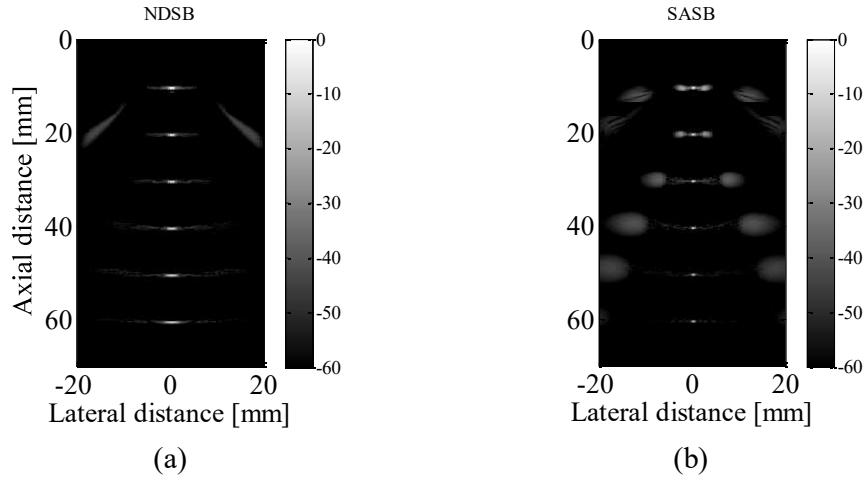


Figure A2: Image after second stage beamforming using (a) NDSB and (b) SASB for transmit $F_{\#} = 0.75$ and a virtual source at 15 mm.

Acknowledgements

We like to acknowledge Ultrasonix/BK Ultrasound for the technical support. This research is supported by the Dutch Technology Foundation STW, which is part of the Netherlands

Chapter 3

Organization for Scientific Research (NWO) and partly funded by the Ministry of Economic Affairs (project number 12405). This work is also part of the research program Heartin4D, which is financed by the Netherlands Organization for Scientific Research (NWO).

References

- [1] M. Karaman and M. O'Donnell, "Synthetic aperture imaging for small scale systems," *IEEE Trans. Ultrason. Ferroelectr. Freq. Control*, vol. 42, no. 3, pp. 429–442, 1995.
- [2] R. Y. Chiao, L. J. Thomas, and S. D. Silverstein, "Sparse array imaging with spatially-encoded transmits," *1997 IEEE Ultrason. Symp. Proceedings. An Int. Symp. (Cat. No.97CH36118)*, vol. 2, 1997.
- [3] J. T. Ylitalo and H. Ermert, "Ultrasound synthetic aperture imaging: monostatic approach," *IEEE Trans. Ultrason. Ferroelectr. Freq. Control*, vol. 41, no. 3, pp. 333–339, 1994.
- [4] M. H. Pedersen, K. L. Gammelmark, and J. A. Jensen, "In-vivo evaluation of convex array synthetic aperture imaging," *Ultrasound Med. Biol.*, vol. 33, no. 1, pp. 37–47, 2007.
- [5] D. K. Peterson and G. S. Kino, "Real-Time Digital Image Reconstruction: A Description of Imaging Hardware and an Analysis of Quantization Errors," *IEEE Trans. Sonics Ultrason.*, vol. 31, no. 4, 1984.
- [6] G. R. Lockwood, J. R. Talman, and S. S. Brunke, "Real-time 3-D ultrasound imaging using sparse synthetic aperture beamforming," *IEEE Trans. Ultrason. Ferroelectr. Freq. Control*, vol. 45, no. 4, pp. 980–988, 1998.
- [7] C. R. Hazard and G. R. Lockwood, "Theoretical assessment of a synthetic aperture beamformer for real-time 3-D imaging," *IEEE Trans. Ultrason. Ferroelectr. Freq. Control*, vol. 46, no. 4, pp. 972–980, 1999.
- [8] G. Montaldo, M. Tanter, J. Bercoff, N. Benech, and M. Fink, "Coherent plane-wave compounding for very high frame rate ultrasonography and transient elastography," *IEEE Trans. Ultrason. Ferroelectr. Freq. Control*, vol. 56, no. 3, pp. 489–506, 2009.
- [9] J. Cheng and J. Y. Lu, "Extended high-frame rate imaging method with limited-diffraction beams," *IEEE Trans. Ultrason. Ferroelectr. Freq. Control*, vol. 53, no. 5, pp. 880–899, 2006.
- [10] J. Kortbek, J. A. Jensen, and K. L. Gammelmark, "Sequential beamforming for synthetic aperture imaging," *Ultrasonics*, vol. 53, no. 1, pp. 1–16, 2013.
- [11] M. M. Mota, P. L. M. J. Van Neer, M. S. Van Der Heiden, and A. W. F. Volker, "Generating a pencil beam from a focused transducer using Stolt migration," *IEEE Int. Ultrason. Symp. IUS*, pp. 982–985, 2013.
- [12] C. Passmann and H. Ermert, "A 100-MHz ultrasound imaging system for dermatologic

- and ophthalmologic diagnostics,” *IEEE Trans. Ultrason. Ferroelectr. Freq. Control*, vol. 43, no. 4, 1996.
- [13] C. H. Frazier and W. D. O’Brien, “Synthetic aperture techniques with a virtual source element,” *IEEE Trans. Ultrason. Ferroelectr. Freq. Control*, vol. 45, no. 1, pp. 196–207, 1998.
- [14] S. I. Nikolov and J. A. Jensen, “3D synthetic aperture imaging using a virtual source element in the elevation plane,” *2000 IEEE Ultrason. Symp. Proceedings. An Int. Symp. (Cat. No.00CH37121)*, vol. 2, 2000.
- [15] M. H. Bae, “A study of synthetic-aperture imaging with virtual source elements in B-mode ultrasound imaging systems,” *IEEE Trans. Ultrason. Ferroelectr. Freq. Control*, vol. 47, no. 6, pp. 1510–1519, 2000.
- [16] S. I. Nikolov and J. A. Jensen, “Virtual ultrasound sources in high-resolution ultrasound imaging,” in *SPIE – Progress in biomedical optics and imaging*, 2002, vol. 4687, pp. 395–405.
- [17] M. C. Hemmsen, T. Kjeldsen, L. Lassen, C. Kjær, B. Tomov, J. Mosegaard, and J. A. Jensen, “Implementation of synthetic aperture imaging on a hand-held device,” *2014 IEEE Int. Ultrason. Symp. Proc.*, pp. 2177–2180, 2014.
- [18] BK Ultrasound, “L14-5/38 Linear,” <http://bkultrasound.com/ultrasonix/transducers/l14-538-linear>.
- [19] J. A. Jensen, “Field: A Program for Simulating Ultrasound Systems,” *Med. Biol. Eng. Comput.*, vol. 34, no. 1, pp. 351–353, 1996.
- [20] CIRS, “Multi-Purpose Multi-Tissue Ultrasound Phantom,” <http://www.cirsinc.com/products/modality/67/multi-purpose-multi-tissue-ultrasound-phantom>.
- [21] R. S. C. Cobbold, *Foundations of Biomedical Ultrasound*. Oxford University Press, 2007.
- [22] M. C. Van Wijk and J. M. Thijssen, “Performance testing of medical ultrasound equipment: Fundamental vs. harmonic mode,” *Ultrasonics*, vol. 40, no. 1–8, pp. 585–591, 2002.
- [23] K. Chen, H. S. Lee, and C. G. Sodini, “A Column-Row-Parallel ASIC Architecture for 3-D Portable Medical Ultrasonic Imaging,” *IEEE J. Solid-State Circuits*, vol. 51, no. 3, pp. 738–751, 2016.

Chapter 4

A Front-end ASIC with Receive Sub-Array Beamforming Integrated with a 32×32 PZT Matrix Transducer for 3-D Transesophageal Echocardiography

*C. Chen, Z. Chen, **D. Bera**, S.B. Raghunathan, M. Shabanimotlagh, E. Noothout, Z.Y. Chang, J. Ponte, C. Prins, H.J. Vos, J.G. Bosch, M.D. Verweij, N. de Jong, M.A.P. Pertijs, "A front-end ASIC with receive sub-array beamforming integrated with a 32×32 PZT matrix transducer for 3-D transesophageal echocardiography," IEEE J. Solid-State Circuits, vol. 63, no. 1, pp. 1–13, 2017.*

Chapter 4

This paper presents a power- and area-efficient front-end ASIC that is directly integrated with an array of 32×32 piezoelectric transducer elements to enable next-generation miniature ultrasound probes for real-time 3-D transesophageal echocardiography. The $6.1 \times 6.1 \text{ mm}^2$ ASIC, implemented in a low-voltage $0.18 \text{ }\mu\text{m}$ CMOS process, effectively reduces the number of receive cables required in the probe's narrow shaft by 9-fold with the aid of 96 delay-and-sum beamformers, each of which locally combines the signals received by a sub-array of 3×3 elements. These beamformers are based on pipeline-operated analog sample-and-hold stages, and employ a mismatch-scrambling technique to prevent the ripple signal associated with mismatch between these stages from limiting the dynamic range. In addition, an ultra-low-power LNA architecture is proposed to increase the power-efficiency of the receive circuitry. The ASIC has a compact, element-matched layout, and consumes only 0.27 mW/channel while receiving, which is lower than the state-of-the-art. Its functionality has been successfully demonstrated in 3-D imaging experiments.

5~7 mm

Gastroscopic tube ($\Phi \sim 5$ mm) containing < 200 coaxial cables connecting to the mainframe

2-D Transducer Matrix

Front-end ASIC

96

864

LNA

Delay line

PGA

3x3 Sub-array

TX

64

RX

96

2-D TEE probes are widely used in clinical practice. They employ a 1-D phased-array transducer to obtain cross-sectional images of the heart. However, such 2-D images often fall short in providing comprehensive visual information for complex cardiac interventions, such as minimally-invasive valve replacements and septal-defect closures. Appropriate real-time 3-D imaging would be very beneficial for improving the success rate of such procedures [1].

59

Chapter 4

[2]. To enable real-time 3-D imaging, a 2-D phase array is required. For an array of aperture size $D \times D$, the achievable signal-to-noise ratio (SNR) and the lateral resolution both improve linearly with D . Therefore, it is desirable to make full use of the available array aperture within the probe tip ($5 \times 5 \text{ mm}^2$). In addition, the pitch of the transducer elements should not exceed half of the acoustic wavelength (λ) to minimize grating lobes and to ensure proper spatial imaging resolution [3]. For a 2-D array with a center frequency of 5 MHz, this corresponds to a pitch of $150 \text{ }\mu\text{m}$, leading to at least 32×32 elements. Accommodating the corresponding number of micro-coaxial cables within the narrow gastroscopic tube is difficult or even impossible. Decreasing the aperture size to reduce the number of channels will lead to a significant deterioration in both the SNR and the lateral resolution. As a result, channel reduction should be performed locally to reduce the number of cables with the aid of miniaturized in-probe electronics [4].

A variety of approaches have been proposed to reduce the cable count in endoscopic and catheter-based ultrasound systems. Part of the beamforming function, which is conventionally performed in the external imaging system to achieve spatial directivity and enhance the signal-to-noise ratio, can be moved into the probe [5, 6]. Time-division multiplexing approaches have been applied in [7, 8] to allow multiple elements to share a single cable. Solutions based on element-switching schemes [9, 10] have also been reported. All these approaches rely on the realization of a front-end ASIC that is closely integrated with the transducer array.

Design of such front-end ASICs is challenging in several aspects. First, the power consumption of the ASIC, which contributes to the overall self-heating of the probe, should be kept below an estimated 0.5 W [11], to avoid excessive tissue temperature rise [12]. This translates to 0.5 mW/element for a 1000-element array and is beyond the state-of-the-art of front-end ultrasound ASICs, which consume at least 1.4 mW/element [10, 13, 14]. Another challenge comes from the dense interconnection between the ASIC and the transducer array. Direct transducer-on-chip integration is desired, as it not only helps to get a small form factor, but also reduces the parasitic interconnect capacitance added to each transducer element. This calls for an element-matched ASIC layout, with a pitch identical to that of transducer elements. As a result, a highly compact circuit implementation for the ASIC is called for. Prior works [13, 15] compromised somewhat on the imaging quality by opting for a slightly larger pitch. Indirect transducer-to-chip integration via interposer PCBs [6, 10] allows the use of a different pitch for the transducer array and the ASIC. However, the limited space within the TEE probe tip precludes this option.

In this paper, we present a front-end ASIC that is optimized in both system architecture and circuit-level implementation to meet the stringent requirements of 3-D TEE probes [16]. It is directly integrated with an array of 32×32 piezoelectric transducer elements, which are split into a transmit and a receive array to facilitate the power and area optimization of the ASIC [17]. The receive elements are further divided into 96 sub-arrays, each with a switched-capacitor-based beamformer, to realize a 9-fold cable reduction. Besides, an ultra-low-power

LNA architecture [18], which incorporates an inverter-based OTA with a bias scheme tailored for ultrasound imaging, is proposed to increase the power-efficiency of the receive circuitry, while keeping the area compact. In addition to that, a mismatch-scrambling technique is applied to mitigate the effects of mismatch between the beamformer stages, and thus improve the overall dynamic range of the ASIC while receiving. These circuit techniques, while designed for PZT matrix transducers, are also relevant for other types of ultrasound transducers, such as capacitive micromachined ultrasonic transducers (CMUTs). The functionality of the ASIC as well as the effectiveness of the proposed techniques have been successfully demonstrated by imaging experiments.

The paper is organized as follows. Section 4.2 describes the proposed system architecture. Section 4.3 discusses the details of the circuit implementation. Experimental results are presented in Section 4.4. Conclusions are given at the end of the paper.

4.2. System Architecture

4.2.1. Transducer Matrix Configuration

In conventional ultrasound probes, each transducer element is used both as transmitter and receiver. A high-voltage CMOS process is then needed to generate the transmit pulses of typically tens of Volts [14]. The integration density of high-voltage processes is generally lower than that of their low-voltage counterparts with the same feature size, which is disadvantageous for ASICs that directly interconnect with 2-D transducer arrays with a tiny element pitch.

In this work, we use an array of 32×32 PZT elements with separate transmit and receive elements (Fig. 2). An 8×8 central sub-array is directly wired out to transmit channels in the external imaging system using metal traces in the ASIC that run underneath 96 un-connected elements to bond-pads on the chip's periphery. These traces are not connected to any junctions in the substrate, and can hence support high transmit voltages provided that they are sufficiently spaced to prevent dielectric breakdown and routed in the top metal layers to minimize capacitive coupling to the substrate. All other 864 elements are connected directly to on-chip receiver circuits, whose outputs are fed to the imaging system's receive channels.

The use of a small central transmit array helps in reducing the overall cable count as well as obtaining a large opening angle while receiving. With respect to a conventional array configuration in which each transducer element is used for both transmit and receive, our scheme trades lateral resolution for a higher frame rate. In our scanning procedure, the transmitter is used to generate only a few wide beams, illuminating an area that can accommodate a number of parallel receive beams per transmit pulse, thus yielding a high frame rate. On the other hand, it should be also ensured that the generated acoustic pressure is adequate for the target imaging depth. According to our numerical simulations in PZFlex (Weidlinger Associates Inc., Mountain View, CA, USA), 64 elements should be capable to

Chapter 4

generate sufficient pressure for an imaging depth up to 10 cm. Moreover, despite the missing elements in the receiver aperture, the point spread function (PSF) is comparable with a fully-populated receiver, as shown by simulations in [19]. This configuration allows the use of a dense low-voltage CMOS technology, thus saving power and circuit area. Compared to [13], which uses the majority of elements to transmit and a sparse array to receive, it achieves better receiving sensitivity as well as lower side-lobes. Moreover, it also helps to reduce the overall in-probe heat dissipation, as transmit circuits normally consume more power [10].

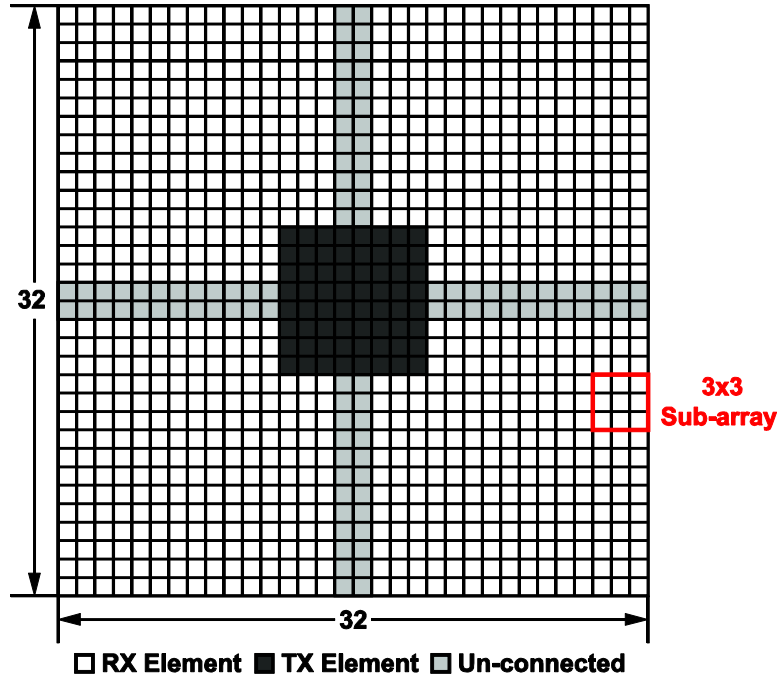


Fig. 2 Transducer matrix configuration.

The transducer array was constructed by dicing a bulk piezo-electrical material (CTS 3203 HD) into a matrix. It is directly mounted on top of the front-end ASIC using the PZT-on-CMOS integration scheme described in [11]. The PZT matrix measures $4.8 \text{ mm} \times 4.8 \text{ mm}$ with an element pitch of $150 \text{ }\mu\text{m}$ and a dicing kerf width of $20 \text{ }\mu\text{m}$. It was designed for a center frequency of 5 MHz and a 50% bandwidth (3.75 MHz ~ 6.25 MHz).

4.2.2. Sub-array Beamforming in Receive

The cable-count reduction approach that we adopted in this work is to perform partial receive beamforming in the ASIC. The basic principle of ultrasound beamforming is to apply appropriate relative delays to the received signals in such a way that ultrasound waves coming from the focal point arrive simultaneously and can be constructively combined. Full-array beamforming for 32×32 transducer elements is impractical for circuit implementation due to the large delay depth required for each element, which is typically a few microseconds. The

sub-array beamforming scheme [5], also known as “micro-beamforming” [17], mitigates this issue by dividing the beamforming task into two steps. A coarse delay that is common for all elements within one sub-array is applied in the external imaging system, while only fine delays for the individual elements (less than 1 μ s) is applied by sub-array beamformers in the ASIC, which significantly reduces the implementation complexity of the required on-chip delay lines.

The sub-array size is determined based on the following concerns. First, in order to keep the symmetry of the beamforming in lateral and elevation directions, a square sub-array is desired. Besides, a larger sub-array brings a more aggressive cable-count reduction, but comes at the cost of an elevated grating-lobe level and a greater maximum fine delay in the sub-array beamformers. We selected a 3×3 configuration to achieve a reasonable acoustic imaging quality, while reducing the number of cables by a factor of 9 [20]. Accordingly, the 864 receive elements of the transducer matrix are divided into 96 sub-arrays and interfaced with 96 sub-array receiver circuits in the ASIC.

The fine delays are programmable in steps of 30 ns up to 210 ns, allowing the sub-array’s directivity to be steered over angles of 0° , $\pm 17^\circ$, and $\pm 37^\circ$ in both azimuthal and elevation directions [11]. All sub-arrays can be programmed identically, which is appropriate for far-field beamforming and requires loading of only 9 delay settings into the ASIC, which has a negligible impact on the frame rate. The ASIC is also equipped with a mode in which all sub-arrays can be programmed individually (i.e. 96×9 settings), allowing near-field focusing at the expense of a longer programming time, and hence a slightly slower frame rate.

4.3. Circuit Implementation

Fig. 3 shows the schematic of a 3×3 sub-array receiver. It consists of 9 LNAs, 9 buffers, 9 analog delay lines, a programmable-gain amplifier (PGA) and a cable driver. A pair of protection diodes are implemented at the input of the LNA to prevent the input from exceeding the supply voltages by more than a diode drop. The LNA output is AC-coupled to a flipped source follower buffer that drives the analog delay line. The joint output of all 9 analog delay lines is then amplified by the PGA. A cable driver buffers the output signal of the PGA to drive the micro-coaxial cable connecting to the imaging system. A local bias circuit (not shown) is implemented within each sub-array.

The echo signals received by the transducer elements have a dynamic range of about 80 dB, 40 dB of which is associated with the fact that echoes from deeper tissue are attenuated more along their propagation path. The gains of the LNA and the PGA are programmable to compensate for this attenuation. The LNA is optimized for a low noise figure (< 3 dB) and provides a voltage gain up to 24 dB, to attenuate the impact of noise of the subsequent stages at small signal levels. The gain can be reduced to -12 dB and 6 dB to avoid output saturation at high signal levels. The PGA provides an additional switchable gain with finer steps (0, 6, 12 dB) to interpolate between the gains steps of the LNA. Thus, an overall dynamic range of more than

Chapter 4

80 dB, which is sufficient for TEE imaging, can be achieved.

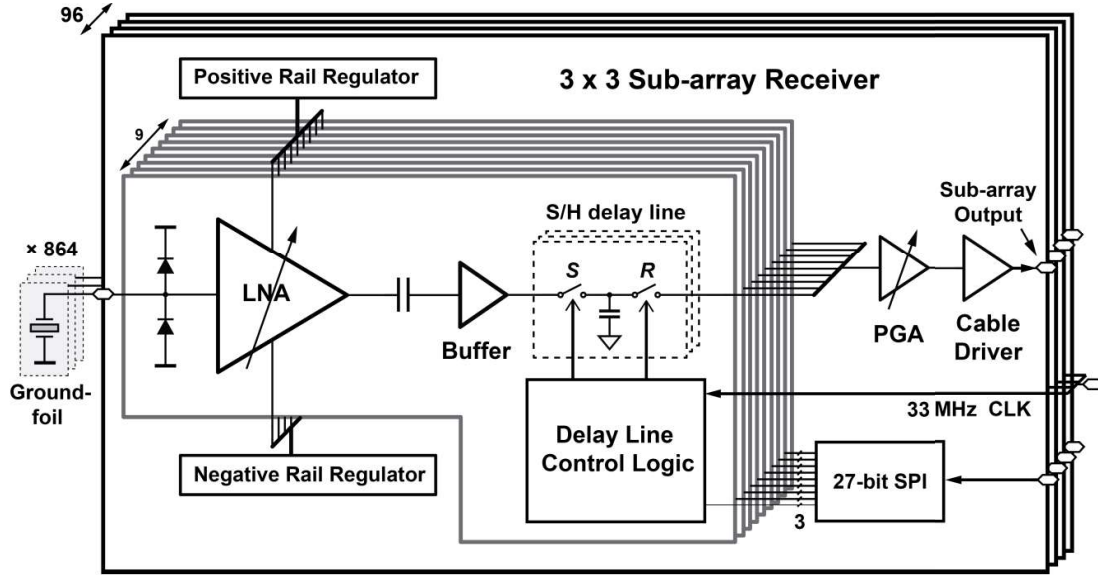


Fig. 3 Schematic of the 3×3 sub-array receiver.

As described in Section I, all the above circuits, along with their biasing and digital control circuits, must be implemented within the area of a 3×3 sub-array, i.e. $450 \mu\text{m} \times 450 \mu\text{m}$, while consuming less than 4.5 mW. Dedicated circuit techniques have been applied to meet these requirements, which will be discussed in this section.

4.3.1. LNA

The choice of the ultrasound LNA topology is dictated by the electrical impedance of the target transducer. Trans-impedance amplifiers (TIA) are widely used in readout ICs for CMUT transducers because of their relatively high impedance [21]. However, a similarly-sized PZT transducer has a much lower impedance around the resonance frequency, typically a couple of $\text{k}\Omega$ s for our transducers (Fig. 4). In view of this, the TIA topology falls short in achieving an optimal noise/power trade-off, since creating a low enough input-impedance requires extra power spent on increasing the open-loop gain, rather than on suppressing the input-referred noise [18]. In this work, instead, we use a capacitive-feedback voltage amplifier, shown in Fig. 5, which offers a mid-band voltage gain of $A_M = C_I / C_F$. Its input impedance is dictated by the input capacitor C_I and can be easily sized to tens of $\text{k}\Omega$ s within the transducer bandwidth, so as to sense the transducer's voltage rather than its current.

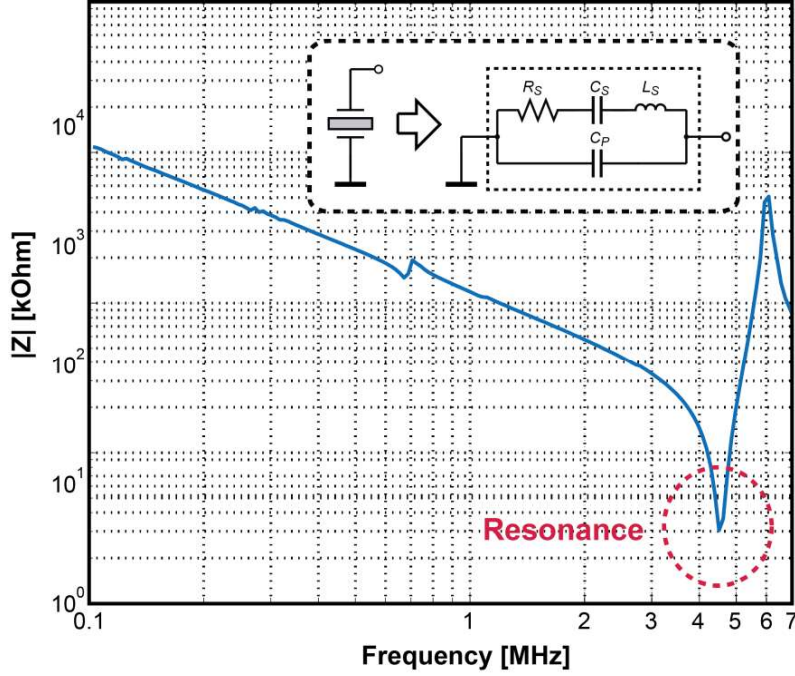


Fig. 4 The measured impedance of a $130 \mu\text{m} \times 130 \mu\text{m}$ PZT transducer element (i.e. $150 \mu\text{m}$ pitch with $20 \mu\text{m}$ kerf) and its equivalent electrical model.

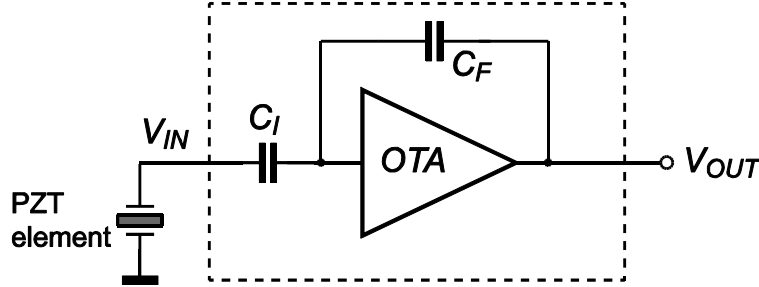


Fig. 5 The proposed LNA architecture.

A current-reuse OTA based on a CMOS inverter is employed to enhance the power-efficiency of the LNA. In previous inverter-based designs [22], extra level-shifting capacitors (C_{LS}) are used to independently bias the NMOS and PMOS transistors, as shown in Fig. 6(a). These level-shifting capacitors and the associated parasitic capacitors at the virtual ground node form a capacitive divider, which attenuates the input signal and thus increases the input-referred noise of the LNA. Enlarging C_{LS} helps in reducing this noise penalty, at the cost of increased die area. In this work, the level-shifting capacitors are eliminated by applying a split-capacitor feedback network [18, 23]. As shown in Fig. 6(b), the input bias points for the NMOS and PMOS transistors are de-coupled by splitting the input and feedback capacitors into two equal pairs, which maintains the same mid-band gain C_I / C_F and the same input impedance.

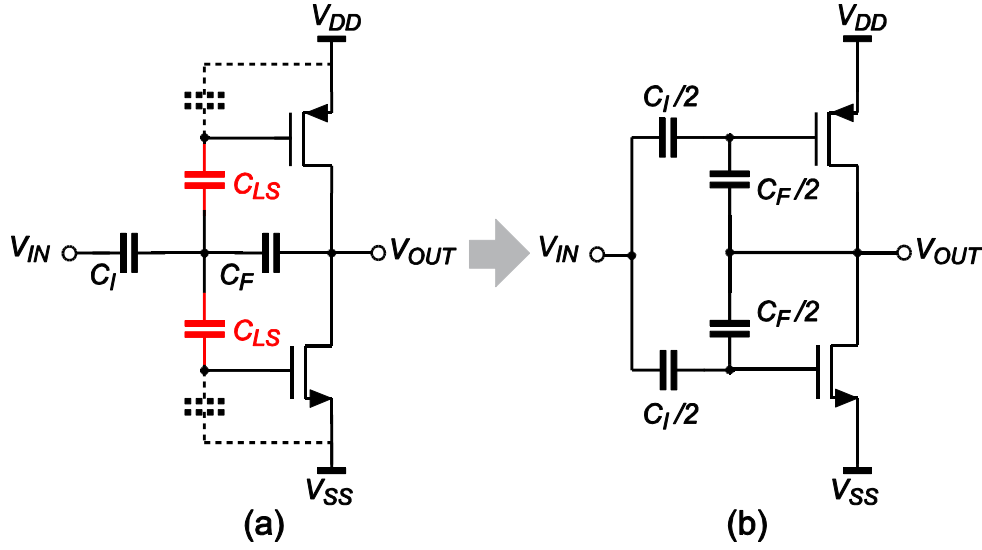


Fig. 6 Inverter-based OTA with split-capacitor feedback network.

To maximize the output swing, the bias voltage of the inverter-based OTA should be properly defined. This is usually achieved with the aid of a DC control loop, in which a slow auxiliary amplifier keeps the output at the desired operating point [22]. However, such a DC control loop will recover too slowly from disturbances caused by the high-voltage pulses propagating across the ASIC during the transmit phase. Therefore, instead, we dynamically activate the bias control loop in synchronization with the transmit/receive (TX/RX) cycles of the ultrasound system, as shown in Fig.7. During the TX phase, the input of the LNA is grounded and the inverter is essentially auto-zeroed, while the auxiliary amplifier drives the gate of the NMOS transistor so as to bias the output at mid-supply. During the RX phase, the auxiliary amplifier is disconnected, and both its inputs are shorted to the mid-supply. Meanwhile, the LNA starts receiving the echo signal by operating at the “memorized” bias points. Given that the typical TX/RX cycle in cardiac imaging is relatively short, ranging from 100 μ s to 200 μ s, the bias voltage hardly drifts during the RX phase. The relatively large sizes of the input transistors ($W/L_N = 75/0.2$, $W/L_P = 60/0.2$), needed for flicker-noise reduction, also help to keep the bias voltages stable. The sample-and-hold operation associated with the auto-zeroing causes broadband white noise to be sampled on the gate of the NMOS transistor and held constant during the receive phase. Therefore, it appears as a small offset voltage that is superimposed on the “memorized” bias point during each transmit/receive cycle, and doesn’t deteriorate the in-band noise performance of the LNA. Moreover, it is further filtered out by the AC-coupler following the LNA and has no impact on the bias condition of succeeding stages.

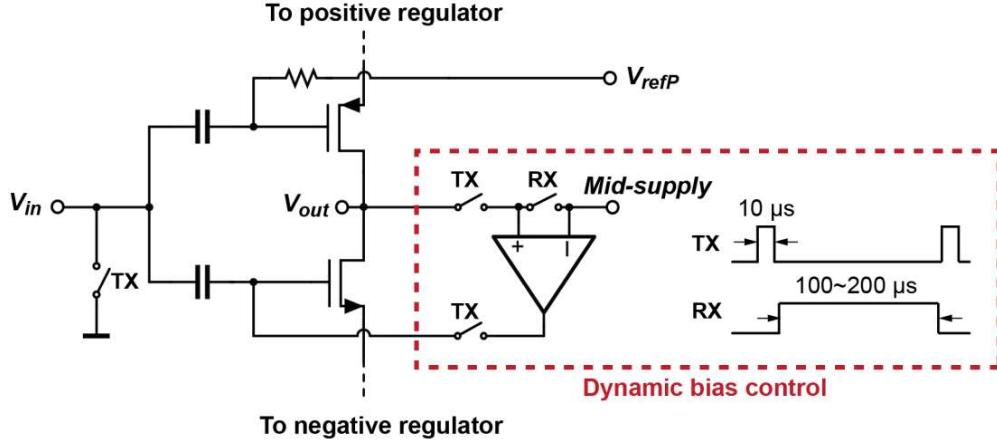


Fig. 7 Dynamic bias control scheme.

A well-known down-side of a single-ended inverter-based OTA is its poor power-supply-rejection ratio (PSRR) [24]. As the LNAs are closely integrated with high-frequency digital circuits for beamformer control, the supply line and the ground are inevitably noisy. To improve the PSRR, we generate two internal power rails within each sub-array by means of two regulators (REG_P and REG_N in Fig. 8) that are shared by the 9 LNAs of a sub-array. Given the fact that the loading currents of these regulators are known and approximately constant, their implementation can be kept rather simple to save area. A capacitor-less LDO based on a super source-follower [25], capable of providing a PSRR better than 40 dB at 5 MHz, is adopted as the topology for both regulators.

Fig. 8 shows the complete schematic of the proposed LNA. The inverter-based OTA is cascoded to ensure an accurate closed-loop gain, and input transistors M_1 and M_4 are biased in weak-inversion to optimize their current-efficiency. The bias voltage of M_1 , V_{refP} , which is derived from a diode-connected PMOS transistor via a high-impedance pseudo-resistor, is shared by the input gate of the positive-rail regulator REG_P . Thus, the bias current of the OTA can be defined by the difference of the reference currents ($I_{p1} - I_{p2}$) and the dimension ratio of M_1 and M_{p1} . In each channel, an unity-gain-connected inverter, implemented with long-channel transistors and consuming only 0.4 μA , is connected between the two regulated power rails to generate a mid-supply reference that is approximately 900 mV. The auxiliary amplifier for DC bias control is realized as a simple differential pair. With a current consumption of less than 1 μA , it is capable to settle within the 10 μs TX phase. A switchable capacitive feedback network, involving capacitors 14C and 7C that can be switched in or out under control of digital gain-control inputs of the ASIC, is implemented to provide the mentioned 3 gain levels for dynamic range enhancement. An explicit loading capacitor (not shown in Fig. 8) is added at the output of the LNA to limit its -3 dB bandwidth below 10 MHz.

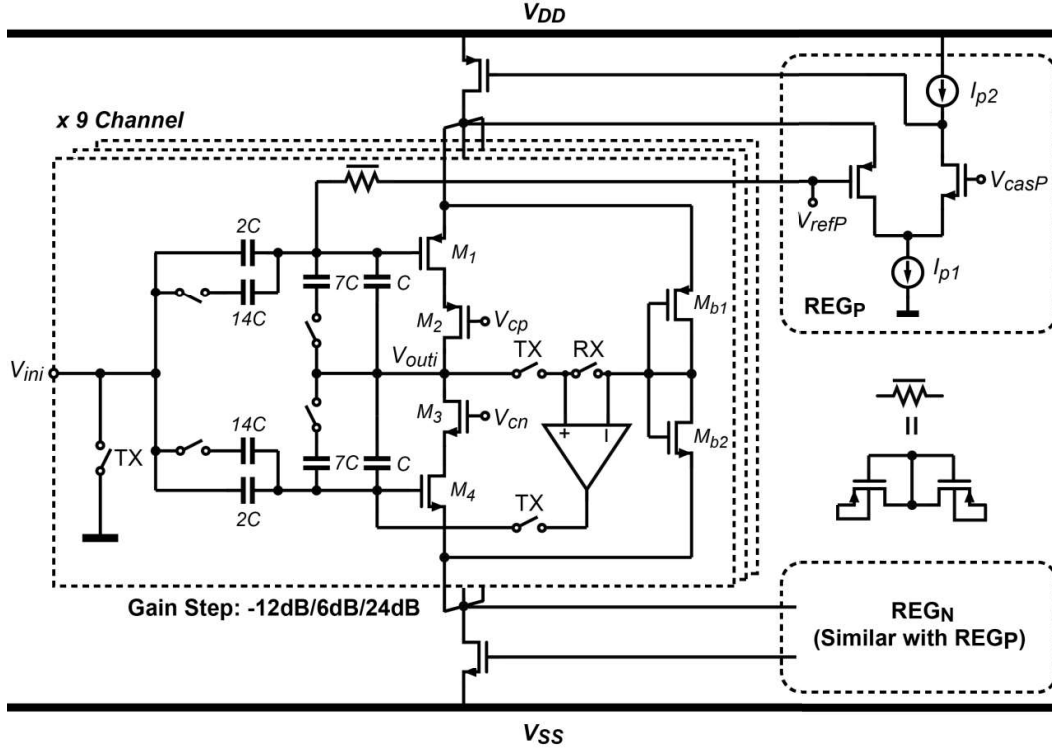


Fig. 8 Complete schematic of the LNA.

4.3.2. Sub-Array Beamformer

Fig. 9 shows the circuit implementation and timing diagram of the sub-array beamformer. It consists of 9 programmable analog delay lines, each of which is built from pipeline-operated S/H memory cells that run at a sampling rate of 33 MHz, corresponding to the target delay resolution of 30 ns. Due to the fact that the sampling rate is higher than the designed bandwidth of the LNA, the increase in the noise floor caused by aliasing is negligible.

The capacitor in each memory cell is carefully sized to ensure that the associated kT/C noise is not dominant, while meeting the area requirement. With 300 fF metal-insulator-metal (MIM) capacitors, an input-referred rms noise voltage of about 118 μ V is expected for each delay line, which is smaller than the output noise of the LNA at its highest gain setting.

The outputs of all 9 delay lines are passively joint together to sum up and average the charge sampled on the capacitors that are connected to the output node [11]. Compared to voltage-mode summation [26, 27], this scheme eliminates the need for a summing amplifier, and is thus more compact and power-efficient. However, a potential source of errors is the residual charge stored on the parasitic capacitance at the output node, which causes a fraction of the output of the previous clock cycle to be added to the output signal. This is equivalent to an undesired first-order infinite-impulse-response low-pass filter. While this filtering can be eliminated by periodically removing the charge from the output node using a reset switch [11], here we

A Front-end ASIC with Receive Sub-Array Beamforming

choose for the simpler solution of minimizing the parasitic capacitance at the output node. It can be shown that an acceptable signal attenuation within the bandwidth of 0-10 MHz of less than 3 dB is obtained if this parasitic is less than 20% of the total capacitance at the output node, which can be easily achieved with a careful layout.

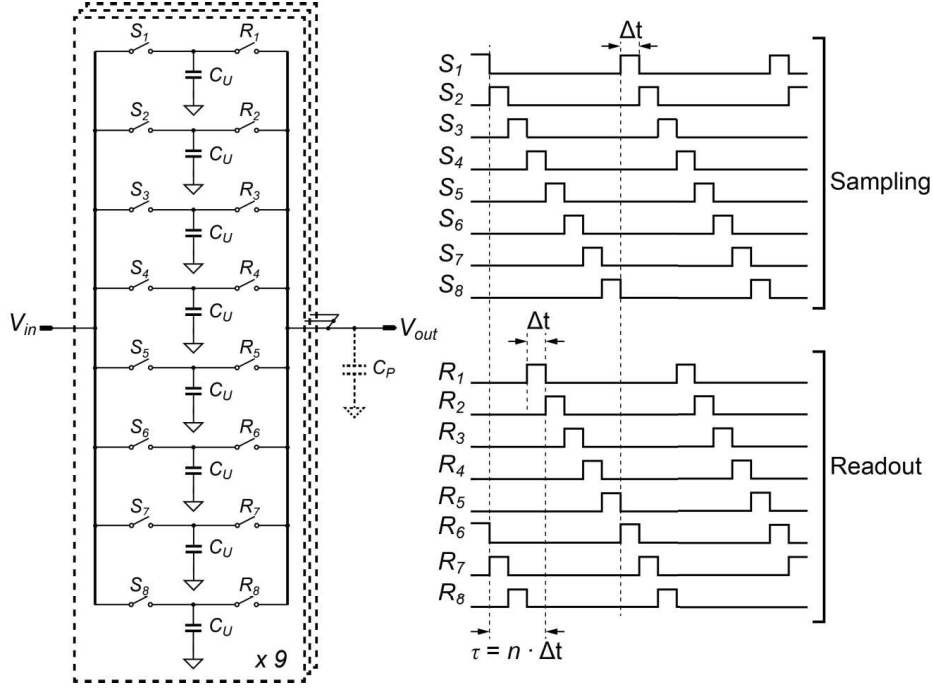


Fig. 9 Schematic and timing-diagram of the sub-array beamformer.

The control logic for programming the delay lines is also integrated within each sub-array. Its core is a delay stage index rotator that determines the sequence in which the memory cells are used, as conceptually shown in Fig. 10. The detailed circuit implementation is shown in Fig. 11. It consists of an 8-stage shift register (D_1 - D_8) in which the 4-bit binary indices of memory cells (1-8) are stored and rotated. Upon startup, register D_n is preset to n . D_1 stores the index of the memory cell used for sampling the input signals, while D_2 - D_8 store the indices of candidate memory cells for readout. A 3-bit selection code, provided by a built-in SPI interface, decides which of these candidates is used, allowing the delay of the individual delay line to be programmed. One-hot codes derived from the selected 4-bit binary indices are re-timed by non-overlapped clocks to control the sample/readout switches in the memory cells.

As mentioned in Section II, the SPI interfaces in all sub-arrays can be either loaded in parallel, or configured as a daisy-chain to load different delay-patterns to individual sub-arrays. With a 50 MHz SPI clock, only 0.54 μ s is needed to program the ASIC's delay pattern in the parallel mode, while for the daisy-chain mode it takes about 13 μ s (sub-arrays in each quadrant of the ASIC form one daisy-chain), leading to a 9% frame rate reduction for an imaging depth of 10

Chapter 4

cm. As such, the daisy-chain mode enables near-field focusing at the expense of a slightly slower frame rate.

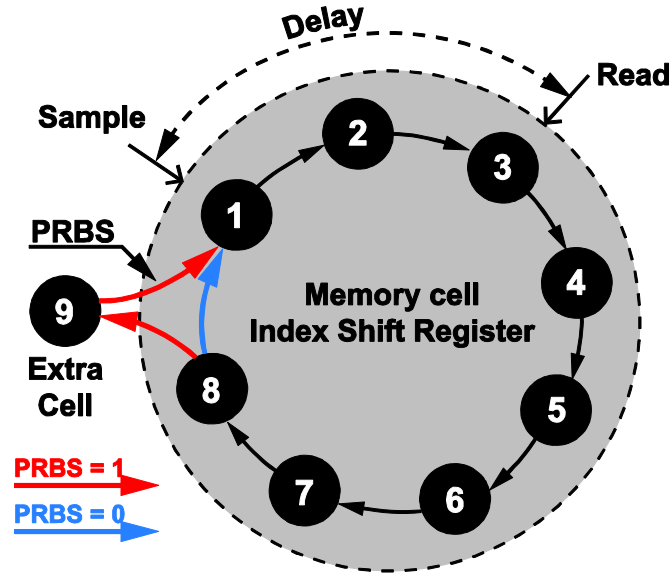


Fig.10 Operation principle of mismatch-scrambling.

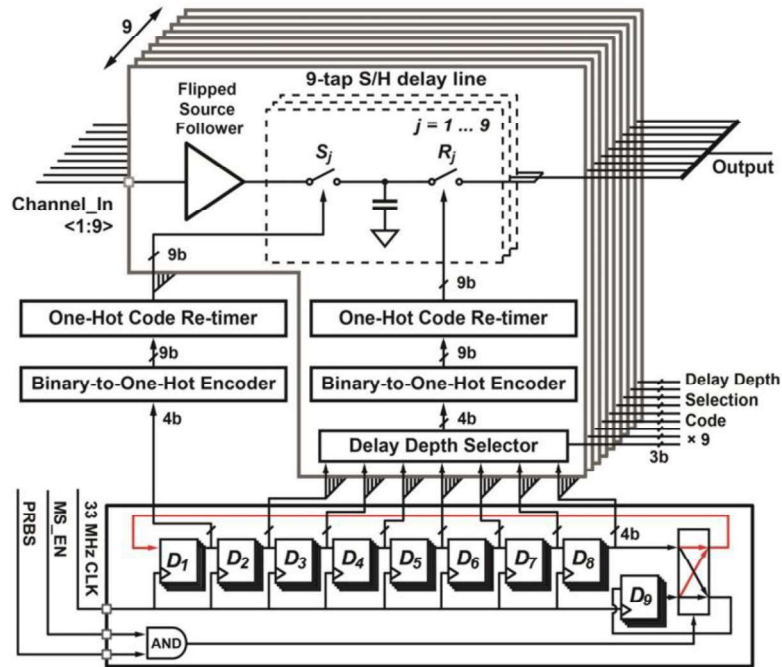


Fig. 11 Circuit implementation of the delay line control logic with mismatch-scrambling.

4.3.3. Mismatch-scrambling

The S/H memory cells suffer from charge injection and clock feed-through errors, the mismatch of which introduces a ripple pattern with a period of 8 delay steps (240 ns) at the output of the delay lines. Such ripple pattern manifests itself as undesired in-band tones in the output spectrum of the beamformer, which limits the dynamic range of the signal chain.

To mitigate this interference, we propose a mismatch-scrambling technique by adding an extra memory cell and a redundant index register D_9 , as shown in both Fig. 10 and Fig. 11. A pseudo-random number generator (PRNG) embedded in each sub-array generates a bit sequence (PRBS) that decides whether the index of D_8 or D_9 shifts into D_1 , while the other index shifts into D_9 . Thus, memory cells are randomly taken out and inserted back into the sequence. This operation randomizes the ripple pattern and converts the interfering tones into broadband noise. The mismatch-scrambling function can be switched on/off with a control bit (MS_EN in Fig. 11).

The PRNG in each sub-array is implemented as a 12-bit Galois linear-feedback shift register (LFSR) [28]. It can be re-configured as a shift register to allow the sequential loading of its initial state, i.e. the seeds. Similar to the daisy-chain mode of the delay-pattern SPI interface, these shift registers can also be cascaded to allow different seeds to be loaded into the individual sub-arrays. Applying a set of randomized seeds for all sub-arrays is expected to further de-correlate the sequences of memory cell rotation on the scale of the full-array. As a result, the excess noise generated by the scrambling process can be suppressed when the output signals of the sub-arrays are combined by the beamforming operation in the imaging system, thus improving the SNR.

4.3.4. PGA

Fig. 12 shows the schematic of the PGA, which is implemented as a current-feedback instrumentation amplifier [17, 29] with a single-ended output. It consists of a differential pair of super source followers with a tunable source-degeneration resistor R_S , which performs as a linearized trans-conductor, and a current mirror with a constant load resistor R_L , which converts the trans-conductor's output current to voltage. The voltage gain of the PGA is defined by the ratio of both resistors R_L/R_S . R_S is implemented as a switchable resistor array ranges from 6 k Ω to 18 k Ω , while R_L is constant (24 k Ω). To avoid using very large CMOS switches for getting small on-resistance, Kelvin connections are used to eliminate errors caused by the on-resistance of those switches (Fig. 12). Compensation capacitors (C_C) are added to ensure the loop stability. These capacitors are switched along with the gain settings from 800 fF at the lower gain setting to 400 fF at the highest gain setting. A differential topology is applied to improve the PGA's immunity to interference. The negative input terminal (V_{in-}) is connected to the output of a replica delay-line buffer, whose input node is AC-coupled to ground while sharing the same DC bias voltage with the other buffers.

Chapter 4

The PGA is sitting after the sub-array beamformer. Therefore, when comparing its noise contribution with preceding stages, the noise averaging effect [10] of the beamformer should be taken into account. It is designed to have an input referred noise density below $30 \text{ nV}/\sqrt{\text{Hz}}$ to prevent adding excess noise when referred to the input of the LNA.

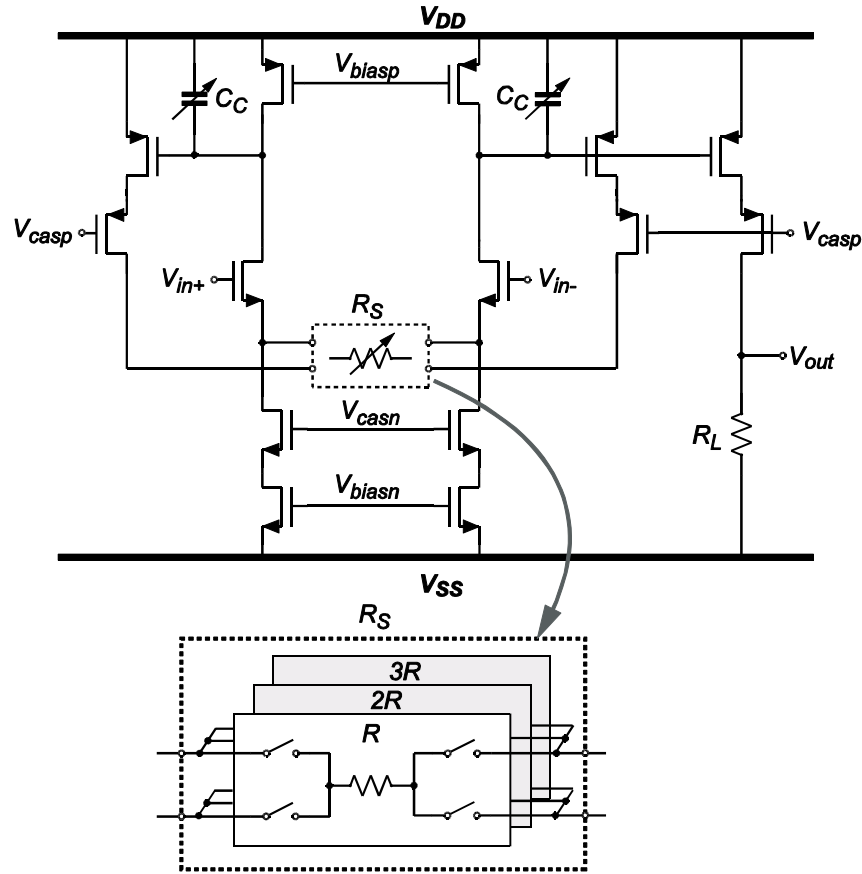


Fig. 12 Schematic of the PGA.

4.3.5. Cable driver

The cable driver is required to fan-out the output signal of each sub-array across a micro-coaxial cable with capacitance up to 300 pF. To maximize its power-efficiency, a class-AB super source follower [30], as depicted in Fig.13, is adopted as the topology for the cable driver. Instead of using a high-impedance pseudo-resistor to form a quasi-floating gate, the gate of the PMOS transistor is only connected to the bias circuit during the TX phase, but kept floating during the RX phase, similar to the dynamic DC bias scheme used in the LNA. When referred back to the input of the signal chain, the noise contribution of the cable driver is negligible as it's compressed by the gain of the PGA.

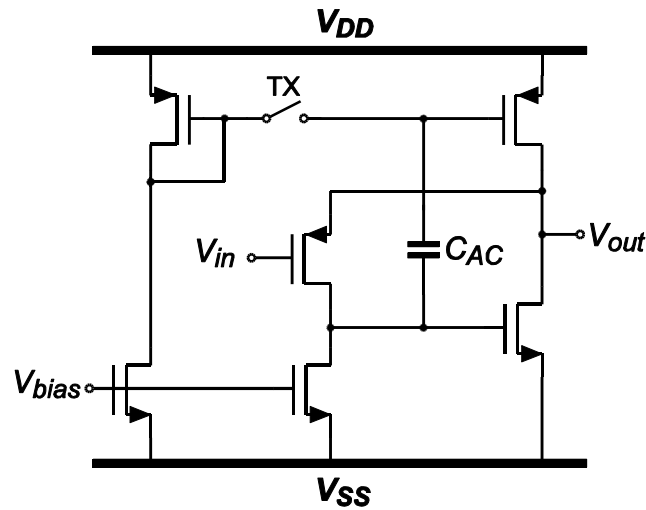


Fig. 13 Schematic of the cable driver.

4.4. Experimental Results

The ASIC has been realized in a $0.18\ \mu\text{m}$ low-voltage CMOS process with a total area of $6.1 \times 6.1\ \text{mm}^2$, as shown in Fig. 14(a). Fig. 14(b) presents a zoom-in view of one sub-array receiver that is matched to a 3×3 group of transducer elements with a pitch of $150\ \mu\text{m}$. While receiving, the ASIC consumes only 230 mW, which is less than half of the power budget for a 3-D TEE probe.

Fig. 15(a) shows a fabricated prototype with an integrated 32×32 PZT matrix transducer. The assembly has been bonded to a daughter PCB to facilitate acoustic measurements (Fig. 15(b)). A matching layer and ground foil are applied on top of the PZT matrix. The ground foil is directly connected to the ground potential of the ASIC via PCB traces. Bonding wires on the periphery of the ASIC are covered by a non-conductive epoxy layer for waterproof.

The ASIC's 96-channel sub-array outputs and 64-channel high-voltage transmit inputs are connected to a mother-PCB via micro-coaxial cables with a length of 1.5 m. The mother PCB is directly mounted on a programmable imaging system (Verasonics V-1 system, Verasonics Inc., Redmond, WA), which acquires the RF data from the ASIC and drives high-voltage pulses via metal traces in the ASIC to transmit elements in the transducer array. Counting in the required power-supply and digital control lines, the total number of cables required for connecting the ASIC to the imaging system is around 190.

Using this setup, the ASIC's electrical and acoustic performance have been characterized experimentally, the results of which are presented in this section.

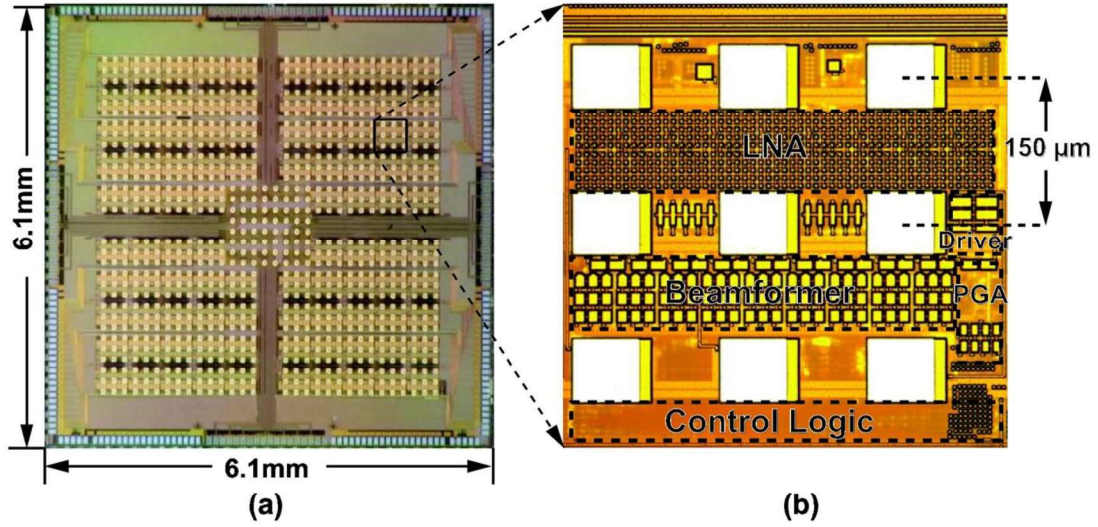


Fig. 14 (a) Micro-photograph of the ASIC; (b) Floor plan of one sub-array receiver. Bond-pads for transducer interconnection are implemented on top of the other circuits in the top layer metal.

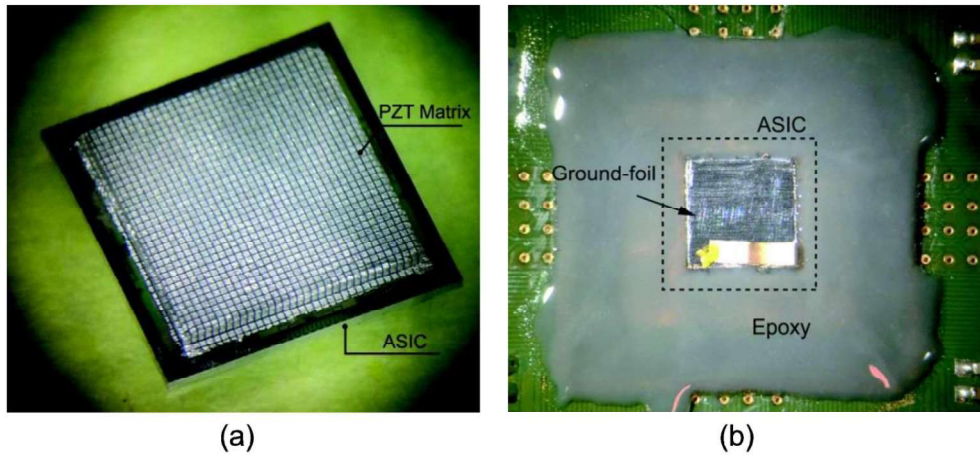


Fig. 15 (a) Photograph of a prototype ASIC with integrated 32×32 PZT matrix; (b) A prototype bonded on a daughter PCB for acoustic experiments.

4.4.1. Electrical characterization

The electrical performance of the proposed LNA architecture has been fully characterized and evaluated with a separate test IC [18]. It demonstrates a 9.8 MHz bandwidth, an 81 dB dynamic range and an input-referred noise density of $5.5 \text{ nV}/\sqrt{\text{Hz}}$ @ 5 MHz at its highest gain, while consuming only 0.135 mW per channel. When interfaced with an external, small PZT array that gives a receive sensitivity of about $10 \text{ μV}/\text{Pa}$, the LNA achieves a noise-efficiency factor (NEF) [31] that is $2.5 \times$ better than the prior state-of-the-art [14].

A Front-end ASIC with Receive Sub-Array Beamforming

Fig. 16 shows the measured transfer function of a 3×3 sub-array receiver in the ASIC, with a uniform delay pattern applied to the sub-array beamformer. Various combinations of LNA/PGA gain settings were applied to achieve a programmable mid-band gain ranging from -24 dB to 24 dB with a gain step of 6 dB. The measured absolute values of the mid-band gain levels are approximately 6 dB lower than the theoretical values of the LNA/PGA gain combinations, which can mainly be attributed to signal attenuation in the delay line buffers and cable drivers and to the attenuation associated with the parasitic capacitance at the beamformer's summing node. This deviation does not deteriorate the imaging quality, as long as an adequate SNR can be maintained at the sub-array output by an appropriate selection of gain settings. The -3 dB bandwidth is about 6 MHz, ranging from 0.3 MHz to 6.3 MHz. Note that the sinc-filtering effect of the sample-and-hold operation in the beamformer also contributes to the gain roll-off at higher frequencies, which introduces 4 dB extra attenuation at 16.5 MHz (half sampling frequency).

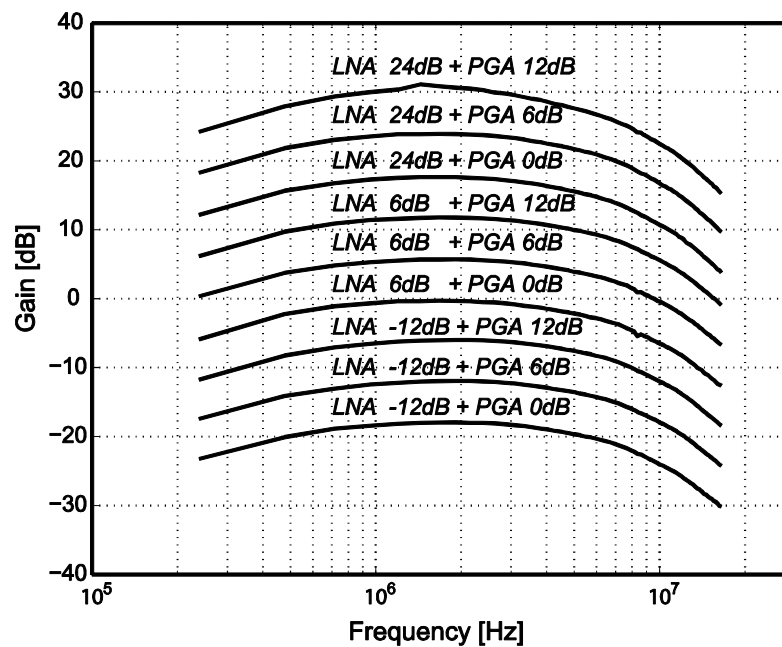


Fig. 16 Measured transfer functions of the ASIC with different combinations of LNA/PGA gain settings.

To investigate the output noise level of the sub-array receiver circuits, we use an ASIC without integrated transducer matrix, in which all bond-pads for transducer interconnection are electrically shorted to ground by means of wire bonding. With the highest LNA and PGA gain settings, the electrical output noise density of a 3×3 sub-array is measured as 120 nV/ $\sqrt{\text{Hz}}$ at 5 MHz. This is in good agreement with the simulated value of 106 nV/ $\sqrt{\text{Hz}}$. With a 300 mV maximum peak-to-peak output amplitude, the peak SNR at the highest gain setting thus found is about 51 dB.

Chapter 4

Fig. 17(a) shows the measured output noise spectrum without enabling the mismatch-scrambling function. Two interference tones appear at fractions of the sampling frequency ($f_s/8$, $f_s/4$), which dominate the noise floor and thus reduce the dynamic range. After enabling mismatch-scrambling (Fig. 17(b)), these tones get eliminated from the output spectrum, at the expense of a small increase in the noise floor.

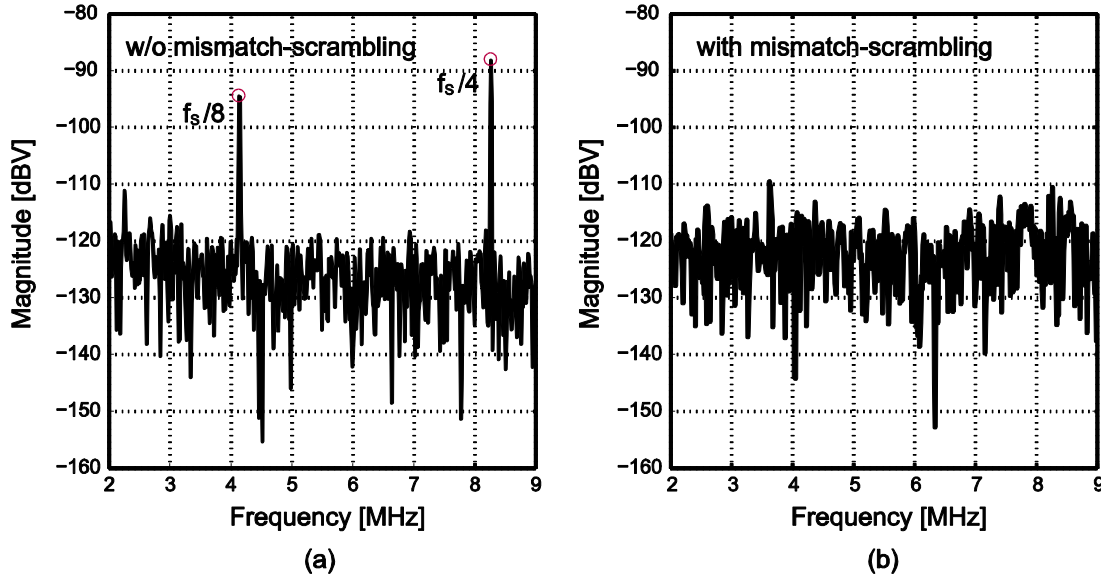


Fig. 17 Measured noise spectrum of the averaged output of 24 sub-arrays without (a) and with (b) mismatch-scrambling. LNA gain = 6 dB and PGA gain = 6 dB.

The noise power reduction associated with the system-level beamforming has been measured by combining the sub-array output signals acquired using the Verasonics system. Fig. 18 shows the measured rms noise voltage after beamforming as a function of the number of sub-arrays. Ideally, if the noise at the outputs of the sub-arrays is uncorrelated, the noise power after beamforming should decrease inversely proportionally to the number of sub-arrays involved. Without mismatch-scrambling, this is not the case, because the sub-array outputs signals are dominated by (correlated) mismatch-related tones. With mismatch-scrambling enabled, the noise level shows the expected improvement, i.e. decreasing at a slope close to 10 dB/dec, provided that randomized seeds are delivered to the different pseudo-range number generators. With the same seed used in all sub-arrays, the tones disappear from the output spectrum, but the randomized mismatch signals of different sub-array are still correlated and hence are not reduced by the averaging operation of the system-level beamformer.

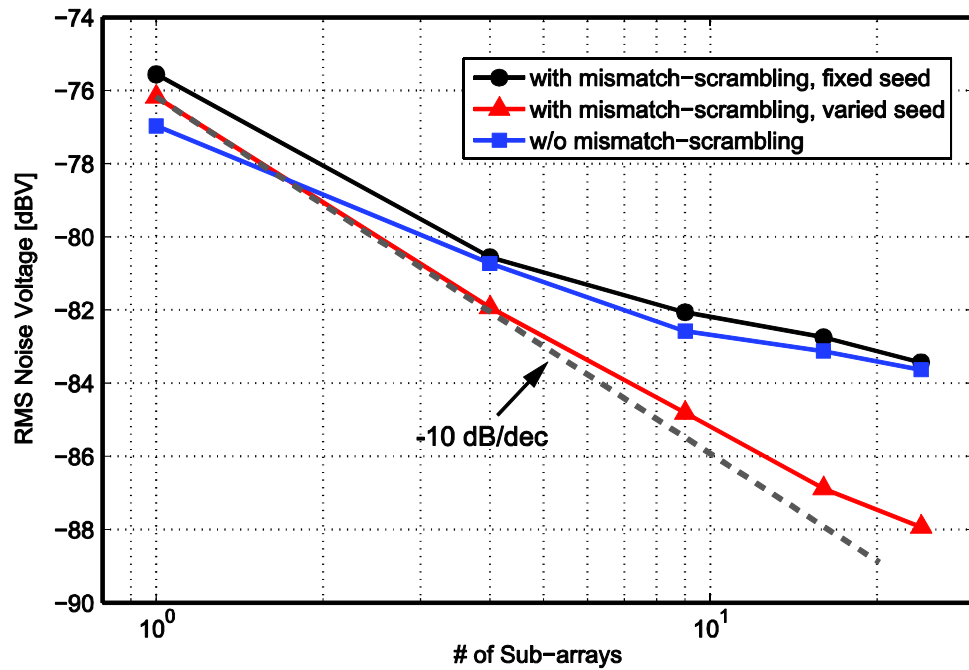


Fig. 18 Measured rms noise voltage after post-beamforming as a function the number of sub-arrays. Noise is integrated over a bandwidth of 2.5 MHz - 7.5 MHz. LNA gain = 6 dB and PGA gain = 6 dB.

Table 1 summarizes the measured electrical performance of the ASIC. A system-level comparison with reported works on ASICs for 3-D ultrasound imaging is given in Table 2. Our ASIC achieves both the best power-efficiency in receiving and the highest integration density.

Table 1. ASIC performance summary

RX	Supply voltage	Analog: 1.8 V	Digital: 1.4 V
	Total power	228.9 mW	
	-3 dB Bandwidth	6 MHz	
	Input-referred noise density @ 5 MHz*	w/o mismatch-scrambling: 1.0 mPa/ $\sqrt{\text{Hz}}$ with mismatch-scrambling: 2.0 mPa/ $\sqrt{\text{Hz}}$ (worst case**)	
	RX sensitivity	$\sim 5 \mu\text{V}/\text{Pa}$ @ LNA input	
	Gain steps	-12/-6/0/6/12/18/24/30/36 dB	
	HD2	43 dBc @ 300 mV peak-to-peak output, 5 MHz	
TX	Max. peak-to-peak TX pulse voltage	50 V (Generated by Verasonics and transmitted via the ASIC)	
	TX efficiency	$\sim 6 \text{ kPa}/\text{V}$ @ 5 cm	

*Calculated as sub-array output noise density / measured voltage gain at 5 MHz.

**The measured input-referred noise with the mismatch-scrambling function enabled varies with different delay patterns because of a systematic mismatch in the layout of S/H delay lines, which could be optimized by a better layout.

Table 2. System-level comparison with prior works

	[5]	[12]	[9]	[10]	This work
Process	1.5 μm HV	0.25 μm HV	0.18 μm HV	0.18 μm LV	0.18 μm LV
Transducer	CMUT	CMUT	CMUT	PZT	PZT
Array size	16 \times 16	32 \times 32	16 \times 16	9 \times 12	32 \times 32
Center freq.	5 MHz	5 MHz	5 MHz	5 MHz	5 MHz
Element Pitch	250 μm	250 μm	250 μm	200 μm	150 μm
Pitch $\leq \lambda/2$?	No	No	No	No	Yes
Beamform Function	TX	TX	Off-chip	RX Sub-array	RX Sub-array
# of TX el.	256	960	256	N/A	64
# of RX el.	32	64	256	81	864
Imaging depth	7.5 cm	7.5 cm	7.5 cm	N/A	10 cm
Volume rate	5* volume/s	5* volume/s	62.5 volume/s	N/A	40 – 300** volume/s
Integration method	Flip-chip bonding Via Interposer	Flip-chip bonding	Flip-chip bonding Via Interposer	Direct Integration	Direct Integration
ASIC size	10 \times 6 mm ²	9.2 \times 9.2 mm ²	6 \times 5.5 mm ²	3.2 \times 3.8 mm ²	6.1 \times 6.1 mm ²
RX power/el.	9 mW	4.5 mW	1.4 mW	0.44 mW	0.27 mW

*Limited by the PCIe interface between Verasonics and the host PC.

**Estimated frame rate for a real-time implementation on a Verasonics Vantage system.

4.4.2. Acoustic experiments

The fabricated prototype shown in Fig. 15 was immersed in a water tank (Fig. 19) for the evaluation of its acoustic performance. To measure the transmit efficiency of the center sub-array, all 64 TX elements were driven simultaneously by the Verasonics system and the pressure was measured at 5 cm using a hydrophone. With a 50 V excitation, a transmit pressure of 300 kPa was measured, leading to a transmit efficiency of about 6 kPa/V.

To characterize the receive beam-steering function of the ASIC, a single element transducer of 0.5-inch diameter and 5 MHz central frequency (Olympus) has been used as an external source, which generates a quasi-continuous plane wave at the surface of the prototype transducer. The prototype was mounted on a rotating stage and turned from -50° to $+50^\circ$ with a steps of 2° . The delays of sub-array beamformers in the ASIC were programmed successively to steer the sub-arrays maximum sensitivity towards 0° , 17° and 37° . The corresponding measured sub-array beam-profiles, shown in Fig. 20, are in good agreement with expectations, with the peak of the beams corresponding well to the programmed steering angles.

A Front-end ASIC with Receive Sub-Array Beamforming

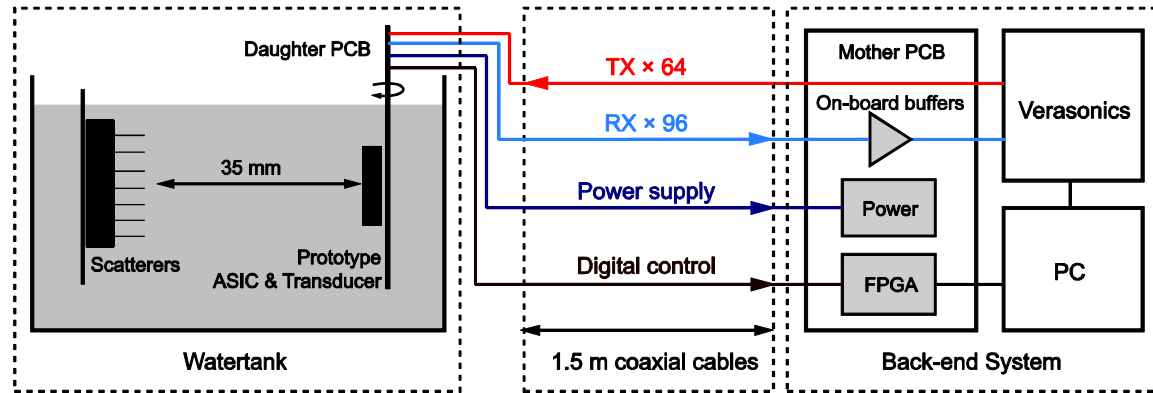


Fig. 19 Schematic diagram of the acoustic experiment setup. For the beam-steering measurements and the characterization of transmit pressure, scatterers were replaced by single-element transducers and a hydrophone, respectively.

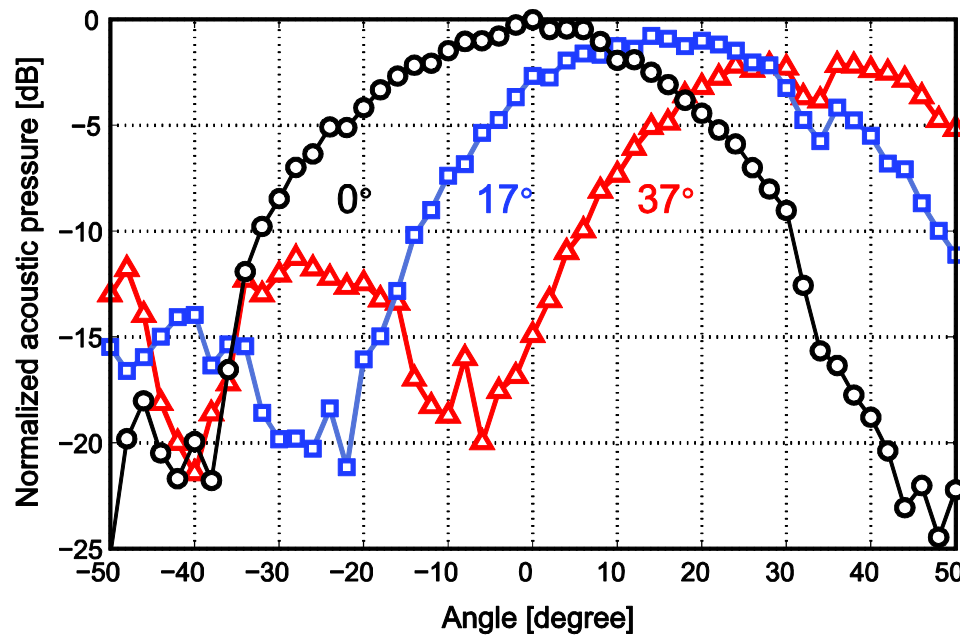


Fig. 20 Measured sub-array beam-profile for steering angles of 0°, 17° and 37°.

4.4.3. Imaging results

To demonstrate the 3-D imaging capability of the prototype, a pattern of seven point scatterers (six steel balls and one needle), forming a letter “M” (Fig. 21(a)), was placed at a distance of approximately 35 mm in front of the transducer array. A diverging wave was transmitted from the prototype, using a pulse of 18 V (peak-to-peak), generated by the Verasonics systems and applied to the transmit sub-array through the connections on the ASIC. A 3-D volume image was re-constructed by combining the sub-array output signals recorded using the Verasonics

Chapter 4

system from multiple transmit-receive events, and rendered to get a frontal view of the point scatterers (Fig. 21(b)), which clearly shows the layout of the scatterers.

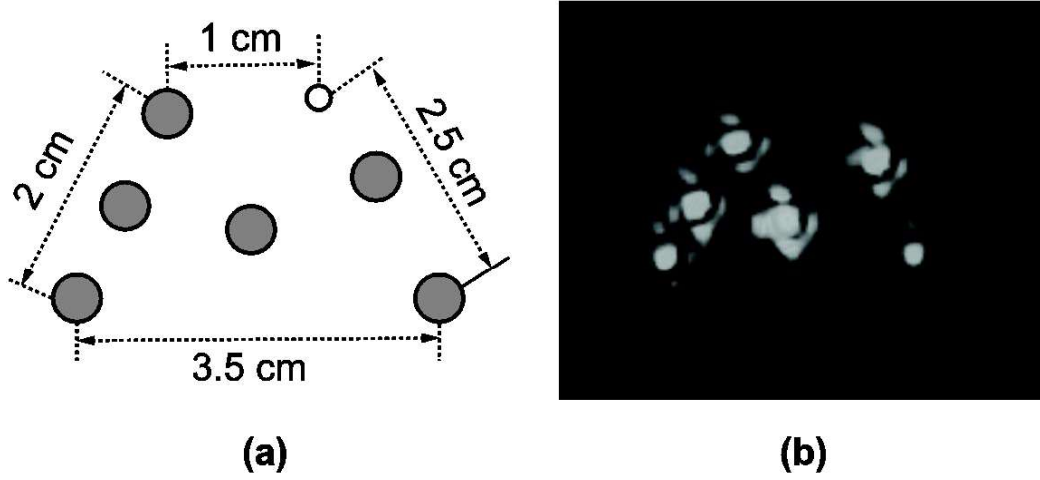


Fig. 21 (a) The pattern of 7 point scatterers including 6 steel balls (gray circles) and 1 needle (the dotted circle); (b) volume-rendered 3-D image. Minor side-lobes appear around the original echo of each point scatterer, which are related to the layout of transducer elements.

Currently, the 3-D image reconstruction has been done offline and 169 transmit-receive events were used to generate one volume as shown in Fig. 21(b) [32]. In a future real-time implementation, this would correspond to a frame rate of 44.4 volumes per second for an imaging depth of 10 cm. When the daisy-chain mode for delay-pattern programming is enabled, the frame rate reduces to about 40 volumes per second. We have also noted that volumes can be reconstructed from at minimum 25 transmit-receive events, at the cost of slightly degraded image quality [32]. This results in a frame rate of 300 volumes per second in the fast imaging mode.

4.4.4. Conclusions

A front-end ASIC with an co-integrated 32×32 PZT matrix transducer has been design and implemented to enable next-generation miniature ultrasound probes for real-time 3-D transesophageal echocardiography. The transducer array is split into a transmit and a receive sub-array to facilitate the power and area optimization of the ASIC. To address the critical challenge of cable-count reduction, sub-array receive beamforming is realized in the ASIC with a highly-compact and power-efficient circuit-level implementation, which utilizes the mismatch-scrambling technique to optimize the dynamic range. A power- and area-efficient LNA architecture is proposed to further optimize the performance. Based on these techniques, the ASIC demonstrates state-of-the-art power and area efficiency, and has been successfully applied in 3-D imaging experiments.

Acknowledgment

This research is supported by the Dutch Technology Foundation STW, which is part of the Netherlands Organisation for Scientific Research (NWO), and which is partly funded by the Ministry of Economic Affairs.

References

- [1] I. S. Salgo, "Three-Dimensional Echocardiographic Technology," *Cardiol. Clin.*, vol. 25, pp. 231–239, May 2007.
- [2] T. V. Scohy, et al., "A new transesophageal probe for newborns," *Ultrasound in medicine & biology*, vol. 35, pp. 1686-1689, Oct. 2009.
- [3] R. S. C. Cobbold, *Foundations of Biomedical Ultrasound*. Oxford University Press, 2006.
- [4] M. A. P. Pertijs, et al., "Low-power receive electronics for a miniature real-time 3D ultrasound probe," in *IEEE International Workshop on Advances in Sensors and Interfaces (IWASI)*, Jun. 2015, pp. 235 - 238.
- [5] B. Savord and R. Solomon, "Fully Sampled Matrix Transducer for Real Time 3D Ultrasonic Imaging," in *Proc. IEEE Ultrasonics Symp.*, 2003, pp. 945-953.
- [6] A. Bhuyan, et al., "3D Volumetric Ultrasound Imaging with a 32'32 CMUT Array Integrated with Front-End ICs Using Flip-Chip Bonding Technology," in *Proc. IEEE Int. Solid-State Circuits Conf. Dig. Tech. Papers*, 2013, pp. 396-397.
- [7] Q. Liu, C. Chen, Z. Chang, C. Prins, and M. A. P. Pertijs, "A mixed-signal multiplexing system for cable-count reduction in ultrasound probes," in *IEEE International Ultrasonics Symposium (IUS)*, Oct. 2015, pp. 1 - 4.
- [8] T. M. Carpenter, et al., "Direct Digital Demultiplexing of Analog TDM Signals for Cable Reduction in Ultrasound Imaging Catheters," *IEEE Trans. Ultrason., Ferroelectr., Freq. Control*, vol. 63, pp. 1078 - 1085, 2016.
- [9] T. Christiansen, M. Rasmussen, J. Jensen, and E. Thomsen, "Row-column addressed 2-D CMUT arrays with integrated apodization," in *International Ultrasonics Symposium*, Sept. 2014, pp. 600 - 603.
- [10] K. Chen, H.-S. Lee, and C. G. Sodini, "A Column-Row-Parallel ASIC Architecture for 3-D Portable Medical Ultrasonic Imaging," *IEEE J. Solid-State Circuits*, vol. 51, pp. 738 - 751, March 2016.

Chapter 4

- [11] C. Chen, et al., "A Prototype PZT Matrix Transducer with Low-Power Integrated Receive ASIC for 3-D Transesophageal Echocardiography," *IEEE Trans. Ultrason., Ferroelectr., Freq. Control*, vol. 63, pp. 47 - 59, Jan. 2016.
- [12] U. S. Food and Drug Administration (FDA), "Guidance for Industry and FDA Staff—Information for Manufacturers Seeking Marketing Clearance of Diagnostic Ultrasound Systems and Transducers," Sept. 2008.
- [13] A. Bhuyan, et al., "Integrated Circuits for Volumetric Ultrasound Imaging With 2-D CMUT Arrays," *IEEE Trans. Biomed. Circuits Syst.*, vol. 7, pp. 796-804, Dec. 2013.
- [14] M. Sautto, et al., "A CMUT transceiver front-end with 100-V TX driver and 1-mW low-noise capacitive feedback RX amplifier in BCD-SOI technology," in *Proc. ESSCIRC*, 2014, pp. 407-410.
- [15] I. O. Wygant, et al., "Integration of 2D CMUT arrays with front-end electronics for volumetric ultrasound imaging," *IEEE Trans. Ultrason., Ferroelectr., Freq. Control*, vol. 55, pp. 327-342, Feb. 2008.
- [16] C. Chen, et al., "A Front-end ASIC with Receive Sub-Array Beamforming Integrated with a 32 x 32 PZT Matrix Transducer for 3-D Transesophageal Echocardiography," in *Symposia on VLSI circuits*, 2016.
- [17] Z. Yu, et al., "Front-end receiver electronics for a matrix transducer for 3D transesophageal echocardiography," *IEEE Trans. Ultrason., Ferroelectr., Freq. Control*, vol. 59, pp. 1500-1512, Jul. 2012.
- [18] C. Chen, Z. Chen, Z. Chang, and M. A. P. Pertijs, "A compact 0.135-mW/channel LNA array for piezoelectric ultrasound transducers," in *European Solid-State Circuits Conference (ESSCIRC)*, 2015, pp. 404 - 407.
- [19] S. B. Raghunathan, et al., "Design of a miniature ultrasound probe for 3D transesophageal echocardiography," in *Proc. IEEE Ultrasonics Symp.*, 2014, pp. 2091-2094.
- [20] S. Blaak, et al., "Design of a Micro-beamformer for a 2D Piezoelectric Ultrasound Transducer," in *Proc. IEEE Ultrasonics Symp.*, 2009, pp. 1338-1341.
- [21] I. O. Wygant, "A comparison of CMUTs and piezoelectric transducer elements for 2D medical imaging based on conventional simulation models," in *International Ultrasonics Symposium*, 2011, pp. 100 - 103.
- [22] S. Robert, O. Abed-Meraim, and L. L. Coco, "Wide-band variable-gain LNA in 65nm

- CMOS with inverter based amplifier for multi-tuners cable TV reception," in European Solid-State Circuits Conference (ESSCIRC), 2009, pp. 104 - 107.
- [23] M. S. Akter, R. Sehgal, F. v. d. Goes, and K. Bult, "A 66 dB SNDR pipelined split-ADC using class-AB residue amplifier with analog gain correction," in European Solid-State Circuits Conference (ESSCIRC), 2015, pp. 315 - 318.
- [24] Y. Chae and G. Han, "Low Voltage, Low Power, Inverter-Based Switched-Capacitor Delta-Sigma Modulator," IEEE J. Solid-State Circuits, vol. 44, pp. 458 - 472, Feb. 2009.
- [25] T. Christen, "A 15-bit 140- μ W Scalable-Bandwidth Inverter-Based $\Delta\Sigma$ Modulator for a MEMS Microphone With Digital Output," IEEE J. Solid-State Circuits, vol. 48, pp. 1605 - 1614, July 2013.
- [26] J.-Y. Urn, et al., "A single-chip time-interleaved 32-channel analog beamformer for ultrasound medical imaging," in Proc. Asian Solid State Circuits Conference (A-SSCC), Nov. 2012, pp. 193 - 196.
- [27] J.-Y. Urn, et al., "An analog-digital-hybrid single-chip RX beamformer with non-uniform sampling for 2D-CMUT ultrasound imaging to achieve wide dynamic range of delay and small chip area," in Proc. IEEE Int. Solid-State Circuits Conf. Dig. Tech. Pap., Feb. 2014, pp. 426 - 427.
- [28] J.-P. Hong, et al., "A 0.004mm² 250 μ W $\Delta\Sigma$ TDC with time-difference accumulator and a 0.012mm² 2.5mW bang-bang digital PLL using PRNG for low-power SoC applications," in Proc. IEEE Int. Solid-State Circuits Conf. Dig. Tech. Pap., Feb. 2012, pp. 240 - 242.
- [29] R. F. Yazicioglu, P. Merken, R. Puer, and C. V. Hoof, "A 60 μ W 60 nV/ $\sqrt{\text{Hz}}$ Readout Front-End for Portable Biopotential Acquisition Systems," IEEE J. Solid-State Circuits, vol. 42, pp. 1100 - 1110, May 2007.
- [30] A. J. Lopez-Martin, J. Ramirez-Angulo, R. G. Carvajal, and L. Acosta, "Power-efficient class AB CMOS buffer," Electron.Lett., vol. 45, pp. 89-90, Jan. 2009.
- [31] K. Chen, H.-S. Lee, A. P. Chandrakasan, and C. G. Sodini, "Ultrasonic Imaging Transceiver Design for CMUT: A Three-Level 30-V_{pp} Pulse-Shaping Pulser With Improved Efficiency and a Noise-Optimized Receiver," IEEE J. Solid-State Circuits, vol. 48, pp. 2734 - 2745, Oct. 2013.
- [32] D. Bera, et al., "Three-Dimensional Beamforming Combining Micro-beamformed RF Datasets," in IEEE Ultrasonics Symposium, 2016, pp. 1-4.

Chapter 6

Multiline 3D beamforming using micro-beamformed datasets for pediatric transesophageal echocardiography

D. Bera, S. B. Raghunathan, C. Chen, Z. Chen, M.A.P. Pertijs, M.D. Verweij, V. Daeichin, H.J. Vos, A.F.W. van der Steen, N. de Jong, J.G. Bosch, "Multiline 3D beamforming using micro-beamformed datasets for pediatric transesophageal echocardiography," Phys. Med. Biol, vol. 63, no. 7, pp. 075015, 2018.

Chapter 6

Until now, no matrix transducer has been realized for 3D transesophageal echocardiography (TEE) in pediatric patients. In 3D TEE with a matrix transducer, the biggest challenges are to connect a large number of elements to a standard ultrasound system, and to achieve a high volume rate (>200 Hz). To address these issues, we have recently developed a prototype miniaturized matrix transducer for pediatric patients with micro-beamforming and a small central transmitter. In this paper we propose two multiline parallel 3D beamforming techniques (μ BF25 and μ BF169) using the micro-beamformed datasets from 25 and 169 transmit events to achieve volume rates of 300 Hz and 44 Hz, respectively. Both the realizations use angle-weighted combination of the neighboring overlapping sub-volumes to avoid artifacts due to sharp intensity changes introduced by parallel beamforming. In simulation, the image quality in terms of the width of the Point spread function (PSF), lateral shift invariance and mean clutter level for volumes produced by μ BF25 and μ BF169 are similar to the idealized beamforming using a conventional single-line acquisition with a fully-sampled matrix transducer (FS4k, 4225 transmit events). For completeness, we also investigated a 9 transmit-scheme (3×3) that allows even higher frame rates but found worse B-mode image quality with our probe. The simulations were experimentally verified by acquiring the μ BF datasets from the prototype using a Verasonics V1 research ultrasound system. For both μ BF169 and μ BF25, the experimental PSFs were similar to the simulated PSFs, but in the experimental PSFs, the clutter level was ~ 10 dB higher. Results indicate that the proposed multiline 3D beamforming techniques with the prototype matrix transducer are promising candidates for real-time pediatric 3D TEE.

6.1. Introduction

6.1.1. Pediatric Transesophageal Echocardiography

Transesophageal Echocardiography (TEE) allows imaging of the heart from the esophagus, avoiding artifacts due to the lungs and the rib cage. A few years ago, a MicroMulti TEE (μ TEE) [1] probe was introduced primarily for neonatal and pediatric applications [2]. The μ TEE probe has shown to be successful in imaging infant patients with weights as low as 1.7 kg without any major difficulties [1], [2]. Additionally, due to its small size, the μ TEE probe is very useful for monitoring adults undergoing catheter ablation for atrial fibrillation and atrial septal defects, without sedation [3], [4]. This probe can also be used for diagnosing hemodynamically unstable patients in intensive care units [5]. Even though the μ TEE probe is very useful for real-time 2D imaging, it is incapable of performing real-time 3D imaging of the heart.

Recently, real-time three dimensional TEE (3D TEE) has become an indispensable diagnostic modality to examine the complex 3D cardiac anatomy and function [6], [7]. In addition to that, 3D TEE helps to guide and monitor surgical and catheter-based interventions [8], [9]. At present, for 3D TEE in adults, a number of matrix TEE probes (Philips X7-2t [10], Siemens V5M TEE [11], GE 6VT-D [12]) are commercially available. These matrix TEE probes are suitable for real-time acquisition and live 3D display in adults. However, they are much larger in size than a μ TEE probe and therefore cannot be used in pediatric patients. Also, without full anesthesia, the 3D TEE probes are not suitable for long-term monitoring in adults, due to patient discomfort. Additionally, pediatric patients in general have higher heart rates than adults, and to accurately image the moving cardiac structures, a higher volume rate is required. Although a volume rate >40 Hz is already sufficient for B-mode imaging, for advanced applications such as 3D particle image velocimetry or speckle tracking higher volume rates (~ 200 Hz) are required. Moreover, to measure electromechanical wave propagation through the Purkinje fibers and myocardium and the resulting transient motion of the heart wall, a frame rate higher than 200 Hz is mandatory [13], [14]. Hence, if a matrix TEE probe with similar dimensions as the μ TEE probe with the capability of high frame rate volume imaging would be available, it could be used both as a pediatric probe as well as an adult probe for long-term monitoring.

6.1.2. Challenges in real-time 3D imaging

There are two major challenges in real-time 3D ultrasound imaging using a matrix transducer. The first challenge is to achieve a sufficiently high frame rate. The second challenge is the enormous number of transducer elements and the limited number of transmit/receive channels to connect these with the ultrasound system. Both challenges are interrelated.

The first challenge has generally been addressed from the early days of 3D imaging [15], [16] through parallel beamforming. In classical ultrasound, one image line is constructed from one transmit, along a narrow transmit beam. In volumetric imaging, where thousands of lines are

Chapter 6

needed for one volume, this is prohibitive. The attainable frame rate can be increased considerably by using wide (either plane or diverging) transmit beams and reconstructing multiple receive scanlines in parallel from each transmission [17]–[21].

To address the second challenge, sparse arrays, multiplexing and micro-beamforming (or sub-array beamforming) have been proposed. Sparse arrays [22] are known to produce poor image quality, and multiplexing is in direct conflict with the first challenge. 3D imaging with micro-beamforming [23], [24] can result in good images while reducing the receive channel count considerably. The principle of micro-beamforming is to subdivide the array into groups of N neighboring elements and to achieve pre-steering by applying micro-delays to the element signals before summing them, thus producing a single partially beamformed or micro-beamformed RF signal (μ BRF) per group. This step is typically performed within a front-end ASIC, and reduction in channel count by a factor N is thereby achieved. An external ultrasound scanner then receives the micro-beamformed RF signals from all sub-arrays and performs a delay-and-sum (DAS) beamforming to achieve full dynamic receive focusing (DRF).

Recently, a high frame rate 3D imaging scheme using diverging transmit waves with a GE 6VT-D TEE probe comprising of micro-beamforming capabilities has been proposed in [25]. In that work, it was shown that with only 9 diverging transmit waves (3×3 in lateral and elevation directions) and receive pre-steering co-aligned with the transmit beam directions, a volume with $70^\circ \times 70^\circ$ sector can be produced at volume rates of ~ 600 Hz with an image quality suitable for Tissue Doppler Imaging, but not for the best B-mode images. In this paper we will also investigate the suitability of such an imaging scheme with 3×3 beams for a prototype matrix transducer described below.

6.1.3. Parallel beamforming

Parallel beamforming was first proposed in [15] to achieve high frame rate volumetric imaging. Although the parallel beamforming technique enables imaging at high frame rate, it produces images with compromised image quality. In parallel beamforming, the scanlines from one transmission show higher correlation among themselves than with scanlines from neighboring transmissions. This results in an imaging artifact: sharp intensity changes at the transition between the scanlines from different transmissions. We refer to these artifacts as crossover artifacts. Several approaches have been proposed [17]–[19] to overcome the latter two limitations of parallel beamforming for 2D imaging using both linear array and phased array transducers. It has been shown that these crossover artifacts can be avoided by synthesizing transmit beams through interpolation of the unfocused received signals prior to the beamforming [17]. For a phased array, spatial compounding of the beamformed scanlines from multiple transmissions has been proposed to suppress these artifacts [19]. Thus, it is possible to avoid the crossover artifacts by combining the beamformed scanlines from neighboring transmissions.

6.1.4. Prototype miniaturized matrix TEE transducer

We have recently designed and realized a matrix TEE transducer [26] with small dimensions suitable for pediatric 3D TEE and/or for long-term monitoring in adults. This design has the capability of parallel beamforming for high frame rate 3D imaging. It features a receive aperture similar to the 2D μ TEE ($5 \times 5 \text{ mm}^2$), and a very small central transmit aperture, capable of generating broad transmit beams suitable for parallel beamforming. It is equipped with an ASIC for micro-beamforming to reduce the receive channel count and achieve a pre-steering capability.

None of the previously proposed parallel beamforming approaches is directly suitable for this prototype matrix transducer, given its transmitter-receiver layout and pre-steering capability. Therefore, the aim of this paper is the design and assessment of a suitable parallel beamforming scheme that can achieve good image quality and sufficiently high volume rate ($>200 \text{ Hz}$) with this type of transducer.

6.1.5. Proposed 3D beamforming schemes

The prototype transducer has a small transmit aperture, therefore it can suitably generate wide transmit beams. The wide transmit beams help in achieving high frame rate imaging using parallel beamforming but lead to reduced image quality. Furthermore, the receive pre-steering is limited to only 25 fixed directions in 3D space. In practice, this means that for each acquisition we have to choose the direction of pre-steering from the 25 directions and transmit a wide beam in an appropriate direction. We call this a transmit-receive event (tx-rx event). Hence, to achieve good-quality 3D images at a high frame rate, we need to find a 3D beamforming scheme that requires a minimal number of tx-rx events and also minimizes the image artifacts. In this paper, we investigated four parallel-beamforming schemes utilizing the high frame rate capabilities of the prototype transducer, and compare their performance in terms of image quality and frame rate. The first scheme requires 25 tx-rx events per volume, the second one 169 tx-rx events, and the third and the fourth scheme require only 9 tx-rx events per volume. To suppress sharp intensity changes in the proposed scheme, the scanlines for the final volume are produced by linearly combining the scanlines of the sub-volumes from neighboring tx-rx events. We refer to this scheme as sub-volume crossfading. As a result, all the beamforming schemes avoid the imaging artifacts due to the sharp intensity changes while switching from one transmission to the other. All of the proposed schemes can produce volume images at a high frame rate ($>40 \text{ Hz}$) by utilizing the broad transmissions and the limited number of pre-steering directions. We compare the image quality and frame rate of the proposed beamforming schemes with an ideal but slow 3D beamforming technique (4225 scanlines; one tx-rx event per scanline). The ideal 3D beamforming is performed in simulation using a hypothetical fully sampled (FS) matrix transducer of the same size and transmitter-receiver layout as the prototype transducer.

Chapter 6

6.1.6. Structure of the paper

A detailed description of the prototype matrix transducer, the two proposed 3D beamforming techniques and the idealized 3D beamforming technique are presented in Section 6.2. Section 6.2 also describes the setup of numerical simulations and experimental validation with an ultrasound research scanner. Section 6.3 compares the image quality of the 3D beamforming schemes in simulations and experiments. The paper ends with a discussion of the results of the beamforming schemes as well as future work regarding real-time 3D TEE using the prototype matrix transducer.

6.2. Materials and Methods

6.2.1. Description of the prototype matrix transducer

We have recently designed and realized a prototype miniaturized matrix TEE transducer [26] with dimensions similar to a 2D μ TEE probe: a $5 \times 5 \text{ mm}^2$ aperture consisting of 32×32 individual PZT elements. The element pitch is $150 \text{ }\mu\text{m}$ and the center frequency is 5 MHz. The transducer array is constructed by dicing a bulk piezo-electrical material (3203HD, CTS Corporation, Albuquerque, MN, USA) with a dicing kerf width of $20 \text{ }\mu\text{m}$. The PZT stack is mounted directly on top of a front-end ASIC using the PZT-on-CMOS integration scheme described in [27]. For simplification of the electronics design, the transmit and receive elements are completely separated electrically.

Figure 1 shows the layout of transmit and receive elements. The transducer has a very small transmit aperture area ($1.2 \times 1.2 \text{ mm}^2$), consisting of 8×8 elements at the center. These transmit elements are wired out directly to an ultrasound scanner. The transmit array is capable of steering to any direction in 3D space, but due to the small aperture size, the natural focus is shallow. Hence, the array cannot focus at a relevant depth; it produces wide transmit beams suitable for parallel beamforming, selectively steered in 3D space. The 864 receive elements are connected directly to the front-end ASIC for micro-beamforming [26]. The receive elements are divided into 96 sub-arrays of 3×3 elements. The signals from each element of a sub-array are delayed with analog delays and summed by a micro-beamformer in the front-end ASIC. The micro-beamformers reduce the number of cables by a factor of 9. Thus, the 864 receive elements of the prototype are funneled into 96 sub-arrays, and their signals are fed to the receive channels of an external ultrasound scanner. In this paper, the output signals of all sub-arrays for one tx-rx event are referred to as a μ BRF dataset. The analog delays for elements in a sub-array can be programmed from 30 ns up to 180 ns in steps of 30 ns. These analog delays can steer an individual sub-array to angles of 0° , $\pm 17^\circ$, and $\pm 37^\circ$ in both lateral and elevation directions. Thus, by using the micro-beamforming, the receiver can be pre-steered to 25 fixed directions in the 3D space.

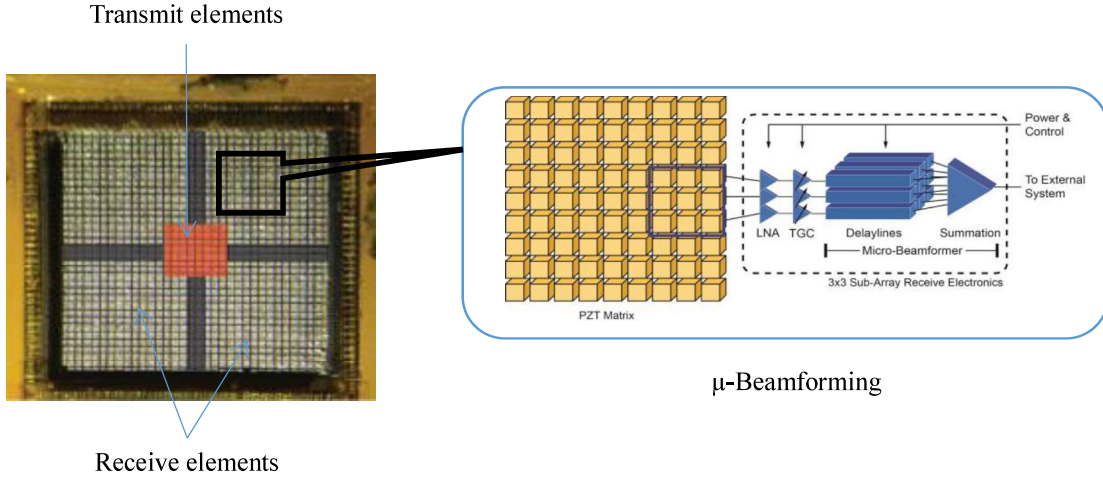


Figure 1: Layout of the custom designed pediatric 3D TEE transducer [26]

6.2.2. Parallel beamforming with pre-steering

The 3D parallel beamforming schemes are performed in three steps. In the first step, the receive sub-arrays are pre-steered to one of the 25 fixed directions. A diverging transmit beam is steered to the same direction or to an adjacent direction, and the 96-channel μ BRF dataset is acquired. In the second step, DAS beamforming is applied to the μ BRF dataset to produce a sub-volume of 3D beamformed scanlines. To cover a desired volume, these two steps are repeated several times to generate overlapping 3D sub-volumes, each from a different tx-rx event. In the third step, each scanline in the final volume is produced by selecting and/or combining scanlines from the sub-volumes reconstructed using the μ BRF datasets of the neighboring tx-rx events.

The pre-steered received beams from a single sub-array of the prototype have an opening angle of $\sim 50^\circ$. Although it is possible to reconstruct a full volume using only one acquired μ BRF dataset, the image intensity will be the best in the proximity of the pre-steering direction. Additionally, such a single-event μ BRF contains grating lobes due to large pitch (1.5λ) between sub-arrays. Hence, to minimize the amplitude variation in the final volume and to suppress grating lobes, transmissions are steered to the angles close to the pre-steering directions. A single sub-volume consisting of only a pre-defined set of scanlines is produced using a μ BRF dataset received from a single tx-rx event. Figure 2 shows an example of parallel beamforming along with receive pre-steering. In this figure, the regions correspond to the 25 receive pre-steering directions. Figure 2(a) depicts one tx-rx event and its beamformed scanlines. In this example, the receive sub-arrays are pre-steered to an angle $(\theta, \varphi) = (0^\circ, 17^\circ)$, where θ is the angle in lateral direction (X), and φ is the angle in elevation direction (Y).

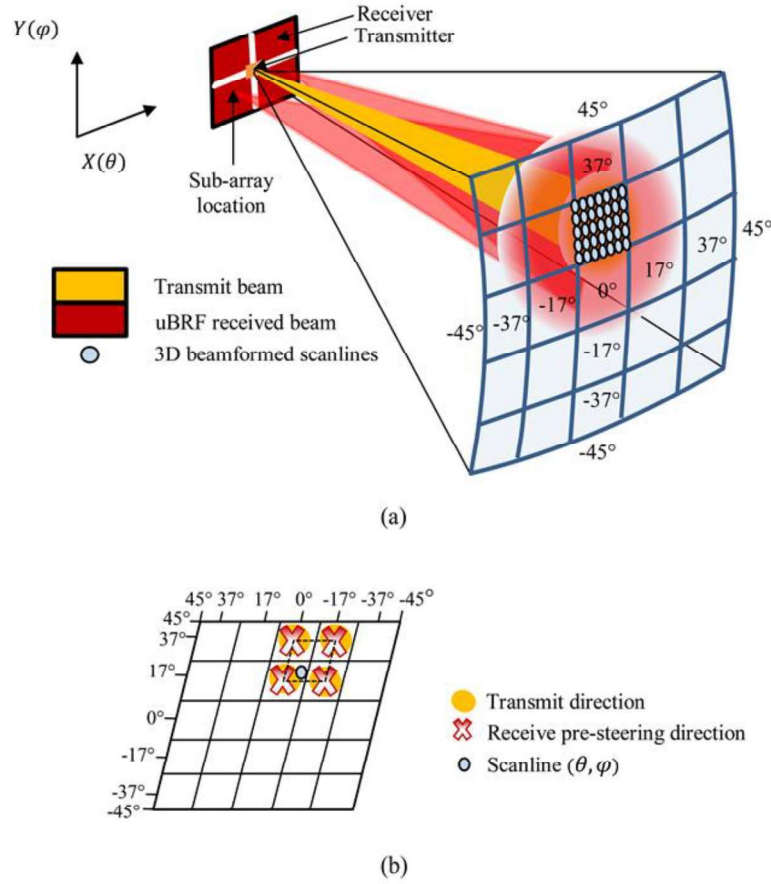


Figure 2: (a) Diverging transmit beam, μ BFRF received beam, 3D beamformed scanlines and 25 pre-steering regions lying on a spherical surface. (b) Illustration of μ BF25: Diverging transmit beams steered to angles aligned with the pre-steering angles. Scanlines of the intermediate angles/regions are reconstructed using neighboring tx-rx events. All the scanlines within the dotted rectangle are built by a linear combination from the same four tx-rx events ($-17^\circ \leq \theta \leq 0^\circ; 17^\circ \leq \varphi \leq 37^\circ$)

A diverging transmit beam is then steered to the same angle $(\theta, \varphi) = (0^\circ, 17^\circ)$. After that, the μ BFRF dataset of this tx-rx event is used to reconstruct the RF scanlines of the region, as highlighted in Figure 2(a). To reconstruct a volume covering $\pm 45^\circ$, both in lateral and elevation directions, the scanlines for all the 25 regions are reconstructed. This switching from one tx-rx event to the other for reconstructing individual regions leads to image artifacts in the form of sharp intensity changes and speckle discontinuities at the region borders, which was not covered in earlier methods of parallel beamforming in presence of micro-beamforming [25].

6.2.3. Proposed parallel beamforming with 25 tx-rx events (μ BF25)

To minimize the image artifacts due to μ BFRF switching, we combined the scanlines produced from the μ BFRF dataset of the neighboring directions, as shown in Figure 2(b). Hence, each scanline at an angle (θ, φ) in the final volume V_f was produced as a weighted sum of the

scanlines for that angle from the sub-volumes of adjacent tx-rx events:

$$V_f(\theta, \varphi) = \{\sum_m w(\theta - \theta_m, \varphi - \varphi_m) \cdot V_m(\theta, \varphi) : |\theta - \theta_m| \leq \delta, |\varphi - \varphi_m| \leq \delta\} \quad (1)$$

with $\sum_m w(\theta - \theta_m, \varphi - \varphi_m) = 1, m \in M$ and $M \subset [1, 25]$,

where $V_m(\theta, \varphi)$ is the scanline corresponding to the m^{th} tx-rx event steered to (θ_m, φ_m) . The weight w is constructed using coefficients from a Hanning window and assigned to the scanline at (θ, φ) based on its proximity to the direction (θ_m, φ_m) . δ is chosen such that for each scanline in V_f , M contains a set of maximum four neighboring tx-rx events from the available 25 tx-rx events. Thus, the $\mu\text{BF}25$ technique performs a weighted sum of corresponding scanlines from the adjacent tx-rx events to produce a volume with minimized image artifacts. Figure (b) illustrates how all the scanlines within the dotted rectangle are built as a linear combination from the same four tx-rx events.

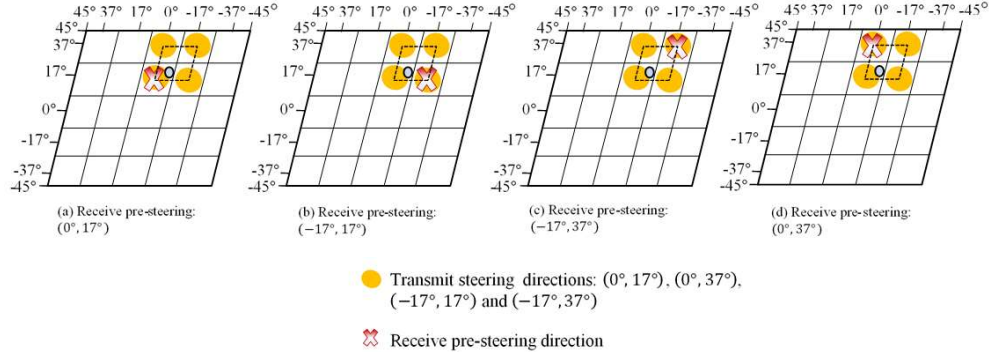


Figure 3: Illustration of $\mu\text{BF}169$: Diverging transmit beams steered to a pre-steering direction and to three neighboring directions while using the same receive pre-steering. Scanlines of the intermediate angles/regions are reconstructed using all 16 neighboring tx-rx events

6.2.4. Proposed parallel beamforming with 169 tx-rx events ($\mu\text{BF}169$)

As mentioned, the pre-steered receive beams from a single sub-array have an opening angle of $\sim 53^\circ$, and the transmit beam had an opening angle of $\sim 17^\circ$ (at -3 dB level). Hence, a pre-steered receive beam overlaps not only with the transmission to its own pre-steering direction but also with the transmissions to the neighboring directions. These overlaps between the pre-steering receive beam and the neighboring transmissions imply that those tx-rx events contain relevant information of scatterers within that zone. To exploit that additional information, we propose an alternative 3D beamforming technique with 169 tx-rx events to achieve improved image quality. Accordingly, each scanline at an angle (θ, φ) in the final volume V_f was produced using scanlines from all the adjacent tx-rx events, as shown in Figure 3, using

$$V_f(\theta, \varphi) = \left\{ \sum_m w(\Delta\theta_m^t, \Delta\varphi_m^t, \Delta\theta_m^r, \Delta\varphi_m^r) \cdot V_m(\theta, \varphi) : |\Delta\theta_m^t|, |\Delta\theta_m^r| \leq \delta \right. \\ \left. \text{and } |\Delta\varphi_m^t|, |\Delta\varphi_m^r| \leq \delta \right\} \quad (2)$$

with $\Delta\theta_m^t = \theta - \theta_m^t$, $\Delta\varphi_m^t = \varphi - \varphi_m^t$, $\Delta\theta_m^r = \theta - \theta_m^r$ and $\Delta\varphi_m^r = \varphi - \varphi_m^r$

$$\text{and } \sum_m w(\Delta\theta_m^t, \Delta\varphi_m^t, \Delta\theta_m^r, \Delta\varphi_m^r) = 1, m \in N \text{ and } N \subset [1, 169]$$

where $V_m(\theta, \varphi)$ is the scanline corresponding to the m^{th} tx-rx event. For the m^{th} tx-rx event, the angle of transmission $(\theta_m^t, \varphi_m^t)$ and the angle of receive pre-steering $(\theta_m^r, \varphi_m^r)$, together determine δ , i.e. the size of the region of reconstruction. For a scanline at (θ, φ) , the weight w is determined based on the deviation from $(\theta_m^t, \varphi_m^t)$ and $(\theta_m^r, \varphi_m^r)$. For each scanline, N contains a set of 16 neighboring tx-rx events from the total 169 tx-rx events.

6.2.5. Proposed parallel beamforming with 9 tx-rx events (μBF9)

To achieve higher frame rate than μBF25 , we explored possible parallel beamforming using less than 25 tx-rx events. Because of the wide opening angle of the transmit beams and the receive beams from the sub-arrays, it is possible to cover an entire volume (of $90^\circ \times 90^\circ$ viewing angle) with only 9 tx-rx events and achieve a volume rate even higher than μBF25 . For volume reconstruction with 9 tx-rx events, considering the transmit direction to be the same as pre-steering direction, we chose the transmit steering and receive pre-steering angles to the central direction and either to $\pm 17^\circ$ or $\pm 37^\circ$ in both lateral and elevation directions. Both in the proposed μBF9 with $\pm 17^\circ$ (μBF9n) and μBF9 with $\pm 37^\circ$ (μBF9w), to produce the final volume, angle weighted linear combination similar to μBF25 was applied to avoid the image artifacts.

6.2.6. Ideal DAS with fully-sampled matrix transducer (FS4k)

To compare the performance of the proposed beamforming techniques with an ideal DAS 3D beamforming, an idealized FS matrix transducer was simulated with all settings similar to the prototype transducer, such as the pitch, center frequency and the number and configuration of transmit and receive elements (Table 1). All transmit and receive elements in the FS transducer, however, were individually addressable (no micro-beamforming, all elements wired out). To achieve the best image quality with the given transmit and receive aperture, for each scanline in the volume one tx-rx event was used, where both transmit and receive were steered in the exact direction of the scanline, with the narrowest possible transmit beam. For such a small receive aperture size ($5 \times 5 \text{ mm}^2$, with natural focus at 20 mm), DRF will not make any difference in the image quality beyond 20 mm. Therefore, in receive, instead of DRF, we used fixed focusing at 40 mm depth. To reconstruct 65×65 scanlines, 4225 tx-rx events were needed. This ‘ideal’ beamforming was therefore named FS4k.

For all the 3D beamforming schemes, the final volume in Cartesian coordinates was produced by performing envelope detection, logarithmic compression and scan conversion on the volume in (r, θ, φ) domain (where r represents depth). The performance of the beamforming schemes

was then compared for image quality.

For an imaging depth of 10 cm (and thus a PRF of 7.5 kHz) and scan angle of $\pm 45^\circ$ in lateral and elevation directions, FS4k will yield a volume rate of 1.78 Hz. For the same imaging depth, μ BF25 can achieve a volume rate of 300 Hz. Both μ BF9 methods can achieve a volume rate of 833.4 Hz, which is even higher than μ BF25. The proposed μ BF169 requires about 7 times more transmissions than μ BF25 and thus can achieve a volume rate of 44.4 Hz.

6.2.7. Simulation and experimental setup

The proposed 3D beamforming schemes were examined using simulations in FieldII [28] and verified by post-processing of μ BRF datasets, acquired from the prototype transducer with a commercial research ultrasound system. The simulations were performed with a model of our prototype matrix transducer using similar properties [26]. The image quality was determined based on the following criteria: clutter levels, uniformity of intensity distribution and width of point spread function (PSF) in lateral and elevation directions.

6.2.7.1. Simulation setup

The FieldII simulations of the proposed techniques were carried out with the transducer parameters and imaging parameters as shown in Table 1. The impulse response of the transducer was modelled as a 2 cycle sinusoid. The transducer excitation was a 3 cycle sinusoid tone burst. The image quality was determined by simulating different sets of point scatterers located at several positions in 3D space. The widths of PSFs were determined by simulating five point scatterers on the C-plane at 20 mm depth as shown in Figure 4. One of the five scatterers was placed at the center, the others were placed at extreme positions (± 8.5 mm) in X and Y direction.

The clutter level and uniformity of intensity distribution were examined by placing a scatterer at 65 consecutive positions on a 20 mm C-plane, with its lateral position ranging between -16 mm and 16 mm. for each scatterer position, an entire volume was reconstructed to determine the clutter level and uniformity of the intensity distribution.

Table 1: Parameters of simulations

	Parameters	Value
Transducer	Center frequency	4.5 MHz
	Number of transmit elements	64
	Number of receive elements	864
	Pitch	150 μ m
	Number of receive sub-arrays	96
Simulation parameters	Receive sub-array pitch	450 μ m
	Pulse duration	0.6 μ s
	Apodization	Box-car
	Sampling frequency	100 MHz

Chapter 6

	Transmit focus	-1.2 mm
	Receive focus	40 mm
	Imaging depth	60 mm
	Transmit steering angles	0°, $\pm 17^\circ$ and $\pm 37^\circ$ in lateral and elevation and all 65×65 angles for FS4k
3D reconstruction	Number of scanlines	65×65
	Scan angle	$\pm 45^\circ$

6.2.7.2. Measures of image quality in simulation

A. Width of PSF

For all the methods, the lateral and elevation PSFs were exactly the same because of the symmetric layout of the transducer elements in both directions. Hence, for all the volumes produced in simulations, we report only the width of the PSFs in the lateral direction from the response of the point scatterers in the central position. In simulation, to estimate the performance of the proposed 3D beamforming techniques, the widths of PSFs in the lateral and elevation directions were computed at -6 dB and at -20 dB and compared with FS4k.

B. Shift invariance

For multiline reconstruction, uniformity of the intensity distribution over 3D space may be compromised (as shown by the imaging artifact mentioned in 6.2). In general, this is referred to as spatial shift variance or translation (in) variance: if the probe is moved with respect to the scatterers, the image should only translate, and not change in any other way. To estimate uniformity of the intensity distribution, we determined the normalized maximum intensity of the individual PSFs (corresponding to each of the 65 scatterer positions) with respect to the maximum intensity of the central scatterer position.

C. Clutter level

Clutter is an artifact in ultrasound images that appears as diffuse echoes superimposed on the received signals of interest. In our PSF measurement, we considered all echoes outside of the -20 dB edge of the main lobe as clutter. For each volume reconstruction technique, the mean clutter level was calculated by taking an average of the clutter level for each 65 volumes produced from the 65 positions of a single point scatterer between -20 mm to +20 mm in the lateral direction.

6.2.8. Experimental setup

To investigate the performance of the proposed 3D beamforming schemes, data were acquired by connecting the prototype matrix transducer [26] to a Verasonics V1 ultrasound system

(Verasonics Inc. Kirkland, Washington, USA). The experiment was done with seven point scatterers (six steel balls and one needle) in water, placed on a C-plane at a depth of 35 mm. For each tx-rx event, the delays corresponding to a pre-steering angle were loaded to the ASIC, using an external FPGA. A diverging transmit beam was then steered to the desired direction and the μ BRF dataset received by the sub-arrays was acquired. The diverging transmit beams were produced by placing the transmission focus behind the transducer at -1.2 mm, and the transducer excitation was a 3 cycle sinusoid tone burst. Appropriate transmit delays for focusing and steering were generated by the Verasonics and applied to the individual transmit elements of the prototype transducer. For each tx-rx event, the μ BRF dataset was acquired with fixed gain settings, at 18 MHz sampling rate and stored for post-processing. Before 3D beamforming, the μ BRF datasets were filtered with a band-pass filter of 100% bandwidth with 4.5 MHz center frequency.

6.3. Results

6.3.1. Simulation results

6.3.1.1. Volume reconstructed using a single tx-rx event

Image intensity of a full volume reconstructed using a single μ BRF dataset acquired for a specific tx-rx event will be the best in the proximity of the transmit and pre-steering direction. Figure 5 shows the 2D slices (located at 0° elevation angle) of the two simulated polar volume images reconstructed for the five point scatterers (shown in Figure 4) using μ BRF datasets acquired from two different tx-rx events. For both of the two tx-rx events, transmissions were steered to $(0^\circ, 0^\circ)$. However, the pre-steering directions for the two volume images were $(-37^\circ, 0^\circ)$ and $(0^\circ, 0^\circ)$. The images are shown in polar coordinates for easier interpretation of sidelobes and clutter. The point scatterer at -8.5 mm (at -23° in Figure 5) in the lateral direction is brighter in Figure 5(b) than in Figure 5(c). Furthermore, in Figure 5(b), the intensity of the central scatterer was highest compared to the other scatterers that were away from the center. Additionally, in Figure 5(b) the central scatterer appeared to be asymmetric, and the scatterer at $+23^\circ$ was completely obscured by the clutter from the scatterer at -23° . This clutter was caused by the grating lobes produced due to the pre-steering to $(-37^\circ, 0^\circ)$. Thus, Figure 5 shows that for a given tx-rx event only a defined 3D region close to the transmit and pre-steering direction has high intensity; all the other regions in the 3D space suffer from poor intensity and clutter. This uneven intensity distribution and clutter suggest that only the defined illuminated sub-volume (closer to the transmit and pre-steering direction) should be reconstructed from each tx-rx event; and thus, multiple tx-rx events should be used to reconstruct the final volume to achieve better image quality.

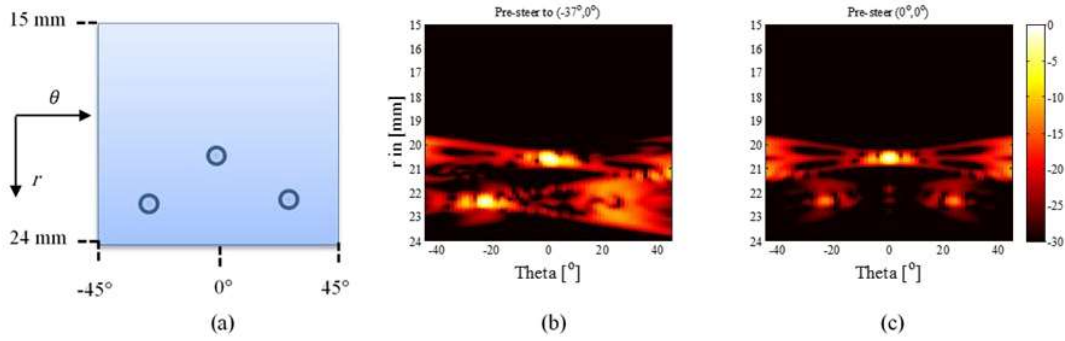


Figure 5: (a) Schematic of the position of the three point scatterers in polar space. 2D slices at 0° elevation angle of polar volumes reconstructed from two tx-rx events (b) pre-steered to $(-37^\circ, 0^\circ)$ and (c) pre-steered to $(0^\circ, 0^\circ)$

6.3.1.2. Volume reconstructed using simple parallel beamforming

For each tx-rx event, the quality of the volume image in terms of intensity is the best close to the pre-steering direction. Therefore, as described in Section 2.2, a complete volume ranging $\pm 45^\circ$ in both lateral and elevation directions was produced using 25 tx-rx events. Figure 6 shows polar volume images sliced into two 2D planes located at 0° lateral angle and at 0° elevation angle. The volumes were reconstructed with point scatterers located at the same positions as in Figure 5. These images contain sharp boundaries introduced by the transition from one tx-rx event to the other at 9° and 23° . The image artifacts caused by the sharp boundaries are indicated by arrows. Since these artifacts are not acceptable in clinical practice, we consider combining overlapped μBRF datasets in the following sections.

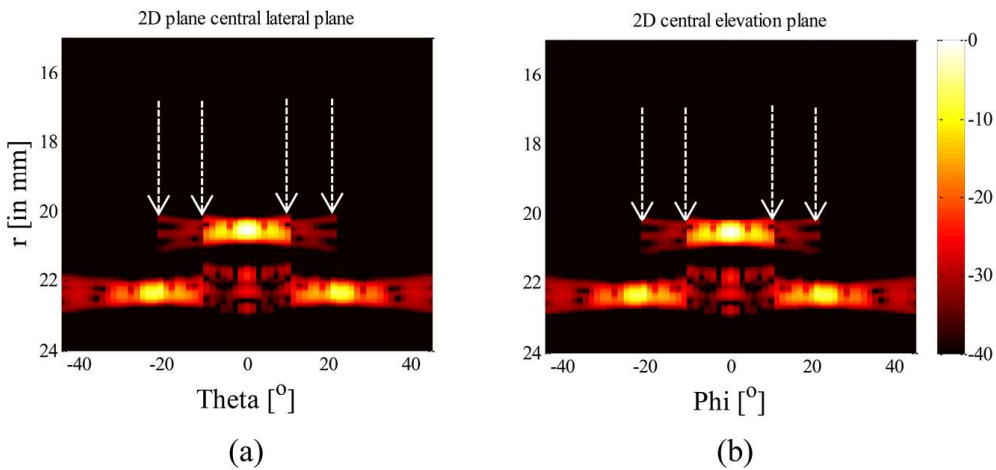


Figure 6: 2D polar images with simple parallel beamforming (hard boundaries). (a) Central lateral plane and (b) central elevation plane.

6.3.1.3. Comparison of width of PSF for μ BF25, μ BF169, μ BF9 and FS4k

Figure 7 shows 2D polar planes sliced from polar volume images at 0° elevation angle for μ BF25, μ BF169, μ BF9n, μ BF9w, and FS4k. Unlike the images produced using simple parallel beamforming (in Figure 6), in all the five images produced by μ BF25, μ BF169, two μ BF9 and FS4k, we do not see the crossover artifacts described before. However, μ BF9 with both $\pm 17^\circ$ and $\pm 37^\circ$ produce images degraded with off-axis energy. In Figure 7(c), for μ BF9n, off-axis energy for the central scatterer is visible at extreme angles.

In Figure 7(d), for μ BF9w, the scatterers at $\pm 23^\circ$ are less intense and degraded by off-axis energies. Hence, both the μ BF9 techniques produced images with inferior image quality compared to μ BF25 and μ BF169. For quantitative comparison between the PSFs of these 3D beamforming schemes, the angular intensity profile of the central point scatterer along the lateral direction at 20 mm depth and 0° elevation angle are plotted in Figure 8. It can be observed that the angular widths at -6 dB for all the five methods are almost the same ($\sim 4^\circ$). However, μ BF169 produced slightly lower (~ 2 dB) sidelobes and μ BF9w produced slightly higher sidelobes than all other beamforming methods. The lateral angular width of the PSF at -20 dB for μ BF9n [Figure 7(c)] is similar to μ BF25 [Figure 7(a)]. However, at wider angles, the PSF for μ BF9n shows the highest clutter level among all other beamforming. The lateral angular width of the PSF at -20 dB for μ BF25 is $\sim 2^\circ$ wider than both μ BF169 [Figure 7(b)] and FS4k [Figure 7(e)]. Thus, considering the widths of the PSFs μ BF169 performs better than all other proposed high frame rate beamforming methods.

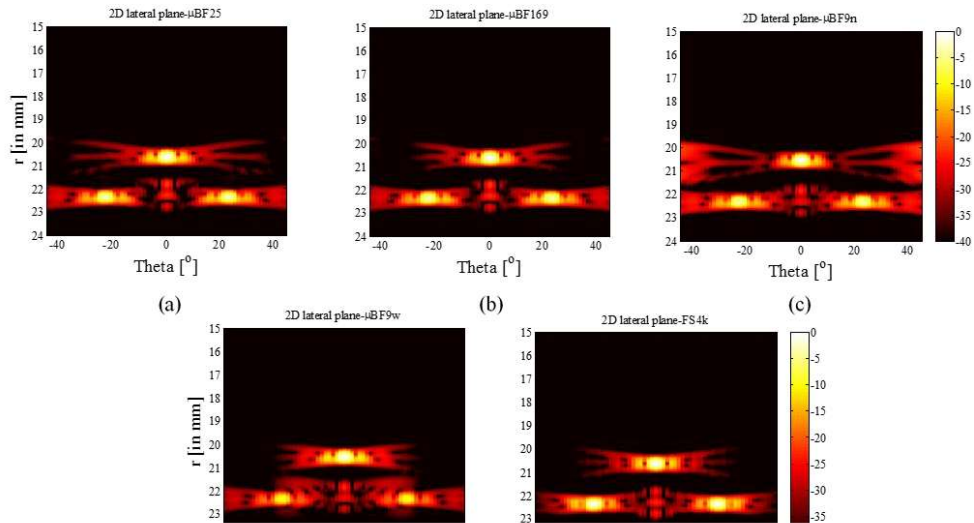


Figure 7: Polar images for 2D lateral plane of 3 point scatterers using (a) μ BF25, (b) μ BF169, (c) μ BF9n, (d) μ BF9w and (e) FS4k.

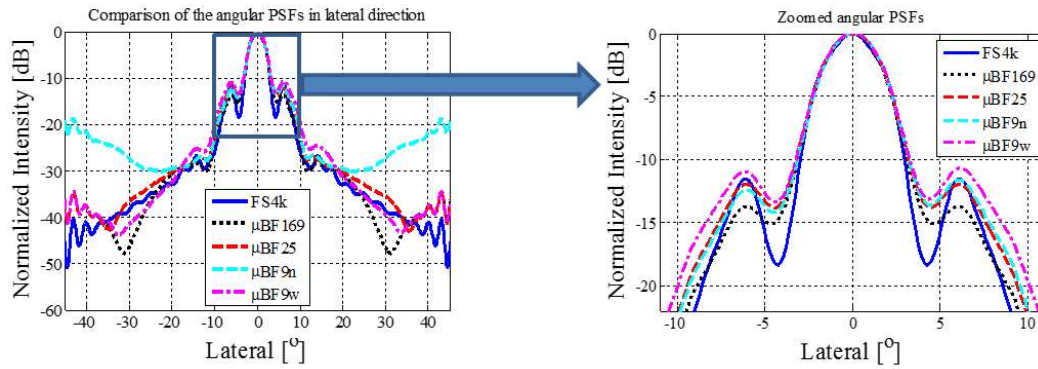


Figure 9: Simulated PSFs of μ BF25, μ BF169, μ BF9n, μ BF9w and FS4k

6.3.1.4. Shift invariance

Figure 9 shows the maximum intensity for the 65 point scatterer locations with respect to the maximum intensity of the central scatterer position located on the C-plane at 20 mm and simulated using μ BF25, μ BF169 and FS4k. For FS4k, the normalized maximum intensities of the scatterers were almost uniform (with a gradual decrease with increase in angle and minor variations). However, for both μ BF25 and μ BF169 sharp intensity drops were visible at four locations. A drop of ~ 4 dB was observed for the point scatterer located at $\pm 25^\circ$, and a drop of ~ 3 dB was observed for the point scatterer at $\pm 9^\circ$. In addition to that, a drop of ~ 7 dB was observed for the point scatterer at $\pm 45^\circ$. For both μ BF25 and μ BF169, the point scatterers at $\pm 17^\circ$ and $\pm 37^\circ$ on the fixed C-plane had similar intensities compared to FS4k. In terms of uniformity of intensity distribution, both μ BF25 and μ BF169 performed relatively poorer than FS4k. However, there were no significant differences observed between the performance of μ BF25 and μ BF169.

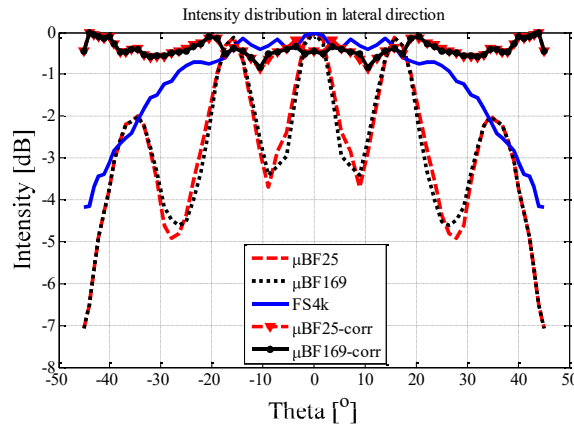


Figure 9: Uniformity of intensity distribution for 65 point scatterer positions along lateral direction.

Multiline 3D beamforming using micro-beamformed datasets

The intensity drops for μBF25 and μBF169 were present due to the fixed receive pre-steering and transmit directions causing lower sensitivity at the interposed angles. It is evident that the intensity drops for μBF9n and μBF9w were more severe, as the angular gap between consecutive tx-rx directions was even larger than μBF25 and μBF169 . For a clearer representation, we did not show those intensity profiles in Figure 9. To compensate for the intensity variation, both in μBF25 and μBF169 , the beamformed RF lines were weighted with the inverse of the intensity profiles. The weights for the polar volume data were computed using a linear interpolation on the weights for the 65 lateral positions. From Figure 9, it can be observed that after the compensation, the corrected intensity profiles for both μBF25 and μBF169 (intensity plots marked with triangles and circles) were uniform. The slight variation in the final normalized intensity levels could be due to a minor numerical imprecision while interpolating the weights for the polar volume data. Similar to μBF25 and μBF169 , the required intensity compensation was also applied to correct the intensity drops in μBF9n and μBF9w . In practice, this compensation will lower the signal to noise ratio (SNR) for the lines that needed a relatively large gain compensation.

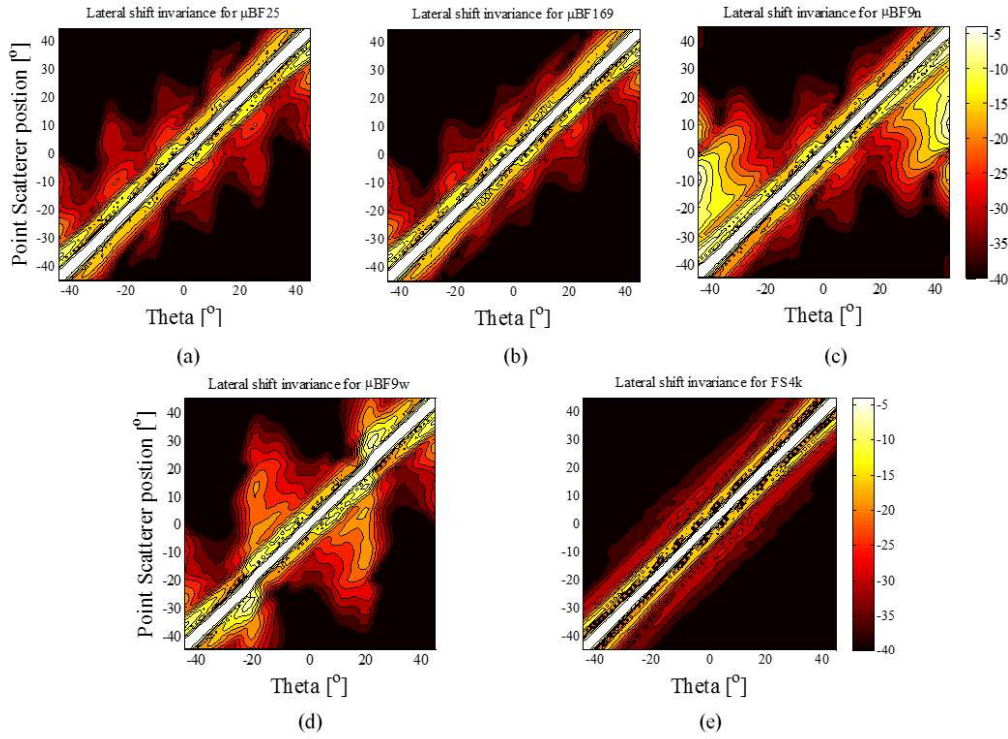


Figure 10: Contour plots of stacked PSFs for 65 lateral positions using (a) μBF25 , (b) μBF169 , (c) μBF9n , (d) μBF9w and (e) FS4k

For the analysis of the lateral shift invariance, Figure 10 shows five contour plots obtained after stacking the intensity compensated PSFs for 65 lateral positions using all the five beamforming schemes. In such a plot, a perfect lateral shift invariant beamforming technique should yield a uniform diagonal structure. These plots show that among the five techniques, as expected, FS4k

Chapter 6

[Figure 10(e)] is the best in terms of shift invariance and both μBF9n [Figure 10(c)] and μBF9w [Figure 10(d)] are worse. For both μBF9n and μBF9w , the point scatterers around the center (in between -20° and 20°) show larger shift variances. Both μBF25 [Figure 10(a)] and μBF169 [Figure 10(b)] had larger shift variances for the point scatterers at the interposed angles (at $\pm 9^\circ$ and $\pm 25^\circ$) due to the fixed receive pre-steering and transmit directions. However, μBF169 is slightly less lateral shift variant than μBF25 . Although intensity compensation yielded uniform maximum intensities at different positions, it increased the clutter levels at the interposed angles. However, as expected from the previous results (shown in Figure 8), all the three techniques were almost equally lateral shift invariant when considered until -20 dB.

6.3.1.5. Clutter levels

Figure 11 shows the mean clutter levels for the 65 point scatterers located on the C-plane at 20 mm and simulated using μBF25 , μBF169 and FS4k. From the figure, it can be observed that the profile of the mean clutter levels was quite uniform for FS4k. However, for both μBF25 and μBF169 , the profiles of the mean clutter levels had valleys at the pre-steering angles and peaks at the interposed angles ($\pm 9^\circ$, $\pm 25^\circ$). The mean clutter levels for μBF25 were ~ 2 dB higher than μBF169 . It can also be observed that the average of the mean clutter levels over different lateral positions for both μBF25 and μBF169 was ~ -77 dB. The average of the mean clutter levels for FS4k was ~ 2 dB lower than μBF25 , μBF169 . It is obvious from Figure 10 that the mean clutter level for the two μBF9 methods will be higher than others, therefore, we have not shown them in Figure 11.

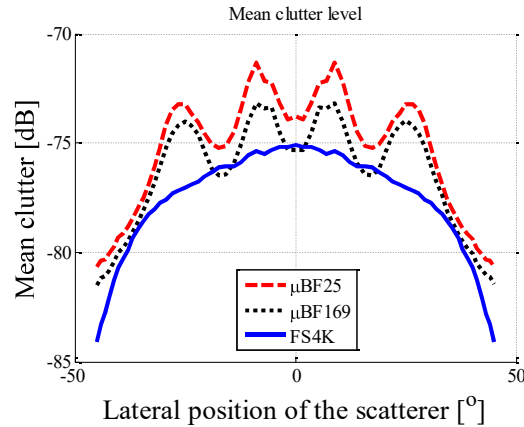


Figure 11: Mean clutter level for 65 scatterer positions along lateral direction.

6.3.2. Experimental results

6.3.2.1. Volume rendered image

Figure 12(a) and Figure 12(b) show the positions of the 7 point scatterers (six steel balls and one needle) of the phantom, Figure 12(c) and Figure 12(d) show the corresponding volume

rendered images using μ BF25 and μ BF169 of this phantom placed on a C-plane at 35 mm with 40 dB dynamic range. In both Figure 12(c) and (d), the positions of the point scatterers accurately matched with the actual positions of the scatterers. However, from Figure 12, it can be observed that the clutter level in volume rendered image using μ BF25 is slightly higher than the image using μ BF169 [indicated by arrows in Figure 12(c) and (d)]. The needle (scatterer 4) did not have a steel ball on the top, so in the rendered images it appeared with less intensity. In the rendered images, for each scatterer, one main lobe and four sidelobes (in both lateral and elevation directions) were observed. The skewed appearance of the sidelobes was caused by few non-working receive sub-arrays in the prototype transducer. We have observed the same pattern of the sidelobes in simulation with the absence of those non-working sub-arrays. Similar to the simulation results, in experimental results, μ BF25 produce volume images with similar appearance as μ BF169 but with somewhat higher clutter levels.

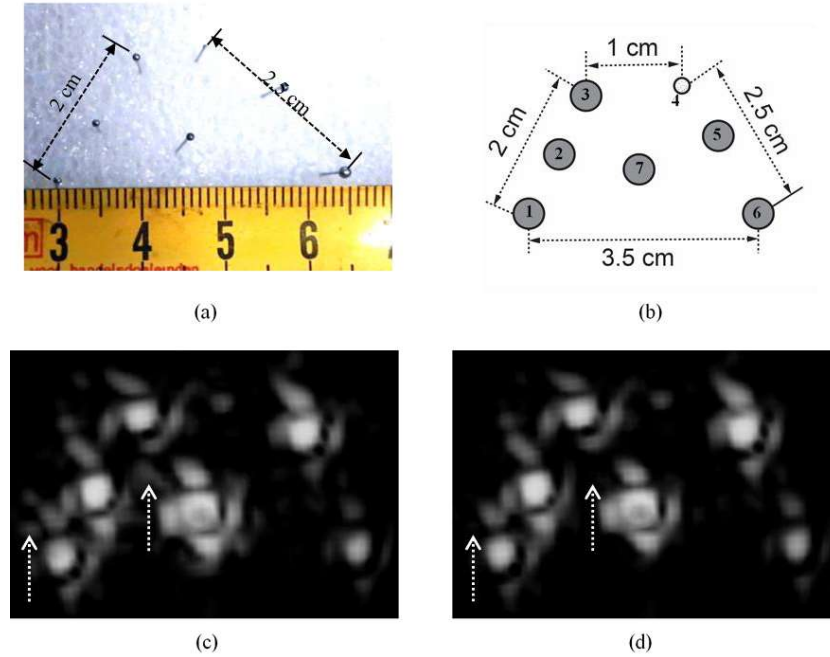


Figure 12: (a) The seven point scatterers used in the experiment, (b) the pattern of the 7 point scatterers including six steel balls (gray circles) and 1 needle (white circle), (c) volume rendered image using μ BF25 and (d) volume rendered image using μ BF169

6.3.2.2. Comparison between the widths of simulated and measured PSF

Figure 13(a) and Figure 13(b) show the PSFs in lateral and elevation directions for the central scatterer of μ BF25 and μ BF169 from the phantom measurement and the simulation of μ BF169. From these figures, it can be observed that the widths of the main lobe at -6 dB, in both lateral and elevation directions from the measurement are $\sim 4^\circ$, which are the same as the widths from the simulation (as shown in Figure 8). However, for lateral direction, the sidelobe levels in both μ BF169 and μ BF25 are ~ 2 dB higher in the measurement than in the simulation. Additionally,

Chapter 6

the lateral PSF for μBF25 from the experiment has 3 dB higher clutter levels than μBF169 at -30° and 33° . Whereas, the elevational PSF for μBF25 from the experiment has 3 dB higher clutter levels than μBF169 at -30° and 28° . The clutter levels in the experiment are on average ~ 10 dB higher than simulation. The asymmetry of the PSFs and the higher clutter levels in the experiment were due to the non-working receive sub-arrays in the prototype transducer.

6.4. Discussion

The purpose of the present research was to develop a 3D beamforming technique to produce high-quality volume images at a higher volume rate (>80 Hz) than conventional 3D ultrasound imaging, using the designed prototype matrix transducer. Because of the specific architecture of the prototype transducer, existing parallel beamforming techniques were not directly suitable for it. Therefore, in this study, we proposed two multiline 3D beamforming schemes, μBF25 and μBF169 , that utilize the capabilities of the prototype transducer. In simulation, the proposed schemes yielded volumes with image quality similar to the volume using conventional single line acquisition with a fully sampled matrix. This was validated experimentally. The schemes were capable of producing high-quality volume images at a higher frame rate than conventional single line acquisition on the prototype miniaturized matrix transducer.

The receive micro-beamformers allowed to pre-steer to 25 fixed angles in 3D. Hence, for a tx-rx event steered to a certain angle, only a specific sub-volume around that angle was beamformed. To avoid the crossover artifacts, we use sub-volume crossfading. In the μBF25 scheme, overlapping sub-volumes using co-aligned tx-rx events were linearly combined to produce the final volume. In the μBF169 scheme, in addition to the tx-rx events used in μBF25 , sub-volumes from non-aligned tx-rx events were also combined to utilize the overlap between the pre-steered receive beams and the wide transmit beams. The widths of the PSFs at -6 dB and -20 dB in lateral and elevation directions for μBF25 and μBF169 were very similar to the widths of the PSFs of FS4k that would be obtained by full-aperture, line-based volumetric imaging. This was expected as the -6 dB width of the PSF primarily depends on the size of the aperture of the transducer.

In simulation, the normalized intensity distribution showed that the intensity was highest at the direction of transmit and receive steering and dropped at the borders of the transmit and receive zones. This is caused by the combined transmit-receive beamprofile, and it was corrected using the inverse of the normalized intensity profile as a gain/weighting factor for the beamformed RF lines. However, these gains also increased the noise level with the same factors. The lateral shift invariance test showed that after the intensity compensation both μBF25 and μBF169 performed as good as FS4k considering upto -20 dB. However, both the methods had higher intensity variation than FS4k between -20 dB and -40 dB. We performed the shift invariance test and intensity compensation only in the lateral direction, as the same intensity profile is expected in the elevation direction.

To achieve higher volume rate than μBF25 , we also tested the performance of two beamforming schemes using only 9 tx-rx events (μBF9 , 3×3 beams). The quantified PSFs for the two μBF9 methods showed degraded image quality due to larger intensity drops and a higher clutter level. Moreover, the lateral shift invariance test showed that μBF9 with both $\pm 17^\circ$ and $\pm 37^\circ$ produced volume images with larger variance. Hence, for the designed prototype, the proposed μBF9 methods were not suitable for producing volume images with acceptable B-mode image quality. Note that this conclusion may seem different from that drawn in [25], which also uses a 3×3 scheme with a TEE probe with pre-steering capabilities. However, the data in [25] is Doppler-processed to obtain tissue velocity, which is in principle insensitive to amplitude variances, provided that the SNR is sufficient. Our current study aims at B-mode imaging, and therefore the two conclusions do not contradict each other.

The main lobes of the PSFs for μBF169 and μBF25 (shown in Figure 13) closely match with the PSF for μBF169 in simulation, showing the accuracy of the performance of the transducer. However, the sidelobes observed in the measured PSFs were higher than in simulation and also asymmetric (slightly tilted). The differences in the sidelobes are due to the specific distribution of few non-working sub-arrays in the prototype transducer. We think this effect will not be visible with a transducer in which all sub-arrays are functional. The clutter levels of the PSFs in the experiments were higher than in simulation primarily due to the following reasons: the non-working sub-groups, noise introduced by the electronics of the prototype transducer and the external ultrasound system.

From the simulation and experimental results of μBF25 and μBF169 , one could conclude that combining more sub-volumes from different combinations of tx-rx provides only a minor improvement in the image quality. However, it should be noted that for μBF169 , it is also important to have overlaps between the transmit beams and the pre-steered receive beams. A narrow transmit beam will have a lesser overlap, leading to almost no effect in the final volume, even after combining the overlapped sub-volumes. On the other hand, increasing transmit opening angle will reduce the penetration depth causing reduction of the SNR at higher imaging depth. Accordingly, choosing an optimum transmit opening angle for the best achievable image quality is subject to further research.

From these results, it can be concluded that μBF25 produces similar image quality as μBF169 with 7 times higher frame rate, except for a minor increase in clutter. Therefore, to produce a high-quality image at higher frame rate using our prototype, μBF25 is preferred over μBF169 .

There are a few limitations that apply to this study. The 3D beamforming technique was examined only with static pin phantoms. In future research, we will verify the effects of moving tissue on the proposed beamforming techniques, e.g. by imaging dynamic heart phantoms similar to what has been described in [29], [30] followed by in vivo imaging in animals and humans. In addition, our study has not investigated other image quality measures,

Chapter 6

such as axial resolution, contrast ratio (CR), contrast-to-noise ratio (CNR), signal-to-noise ratio (SNR) etc. The axial resolution is mainly determined by the pulse characteristics. As we have used the same pulse characteristics for all the beamforming techniques, we expect no differences in axial resolution among them. The other important image quality parameters (the CR and CNR) have not been evaluated during this research. The clutter levels of the PSFs in experiments were at the most ~ 10 dB higher than in simulation and only present at extreme angles. Therefore, this difference in clutter level is not expected to provide any significant differences in CR and CTR. In μ BF169 we are combining sub-volumes from larger number of neighboring tx-rx events than μ BF25. Therefore, μ BF169 might help in improving the resulting SNR. In addition to that, for μ BF169, the SNR might also be improved because of the suppression of the off-axis energies. Additionally, to improve the uniformity of intensity distribution, the effect of interposed angle transmissions (i.e., at angles of $\pm 9^\circ$ and $\pm 25^\circ$) should be investigated to find if this would provide more optimal uniformity. Although interposed transmissions may provide more uniform overall intensity, the receive sensitivity will be reduced by a few dB in those directions due to the limited pre-steering capability of the ASIC of the prototype transducer.

6.5. Conclusion

We have proposed and implemented two multiline 3D beamforming schemes to produce volumes with good image quality at a maximum volume rate of 300 Hz using a prototype miniaturized matrix transducer with micro-beamformer suitable for pediatric Transesophageal Echocardiography (TEE) and for continuous monitoring in adults. In simulation, the image quality (width of PSFs, lateral shift invariance and clutter level) of the volumes produced by the proposed techniques were similar to the volume using conventional single line acquisition with a hypothetical, idealized fully-sampled matrix transducer of the same size and transmitter-receiver layout as the prototype transducer. The proposed μ BF25 can produce volume images at 169 times higher frame rate than the ideal single-line acquisition method. In addition to that, because of the high volume rate (300 Hz) capability, μ BF25 can be suitable for advanced clinical application such as 3D particle image velocimetry [31] or speckle tracking. The proposed μ BF169 can produce volume images with good quality at a volume rate (>40 Hz) sufficient for B-mode imaging. The main lobe widths of the PSFs in both lateral and elevation direction from the experiment were $\sim 4^\circ$, in good agreement with the simulated PSFs. From these results, we can conclude that the proposed 3D beamforming techniques are suitable for the prototype matrix transducer to produce a high-quality image at a high frame rate.

Acknowledgements

This work is part of the Open Technology Programme with project number 12405 which is (partly) financed by the Netherlands Organisation for Scientific Research (NWO). We like to thank Oldelft Ultrasound, Delft, the Netherlands for their valuable support in transducer manufacturing.

References

- [1] S. C. Zyblewski *et al.*, “Initial Experience With a Miniaturized Multiplane Transesophageal Probe in Small Infants Undergoing Cardiac Operations,” *Ann. Thorac. Surg.*, vol. 89, no. 6, pp. 1990–1994, 2010.
- [2] K. Pushparajah, O. I. Miller, D. Rawlins, A. Barlow, K. Nugent, and J. M. Simpson, “Clinical application of a micro multiplane transoesophageal probe in congenital cardiac disease,” *Cardiol. Young*, vol. 22, no. 2, pp. 170–7, 2012.
- [3] S. Stec, B. Zaborska, M. Sikora-Frc, T. Kryski, and P. Kuakowski, “First experience with microprobe transoesophageal echocardiography in non-sedated adults undergoing atrial fibrillation ablation: Feasibility study and comparison with intracardiac echocardiography,” *Europace*, vol. 13, no. 1, pp. 51–56, 2011.
- [4] M. Taniguchi, T. Akagi, Y. Kijima, H. Ito, and S. Sano, “Transcatheter closure of a large atrial septal defect under microprobe transesophageal echocardiographic guidance,” *Echocardiography*, vol. 29, no. 4, 2012.
- [5] C. E. Wagner, J. S. Bick, B. H. Webster, J. H. Selby, and J. G. Byrne, “Use of a miniaturized transesophageal echocardiographic probe in the intensive care unit for diagnosis and treatment of a hemodynamically unstable patient after aortic valve replacement,” *J. Cardiothorac. Vasc. Anesth.*, vol. 26, no. 1, pp. 95–97, 2012.
- [6] P. M. Kapoor *et al.*, “An update on transesophageal echocardiography views 2016: 2D versus 3D tee views,” *Ann. Card. Anaesth.*, vol. 19, no. Supplement, pp. S56–S72, 2016.
- [7] M. Montealegre-Gallegos, F. Mahmood, K. Owais, P. Hess, J. S. Jainandunsing, and R. Matyal, “Cardiac Output Calculation and Three-Dimensional Echocardiography,” *J. Cardiothorac. Vasc. Anesth.*, vol. 28, no. 3, pp. 547–550, 2014.
- [8] L. H. Frank, A. Chelliah, and C. Sable, “Evaluation of a second-generation microtransesophageal echocardiography transducer and software,” *World J. Pediatr. Congenit. Heart Surg.*, vol. 5, no. 4, pp. 565–70, 2014.
- [9] L. Sugeng *et al.*, “Real-Time Three-Dimensional Transesophageal Echocardiography in Valve Disease: Comparison With Surgical Findings and Evaluation of Prosthetic Valves,” *J. Am. Soc. Echocardiogr.*, vol. 21, no. 12, pp. 1347–1354, 2008.
- [10] I. S. Salgo, “Three-Dimensional Echocardiographic Technology,” *Cardiol. Clin.*, vol. 25, no. 2, pp. 231–239, 2007.
- [11] Siemens, “syngo fourSight TEE view.” [Online]. Available:

- <https://www.healthcare.siemens.com/ultrasound/options-and-upgrades/clinical-applications/syngo-foursight-tee-view>. [Accessed: 25-Jul-2016].
- [12] GE Healthcare, “Vivid™ E9 XDclear™,” 2013.
 - [13] M. Pernot and E. E. Konofagou, “Electromechanical imaging of the myocardium at normal and pathological states,” in *IEEE Ultrasonics Symposium*, 2005, vol. 2, pp. 1091–1094.
 - [14] J. Provost, W.-N. Lee, K. Fujikura, and E. E. Konofagou, “Imaging the electromechanical activity of the heart in vivo,” *Proc. Natl. Acad. Sci. U. S. A.*, vol. 108, no. 21, pp. 8565–70, 2011.
 - [15] D. P. Shattuck, M. D. Weinshenker, S. W. Smith, and O. T. von Ramm, “Explososcan: a parallel processing technique for high speed ultrasound imaging with linear phased arrays,” *J. Acoust. Soc. Am.*, vol. 75, no. 4, pp. 1273–1282, 1984.
 - [16] O. T. Von Ramm, S. W. Smith, and H. G. Pavy, “High-speed Ultrasound Volumetric Imaging System- Part II : Parallel Processing and Image Display,” *IEEE Trans. Ultrason. Ferroelectr. Freq. Control*, vol. 38, no. 2, pp. 100–108, 1991.
 - [17] T. Hergum, T. G. Bjåstad, K. Kristoffersen, and H. Torp, “Parallel Beamforming Using Synthetic Transmit Beams,” *IEEE Trans. Ultrason. Ferroelectr. Freq. Control*, vol. 54, no. 2, pp. 271–280, 2007.
 - [18] L. Tong, A. Ramalli, R. Jasaityte, P. Tortoli, and J. D’Hooge, “Multi-Transmit Beam Forming for Fast Cardiac Imaging — Experimental Validation and In Vivo Application,” vol. 33, no. 6, pp. 1205–1219, 2014.
 - [19] H. Hasegawa and H. Kanai, “High-frame-rate echocardiography using diverging transmit beams and parallel receive beamforming,” *J. Med. Ultrason.*, vol. 38, no. 3, pp. 129–140, 2011.
 - [20] J. Provost *et al.*, “3D ultrafast ultrasound imaging in vivo,” *Phys. Med. Biol.*, vol. 59, no. 19, pp. L1–L13, 2014.
 - [21] P. Santos *et al.*, “Acoustic Output of Multi-Line Transmit Beamforming for Fast Cardiac Imaging,” vol. 62, no. 7, pp. 1320–1330, 2015.
 - [22] A. Austeng and S. Holm, “Sparse 2-D arrays for 3-D phased array imaging - Design methods,” *IEEE Trans. Ultrason. Ferroelectr. Freq. Control*, vol. 49, no. 8, pp. 1073–1086, 2002.
 - [23] S. Blaak, C. T. Lancée, J. G. Bosch, C. Prins, A. F. W. Van Der Steen, and N. De Jong,

- “A matrix transducer for 3D transesophageal echocardiography with a separate transmit and receive subarray,” in *IEEE Ultrasonics Symposium*, 2011, pp. 2341–2344.
- [24] B. Savord and R. Solomon, “Fully sampled matrix transducer for real time 3D ultrasonic imaging,” in *IEEE Ultrasonics Symposium*, 2003, vol. 1, pp. 945–953.
- [25] P. Santos, G. Haugen, L. Løvstakken, E. Samset, and J. D’hooge, “Diverging Wave Volumetric Imaging Using Subaperture Beamforming,” *Ultrason. Ferroelectr. Freq. Control. IEEE Trans.*, vol. 63, no. 12, pp. 2114–2124, 2016.
- [26] C. Chen *et al.*, “A Front-End ASIC With Receive Sub-array Beamforming Integrated With a 32 x 32 PZT Matrix Transducer for 3-D Transesophageal Echocardiography,” *IEEE J. Solid-State Circuits*, vol. 63, no. 1, pp. 1–13, 2017.
- [27] C. Chen *et al.*, “A Prototype PZT Matrix Transducer with Low-Power Integrated Receive ASIC for 3D Transesophageal Echocardiography,” *IEEE Trans. Ultrason. Ferroelectr. Freq. Control*, vol. 63, no. 1, pp. 47–59, 2016.
- [28] J. A. Jensen, “Field: A Program for Simulating Ultrasound Systems,” *Med. Biol. Eng. Comput.*, vol. 34, no. 1, pp. 351–353, 1996.
- [29] F. P. Li, M. Rajchl, J. Moore, and T. M. Peters, “A mitral annulus tracking approach for navigation of off-pump beating heart mitral valve repair,” *Med. Phys.*, vol. 42, no. 1, pp. 456–468, 2015.
- [30] P. W. Wood, P. H. Gibson, and H. Becher, “Three-dimensional echocardiography in a dynamic heart phantom: comparison of five different methods to measure chamber volume using a commercially available software,” *Echo Res. Pract.*, vol. 1, no. 2, pp. 51–60, 2014.
- [31] J. D. Voorneveld, D. Bera, A. F. W. van der Steen, N. de Jong, and J. G. Bosch, “Particle image velocimetry on simulated 3D ultrafast ultrasound from pediatric matrix TEE transducers,” in *Proc. SPIE, Medical Imaging*, 2017, vol. 10139, pp. 1–9.

Chapter 7

Fast volumetric imaging using a matrix TEE probe with partitioned transmit-receive array

D. Bera, F. van den Adel, N. Radeljic-Jakic, B. Lippe, M. Soozande, M.A.P. Pertijs, M.D. Verweij, P. Kruizinga, V. Daeichin, H.J. Vos, A.F.W. van der Steen, J.G. Bosch, N. de Jong. "Fast volumetric imaging using a matrix TEE probe with partitioned transmit-receive array". Ultrasound in Medicine & Biology. Forthcoming 2018.

Chapter 7

We present a 3D multiline parallel beamforming scheme for real-time volumetric ultrasound imaging using a prototype matrix TEE probe with diagonally diced elements and separated transmit and receive arrays. The elements in the smaller rectangular transmit array are directly wired to the ultrasound system. The elements of the larger square receive aperture are grouped in 4×4 -elements sub-arrays by micro-beamforming in an ASIC. We propose a beamforming sequence with 85 transmit-receive events that shows good performance for a volume sector of $60^\circ \times 60^\circ$. The beamforming is validated using Field II simulations, phantom measurements and in-vivo imaging. The proposed parallel beamforming achieves up to 59 Hz volume rate and produces good image quality by angle-weighted combination of overlapping sub-volumes. Point Spread Function, Contrast Ratio and Contrast-to-Noise Ratio in the phantom experiment closely match with simulation. *In-vivo* 3D imaging at 22 Hz volume rate in a healthy adult pig clearly shows the cardiac structures, including valve motion.

7.1. Introduction

Echocardiography is an indispensable diagnostic modality to assess the anatomy and function of the heart. In general, there are two types of echocardiography routinely performed in the clinic: transthoracic echocardiography (TTE), and transesophageal echocardiography (TEE). In TTE, an ultrasound transducer is placed on the chest, and the imaging is performed through an acoustic window in between the ribs. The ultrasound images produced by TTE may suffer from poor image quality because of the limited acoustic window and attenuation, aberration, shadowing and reflections due to the skin, fat, and ribs. In TEE, a transducer is mounted on the tip of a gastroscopic tube and inserted via the mouth into the patient's esophagus to image the heart. Therefore, unlike TTE, TEE images are not deteriorated by the skin, fat, or ribs. Moreover, as the esophagus is located only millimeters away from the heart, the received ultrasound signals in TEE are less attenuated than in TTE. TEE, therefore, produces a superior image quality to TTE, especially for the cardiac structures such as the aorta, pulmonary artery, valves, atria, atrial septum, atrial appendages and even the coronary arteries.

At present, TEE is routinely performed in several heart conditions. It is most commonly used to evaluate valvular disease, prosthetic heart valve dysfunction, cardiac sources of embolism, aortic dissections or aneurysms, and endocarditis [1]. In addition, TEE is performed both to verify the preoperative diagnosis and to monitor the success in many cardiac surgical procedures such as congenital heart disease corrections or valve repair [2].

Several studies have shown that real-time 3D imaging is preferred over 2D imaging in most cardiac diagnostics [3], [4] because of its superior visualization of 3D structures in the heart. Unlike 2D imaging where the acquisitions are performed only at fixed imaging planes corresponding to standard views, in 3D TEE all the important information is captured in a single dataset. In a comprehensive study, an acquired volume can be rotated and cropped at any desired plane to view different cardiac structures. Moreover, 3D TEE provides more consistent measurements of clinically relevant parameters such as volumes of the left ventricle (LV) and the right ventricle (RV), ejection fraction, and cardiac output [4], compared to 2D TEE. Furthermore, 3D TEE allows better morphological and dynamic evaluation of 3D cardiac structures such as the tricuspid valve, the aortic valve, and the mitral valve. Consequently, 3D TEE has become an essential diagnostic modality for a comprehensive examination of cardiac anatomy and function as well as for guiding and monitoring operative and catheter-based interventions [5], [6].

For 3D TEE in adults, there are a number of commercially available matrix array TEE probes: X7-2t from Philips Ultrasound, Bothell, WA [7]; V5M TEE from Siemens Healthineers GmbH, Erlangen, Germany [8]; and 6VT-D from General Electric Healthcare, Amersham, U.K.[9]. These matrix TEE probes are capable of real-time acquisition and live 3D display. The Philips X7-2t probe has an active aperture of $10 \times 10 \text{ mm}^2$ with 2500 elements of frequency range 2-7 MHz (Salgo 2007). The V5M TEE probe has an aperture size of $14.5 \times 11.5 \text{ mm}^2$ (operating

Chapter 7

frequency 3-7 MHz). The 6VT-D TEE probe has an effective aperture size of $14.3 \times 12.7 \text{ mm}^2$, and its operating frequency range is 3-8 MHz. These probes comprise of complicated interconnect circuitry to have integrated transmit and receive elements. In these probes, the transmit beamforming is limited by the capabilities of the on-chip high voltage pulsers. Additionally, using these probes, volume imaging at a high volume rate is achievable only with limited viewing angle and compromised image resolution. To produce volumes of larger viewing angle with high resolution, volume stitching using ECG is used, which reduces the achievable volume rate and may introduce image artifacts with irregular heartbeats. Hence, a 3D TEE probe avoiding these challenges will certainly be very helpful for high frame rate volumetric imaging.

As an alternative to the commercially available 3D TEE probes, Oldelft Ultrasound (Delft, the Netherlands) has recently developed a prototype matrix probe for 3D TEE to facilitate full volume imaging with good resolution at a sufficient frame rate ($>20 \text{ Hz}$) for visualizing the motion of the 3D structures of the heart. To reduce the complexity and power dissipation of the Application-Specific Integrated Circuit (ASIC) design, the prototype matrix probe is divided into separate transmit and receive arrays based on a split-array architecture [11], [12]. This split-array concept offers several advantages. The transmit elements are directly wired out to an external ultrasound system, thereby enabling the use of a compact low-voltage (1.8 V) 180 nm CMOS process for the ASIC, which is only connected to the receive elements. Moreover, the lack of in-probe transmit electronics limits power dissipation and provides full flexibility in defining the transmit pulse shapes; on-chip high voltage pulsers for transmission mostly can only provide very simple pulse shapes. Additionally, for non-fundamental imaging techniques such as (sub)harmonic imaging, in the split-array architecture the transmit and receive arrays could be optimized separately; however, this was not performed in this prototype. To reduce the receive channel count, micro-beamforming (or sub-array beamforming) is performed by applying small analog delays before summing the received RF signals from the individual elements of each sub-array. These micro-beamformed RF receive signals are then transferred to the external ultrasound system [11]. The prototype transducer comprises a small rectangular transmit array at the distal end of the gastroscopic tube and a larger square receive array proximal to the transmit array (Figure 1). The PZT material is diced at an angle of 45° to the azimuth and elevation plane, which produces elements and sub-arrays rotated diagonally. This diagonal dicing reduces the overlap between transmit sidelobes and grating lobes and receive grating lobes for the separated transmitter-receiver layout, as will be shown in this study.

The specific transmitter-receiver layout will affect the image characteristics in several ways. First of all, the misalignment between the transmit and receive beams produced by the separated transmit and receive array will cause slightly tilted speckles and PSFs. Secondly, the combination of rectangular transmit aperture and square receive aperture will produce asymmetric PSFs (narrower in azimuth direction than in elevation direction). Finally, the diagonal dicing will produce transmit and receive grating lobes that are most prominent in the

diagonal directions. Because of these effects, the appearance of the volume image might change based on the orientation of the probe with respect to the imaging object. For any 3D beamforming technique using the prototype probe, these effects on the image characteristics are expected, as they are caused by the intrinsic properties of the prototype. In this paper, we examine these effects and discuss the implications.

To solve the challenge of producing volume images at a sufficiently high frame rate (>20 Hz), parallel beamforming [13] can be used. The relatively wide transmit beams of the small transmit array illuminate a sector of 3D space, and by processing the received channel signals in parallel, several image lines can be reconstructed simultaneously. The PSF of the reconstructed beams is wider; because of the limited transmit focusing. Artifacts could also appear in the resulting images, in the form of sharp intensity changes between scanlines from neighboring transmissions [14]–[16]. We refer to these artifacts as crossover artifacts. One solution to produce good quality volume images at high frame rate using parallel beamforming with a small transmit aperture has already been proposed by us in [17]. In that study, we minimized the crossover artifacts by combining the overlapping sub-volumes corresponding to each transmission. We refer to this scheme as angle-weighted sub-volume combination. In the current study, the prototype matrix probe is very different from the transducer in [17]. It has a different layout and aperture size of the transmit and receive arrays. Accordingly, the transmit and receive opening angles are also different. Additionally, this probe has a more flexible pre-steering capability. Hence, the 3D beamforming technique as proposed in [17] is adapted for the prototype matrix probe based on these characteristics.

In this paper, we describe a 3D beamforming scheme that can produce good quality volume images at an adequate frame rate (>20 Hz) with the prototype adult matrix probe. The scheme uses parallel beamforming. Due to the rectangular transmit aperture, the transmit beam has an elliptical cross-section and more receive scanlines are reconstructed in elevation direction than in the azimuth direction. Hence, to reconstruct a volume (of equal size in elevation and azimuth direction), less transmit beams are required in the elevation direction than in the azimuth direction. The receive sub-arrays are pre-steered to the same direction as the transmit direction, creating one transmit-receive event (tx-rx event). To produce a volume image at an adequate frame rate, a 3D beamforming scheme should use a minimal number of tx-rx events and also should be able to minimize the image artifacts introduced by the parallel beamforming. Therefore, to judiciously choose the tx-rx events scheme for high frame rate volume imaging, we first show the results from the acoustic characterization of the transmit array and the receive array. Based on these results, we propose a parallel beamforming scheme exploiting the capabilities of the prototype probe. The proposed 3D beamforming scheme requires 85 tx-rx events (17 directions in azimuth \times 5 directions in elevation) to reconstruct a volume of $60^\circ \times 60^\circ$ field of view. To avoid the crossover artifacts in the final image, we use angle-weighted sub-volume combination in the proposed 3D beamforming scheme. In this paper, we validate and compare the performance of the 3D beamforming scheme in both simulation and experiment.

Chapter 7

Finally, we did an in vivo acquisition on a porcine heart to show the real-time 3D imaging capability of the prototype matrix probe.

7.2. Materials and methods

7.2.1. Description of the prototype matrix transducer

Figure 1 shows the probe and the layout of transmit and receive elements of the prototype matrix probe. The probe has an outer dimension of $15 \times 11 \times 35$ mm³ which is similar to other TEE probes. The acoustic aperture measures about 10×9 mm² overall and consists of 2176 individual PZT elements that operate at an ultrasound frequency of 5 MHz. The transducer array is fabricated by dicing a bulk piezo-electrical material (3265HD, CTS Corporation, Albuquerque, MN, USA) with a pitch of 181 μ m and a dicing kerf width of 30 μ m at an angle of 45°, which produces elements rotated by 45°. The PZT stack is mounted directly on top of a front-end ASIC using a PZT-on-CMOS integration scheme.

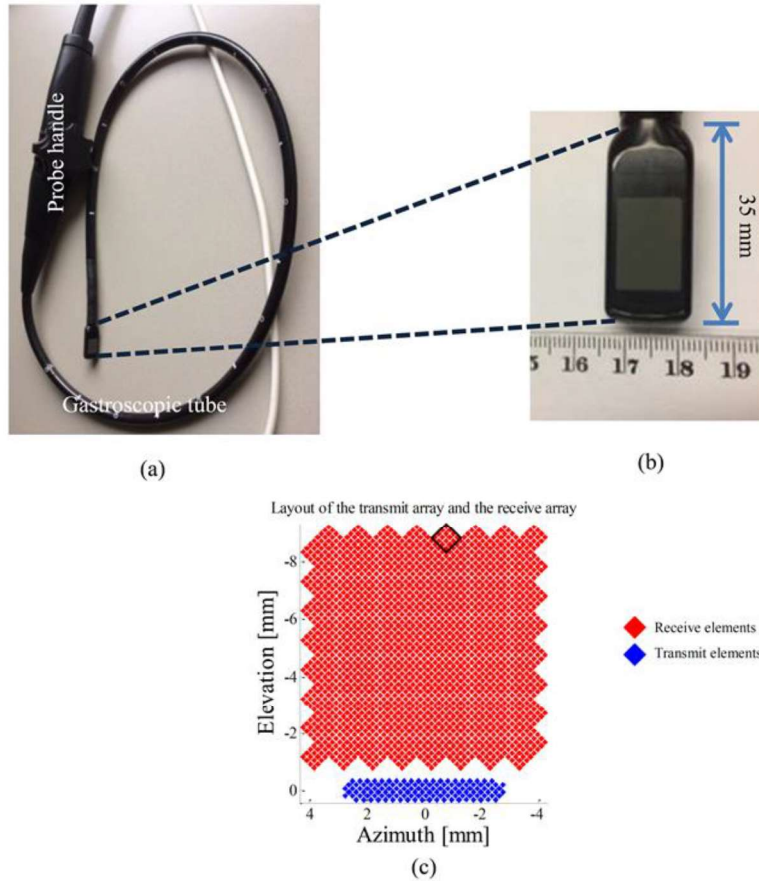


Figure 1: The prototype matrix TEE probe. (a) The probe with the rectangular tip, the probe handle and the gastroscopic tube, (b) a zoom-in of the tip, and (c) the effective aperture, with element-wise layout of the transmit and receive arrays. The black square indicates a 4×4 receive sub-array.

Fast volumetric imaging using a matrix TEE probe

The rectangular transmit aperture area ($5.76 \times 0.90 \text{ mm}^2$) consists of 128 elements distributed in 6 rows at the distal side of the tube. The transmit elements are wired out directly to the external ultrasound scanner. The receive aperture ($8.7 \times 8.7 \text{ mm}^2$) comprises 2048 elements that are connected to the front-end ASIC for micro-beamforming. The receive elements are divided into 128 sub-arrays of 4×4 elements. Each sub-array has a micro-beamformer that applies analog delays to the signals from the individual elements before summing. Thus, the micro-beamformers reduce the number of required receive cables by a factor of 16, to 128. The analog delays for the elements in a sub-array can be programmed from 0 ns up to 550 ns in steps of 10 ns. Thus, an individual sub-array can be steered to any angle in the 3D hemisphere. A time gain compensation is configured as an attenuation of the signal from individual receive sub-arrays. The attenuation ranges from 16 dB to 0 dB. The attenuation is applied with time steps of 640 ns up to a maximum time of $\sim 80 \mu\text{s}$. The prototype is realized as a fully functional device, mounted in a standard gastroscopic tube with manipulation handle.

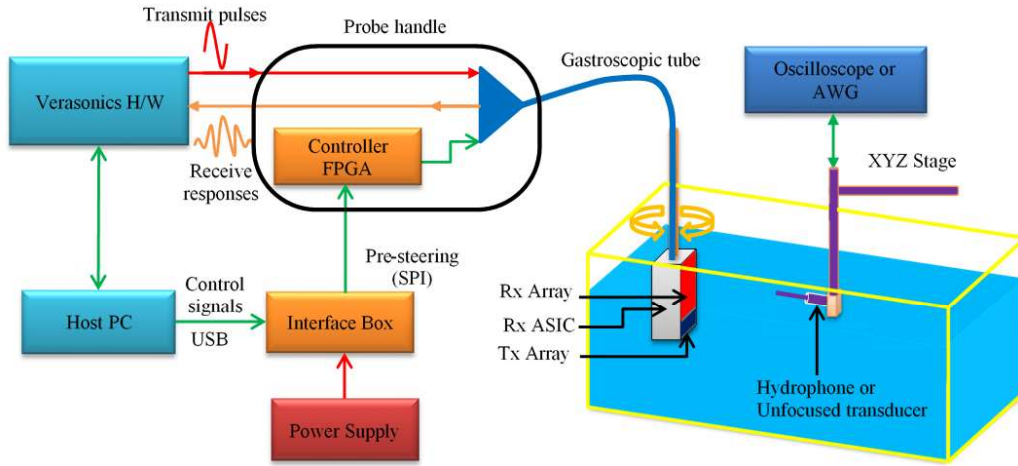


Figure 2: Measurement setup for acoustic characterization. SPI = Serial Peripheral Interface; USB = Universal Serial Bus.

7.2.2. Setup for the acoustic characterization of the transmit and receive array

The prototype matrix probe was mounted on the rotating arm of a fully automated UMS3 Scanning Tank (Precision Acoustics, Dorchester, U.K.) as shown in Figure 2. To characterize the transmit array, a 0.2 mm needle hydrophone with integrated amplifier (Precision Acoustics, Dorchester, U.K.) was mounted on the XYZ stage of the water tank. The amplified hydrophone signals were captured using an oscilloscope (DSOX4054A, Keysight Technologies, Santa Clara, CA, USA). For the receive characterization, the needle hydrophone was replaced with an unfocused 0.5-inch transducer (V309, 5.8 MHz center frequency with 80% bandwidth, Olympus Scientific Solutions, Waltham, MA, USA). This external transducer was excited with an arbitrary waveform generator (AWG) (33250A, Keysight Technologies, Santa Clara, CA, USA). The transmit array and the receive array were evaluated separately. The transmit

Chapter 7

elements were connected to 128 channels of a Verasonics V1 ultrasound system (Verasonics Inc. Kirkland, Washington, USA). The ultrasound system was configured to generate pulses with a peak-to-peak of 15 V for all the transmit elements with appropriate time delays to steer the transmit beams. The micro-beamformed RF signals from the 128 receive sub-arrays were recorded simultaneously using the ultrasound system. In this paper, the set of output RF signals from all the sub-arrays from a single tx-rx event is referred to as a micro-beamformed RF (μ BRF) dataset. The host PC was connected to the controller FPGA in the handle via an interface box. This interface box converts the PC's USB interface to the Serial Peripheral Interface (SPI) used by the FPGA and ASIC for control signals and pre-steering settings. The interface box was also connected to a power supply (± 5 V) for the controller FPGA and the ASIC.

7.2.2.1. Characterization of the transmit array

To characterize the transmit array, we measured the transmit beam profiles (both non-steered and steered), the transmit efficiency and the frequency response. Each of the 128 transmit elements was excited by a 5 MHz single cycle sinusoidal pulse from the ultrasound system, and the acoustic signal was recorded on-axis using the hydrophone placed at a distance of 20 mm from the surface of the transmit array. The 2D beam profiles of the transmit array were measured on a C-plane at 20 mm by the hydrophone mounted on the XYZ stage of the water tank. To measure the transmit beam profiles, the transmit array was steered to $(0^\circ, 0^\circ)$, $(30^\circ, 0^\circ)$ and $(30^\circ, 30^\circ)$ [expressed as (θ, φ) , where θ is the angle in azimuth direction and φ is the angle in elevation direction]. For every steering angle, the peak-to-peak pressure was recorded by the hydrophone at each scanning position. The transmit efficiency and the frequency response of the transmit array were computed based on the highest peak-to-peak acoustic pressure signal received by the hydrophone for $(0^\circ, 0^\circ)$ steering.

7.2.2.2. Characterization of the receive array

To characterize the receive array, we measured the receive sensitivity variation among the sub-arrays, the receive beam profiles of the sub-arrays (for several pre-steering angles) and the receive efficiency. For the receive characterization, the prototype was mounted on the rotational arm of the water tank (as shown in Figure 2), in front of the unfocused single-element ultrasound transducer used as a source. The source transducer was excited with a single-cycle 5 MHz sinusoidal pulse, generated from the AWG. To assure a plane-wave excitation, the source transducer was placed at a sufficient distance from the receive array. In order to mimic the echoes from different angles, the prototype was mechanically rotated in azimuth direction from -60° to $+60^\circ$ in steps of 2° . The received acoustic signals from the 128 sub-arrays were captured at every angle using the ultrasound system, and the beam profiles of the individual sub-arrays were computed. For each pre-steering angle, the beam profile of the entire receive array was calculated by delaying the signals from all the sub-arrays before summing. To measure the receive beam profiles, the receive sub-arrays were pre-steered to 5 angles (-40° to

+40° with steps of 20°) in the azimuth direction. To measure the sensitivity of the receive sub-groups and receive efficiency of a sub-group we used the data acquired for (0°,0°) pre-steering. The beam profiles in elevation direction are considered to be the same because of the symmetry of the receive array.

7.2.3. Parallel beamforming with micro-beamformed datasets

We selected the proposed beamforming scheme based on three arguments. First, the transmit beams should have sufficient overlap to insonify the entire 60°×60° viewing angle with sufficient amplitude and allow the angle-weighted combination of several sub-volumes to avoid the crossover artifacts. The transmit aperture produces a beam with a theoretical -6 dB opening angle of ~4° in azimuth direction and ~27° in elevation direction. The pre-steered sub-array receive beams have a theoretical -6 dB opening angle of ~20° in both azimuth and elevation directions. Hence, to cover the entire viewing angle, at least fifteen transmissions in azimuth direction and at least three transmissions in elevation direction are required, but a larger number is beneficial for sufficient transmit/receive amplitude. This should be faced with a trade-off to the second argument, which is that less transmissions means higher volumetric frame rate. With a final aim of roughly 50 volumes per second and a maximum of 5000 tx-rx events per second, this would lead to a maximum of 100 transmissions per volume. The third argument is that the extremities of the volume may be allowed to have a little lower quality in terms of SNR/signal amplitude, contrast, and resolution, as the natural emphasis will, in general, be on the central part of the imaged volume. Based on these three arguments, we propose a 3D parallel beamforming scheme which is steered to 17×5 angles, distributed over a combination of azimuth directions of -24°:3°:24° and elevation directions of -20°:10°:20°. The angular weights for the combination of the sub-volume receive scanlines were chosen as coefficients from a Hanning window, based on the angular distance of the scanlines from the tx-rx direction.

To summarize, the following steps were performed to produce the final volume with 121×121 scanlines:

Step 1: A wide transmit beam was steered to one angle in 3D space from the set of 17×5 predefined angles.

Step 2: The receive sub-arrays were pre-steered to the same transmit angle and the 128-channel μ BRF dataset was acquired.

Step 3: To produce a sub-volume with 3D beamformed scanlines (~13×41 lines near the transmit/receive angle), Delay-and-Sum parallel beamforming using dynamic receive focusing was applied to the μ BRF dataset of the tx-rx event.

Repeat step 1-3 for all 85 angles (85 tx-rx events).

Chapter 7

Step 4: The scanlines from the overlapping sub-volumes of neighboring tx-rx events were linearly combined to produce the final scanlines by angle-weighting.

7.2.4. Ideal delay-and-sum (DAS) beamforming

To compare the image quality of the volumes produced by the proposed beamforming scheme with ideal volume images, in simulation we produced volume images with a slow but ideal DAS 3D beamforming. To achieve the best image quality with the given transmit and receive aperture, for each of the 61×61 scanlines in the volume one tx-rx event was used, where the transmit steering and receive pre-steering were set to the exact direction of the scanlines. Comparison with the acquired volumes generated with the proposed beamforming scheme was done after scan conversion.

7.2.5. Imaging simulations and experimental setup

7.2.5.1. Simulations

The transducer parameters used in simulations using FieldII [18] are shown in Table 1. The impulse response of the transducer was modelled as a 4 cycle sinusoid (46% fractional bandwidth). The parameters used for the acoustic characterization and the 3D imaging in both simulation and experiment are shown in Table 2 and Table 3, respectively. In Table 3, the parameters used for the simulation were chosen to produce volume images using ideal DAS beamforming.

Table 1: Transducer simulation parameters

	Parameters	Value
Transducer	Center frequency	5 MHz
	Number of transmit elements	128
	Number of receive elements	2048
	Diagonal pitch	181 μm
	Number of receive sub-arrays	128
	Receive sub-array diagonal pitch	724 μm
Simulation parameters	Excitation pulse	Single sinusoid with a Hamming window
	Apodization	Box-car
	Sampling frequency	100 MHz

Fast volumetric imaging using a matrix TEE probe

Table 2: Parameters for acoustic characterization

Transmit Characterization	Transmit focus	20 mm
	Transmit steering angles	(0°,0°), (30°,0°) and (30°,30°)
Receive Characterization	Receive pre-steering angles	[-40°: 20°: +40°] (-40° to +40° with steps of 20°) in azimuth direction

Table 3: Imaging parameters

	Parameters	Value
For simulation	Transmit steering angles	[-30°: 1°: +30°] in both azimuth and elevation direction
	Receive pre-steering angles	61×61= 3721 angles co-aligned with the transmit directions
	Field of view	60°×60°
	Number of receive scanlines	61×61
	Transmit focus	-100 mm
For experiment	Receive focusing	Dynamic receive focus
	Transmit steering angles	[-24°: 3°: +24°] in azimuth direction in combination with [-20°: 10°: +20°] in elevation direction
	Receive pre-steering angles	85 angles co-aligned with the transmit directions
	Field of view	60°×60°
	Number of receive scanlines	121×121
	Transmit focus	-100 mm

7.2.5.2. Experimental setup for 3D imaging

To investigate the performance of the proposed 3D beamforming scheme, the micro-beamformed datasets were acquired with the prototype probe connected to the Verasonics ultrasound system. The experiment was done with a commercial tissue phantom (multi-purpose ultrasound phantom 040-GSE, CIRS, Virginia, USA) (CIRS) with 0.5 dB/MHz/cm attenuation and containing wire targets and hyperechoic and anechoic cysts. We performed imaging experiments for three orientations of the prototype matrix probe on the phantom. Figure 3 shows one of the three setups, where the central azimuth plane of the prototype matrix probe was positioned perpendicular to the wires and to the axis of the hyperechoic cylinder in the phantom. To show the effects of the rectangular transmit aperture and the diagonal dicing, the other two imaging orientations were achieved by rotating the probe to ~45° and ~90° with respect to the position shown in Figure 3. The beam was produced by placing a virtual source

Chapter 7

behind the transducer plane at a distance of -100 mm, effectively producing a plane steered wave. The pulse repetition time was 0.200 ms ($85 \times 0.2 \text{ ms} = 17 \text{ ms}$ per volume recording) and the wait time between frame recordings was 28.5 ms, needed for reliable synchronization in the current setup. This synchronization issue was caused by a slow data connection for control signals, not by the prototype itself. The effective volume rate was therefore not 59 Hz but 22 Hz. The μ BRF dataset received by the sub-arrays was acquired with fixed gain settings in the ultrasound system, digitized at 20 MHz sampling rate, and stored for post-processing. Before 3D beamforming, the μ BRF datasets were filtered with a band-pass filter of 100% bandwidth with 5 MHz center frequency.

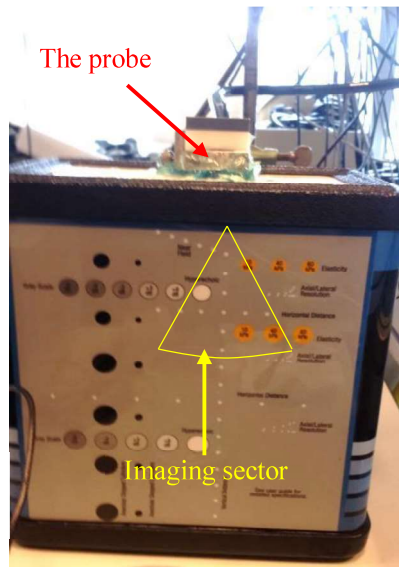


Figure 3: Experimental imaging setup for the position of the probe having the central azimuth plane perpendicular to the structures in the phantom

7.2.5.3. In-vivo porcine experiment

For the *in vivo* experiment, imaging was performed in an experimental intervention in an adult pig of 50 kg (Erasmus MC Animal Experiments Committee protocol #109-14-12). The anesthetized pig was laid down in the supine position and ventilated. Since the pig esophagus is oriented differently than in humans with respect to the heart, direct transesophageal imaging in pigs is cumbersome. Therefore, the imaging was performed through a hole in the chest wall and the diaphragm. The probe head was positioned directly next to the heart to get a view similar to the standard short axis (SAX) view. Afterwards, imaging was done in an open-chest setting, with the probe head on the anterior heart wall. The acquisitions were carried out by an experienced cardiologist. The imaging settings were kept the same as in the phantom imaging. A 2.5-s acquisition was recorded up to ~90 mm depth in each view using the same tx-rx scheme

as the phantom imaging, but using a transmit excitation pulse with a peak-to-peak of 40 V. We oriented the probe to capture the following 3D structures of the heart: the aortic valve, the mitral valve, the tricuspid valve and the interventricular septum.

7.2.5.4. Measures of image quality

A. Point Spread Function (PSF): To estimate the performance of the proposed 3D beamforming scheme, the widths of PSFs in the azimuth and elevation directions were measured at -6 dB.

B. Contrast to Noise Ratio (CNR) and Contrast Ratio (CR): The performance of the proposed 3D beamforming scheme on the cysts was estimated using the CNR and CR as defined in [19], which are given by

$$CNR = \frac{\mu_s - \mu_c}{\sqrt{(\sigma_s^2 + \sigma_c^2)/2}} \quad (2)$$

$$CR = \frac{\mu_s - \mu_c}{(\mu_s + \mu_c)/2} \quad (3)$$

where μ_s and μ_c are the mean amplitudes of a speckle region and a cyst region, respectively, and σ_s^2 and σ_c^2 represent the variances of the speckle and cyst region.

7.3. Results

7.3.1. Transmit and receive beam characteristics

7.3.1.1. Transmit characteristics

Figure 4 shows the measured beam profiles of a single transmit element in azimuth and elevation direction at 20 mm depth. From this figure, it can be observed that the full width half maximum (FWHM) beamwidth of a single element is $\sim 50^\circ$. Figure 5 shows the time trace at 20 mm for the position of maximum peak-to-peak pressure signal received by the hydrophone for the same transmit element when excited using a pulse with a peak-to-peak of 15 V. For this transmit element, the transmit efficiency (calculated using the peak-to-peak pressure of 10 kPa) was 0.67 kPa/V.

Figure 6 shows the measured and simulated beam profiles of the entire transmit array when steered to $(0^\circ, 0^\circ)$. As expected, due to the rectangular transmit aperture the FWHM in azimuth direction was narrower than the elevation direction. The FWHM in azimuth direction was $\sim 3.6^\circ$ in the measurement compared with $\sim 4^\circ$ in the simulation. In elevation direction, the FWHM was $\sim 20^\circ$ in the measurement compared to $\sim 28^\circ$ in the simulation. The measured beam profile in elevation direction was narrower than in the simulation. One of the reasons could be a misalignment of the measurement plane with respect to the transmit beam; as will be visible in

Chapter 7

Figure 7(a) below, a small misalignment in the azimuth plane will result in a large mismatch in the elevation beam profile. This effect is much less prominent for the azimuth beam profile.

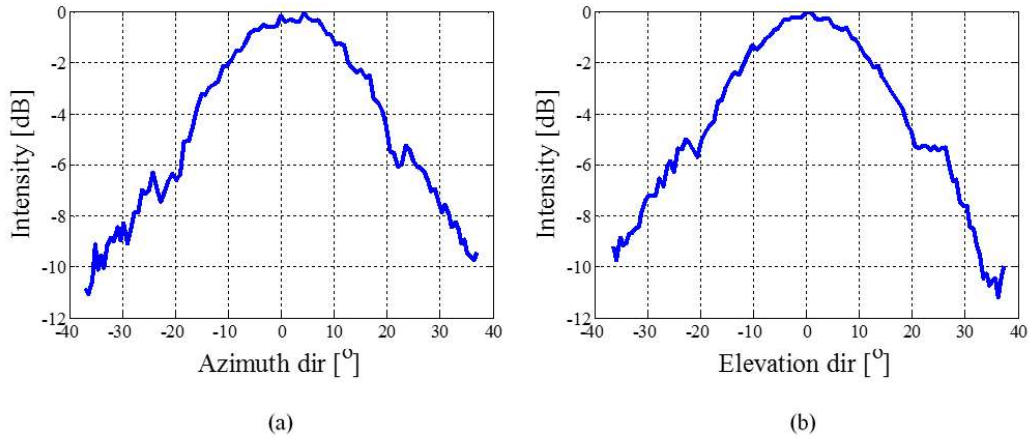


Figure 4: Beam profiles of a single transmit element in (a) azimuth direction and (b) elevation direction.

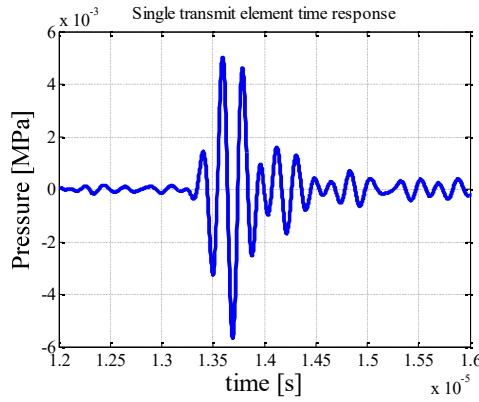


Figure 5: The time trace at 20 mm for the position of the maximum peak-to-peak pressure signal received by the hydrophone for a single transmit element

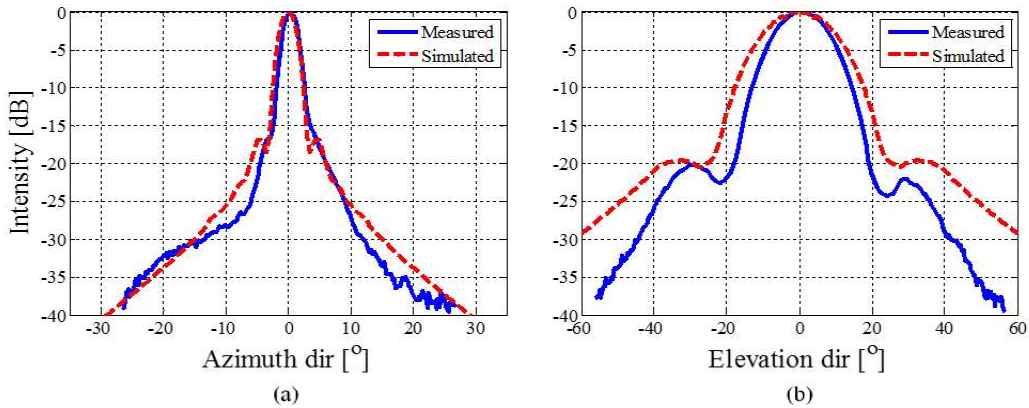


Figure 6: Beam profiles of the transmit array in (a) azimuth direction and (b) elevation direction

Figure 7 shows the measured and simulated 2D beam profiles on a C-plane at 20 mm for three steering angles $[(0^\circ, 0^\circ), (30^\circ, 0^\circ) \text{ and } (30^\circ, 30^\circ)]$. From this figure, it can be observed that the measured beam profiles were very similar to the simulated beam profiles, although in the measured beam profiles shown in Figure 7(b) and (c) the clutter level was 10 dB higher than in simulation. In Figure 7(c), for steering to $(30^\circ, 30^\circ)$, the transmit grating lobes appeared in the diagonal direction at $(-35^\circ, -35^\circ)$. This is due to the element pitch of $181\mu\text{m}$ being larger than $\lambda/2$ for the transmit array in the diagonal direction.

Figure 8 shows the time trace of the transmit array at 20 mm for the position of the maximum peak-to-peak pressure signal received by the hydrophone and the corresponding frequency response of the transmit array. From this figure, it can be observed that for an excitation using a single sinusoid with a peak-to-peak of 15 V, the maximum peak-to-peak pressure generated by the transmit array was 1.2 MPa. The frequency response shows that the transmit array has a center frequency of 4.8 MHz with 50% bandwidth.

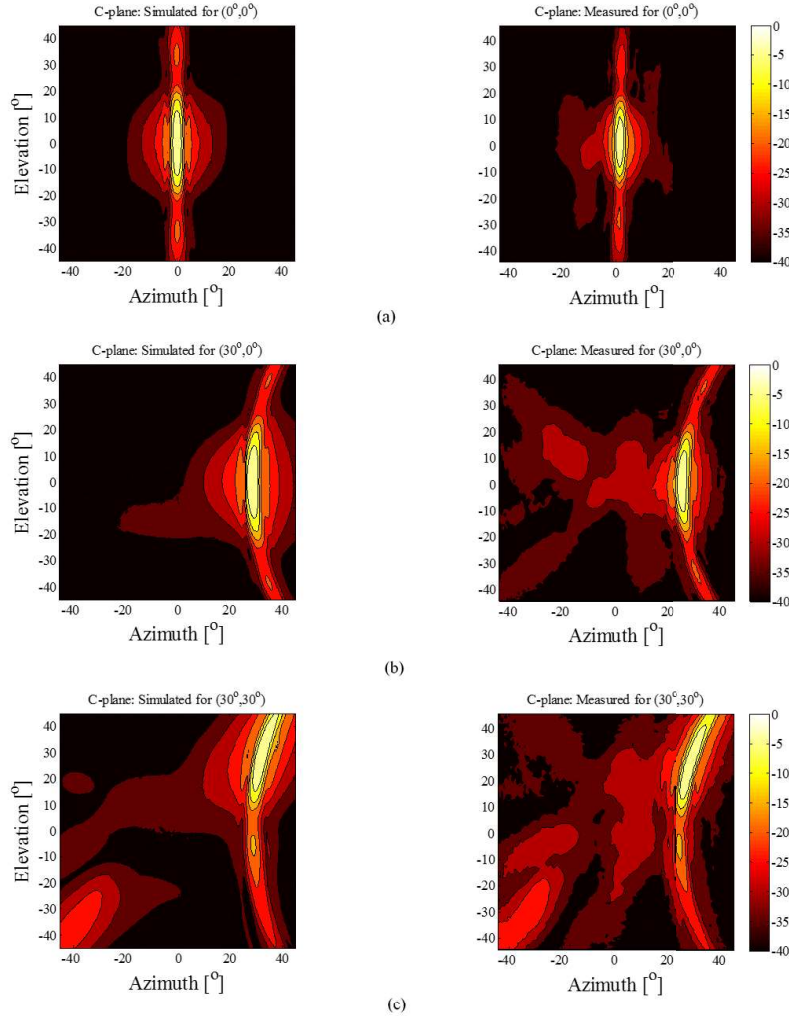


Figure 7: Transmit beam profiles on a C-plane at 20 mm. Simulated (left side) and measured (right side) for steering to (a) $(0^\circ, 0^\circ)$, (b) $(30^\circ, 0^\circ)$, (c) $(30^\circ, 30^\circ)$

Chapter 7

7.3.1.2. Receive characteristics

The receive beam profiles of two sub-arrays (chosen randomly) for 5 pre-steering angles ($-40^\circ:20^\circ:40^\circ$ in azimuth direction) are shown in Figure 9. It can be observed that the directivity patterns of the sub-arrays are nearly uniform for all the pre-steering directions. The received intensity drops only by ~ 3 dB from pre-steering $(0^\circ, 0^\circ)$ to pre-steering $(0^\circ, 40^\circ)$. This suggests that even with micro-beamforming it is possible to achieve a wide directivity pattern similar to a single element. Additionally, there is no significant difference in the directivity patterns of individual sub-arrays. The FWHMs of the received beams for the sub-arrays are $\sim 30^\circ$ compared to the theoretical value of $\sim 20^\circ$. The theoretical FWHM was computed considering a circular transducer with a diameter ($1.024 \mu\text{m}$) same as the width of a sub-array in elevation/azimuth direction.

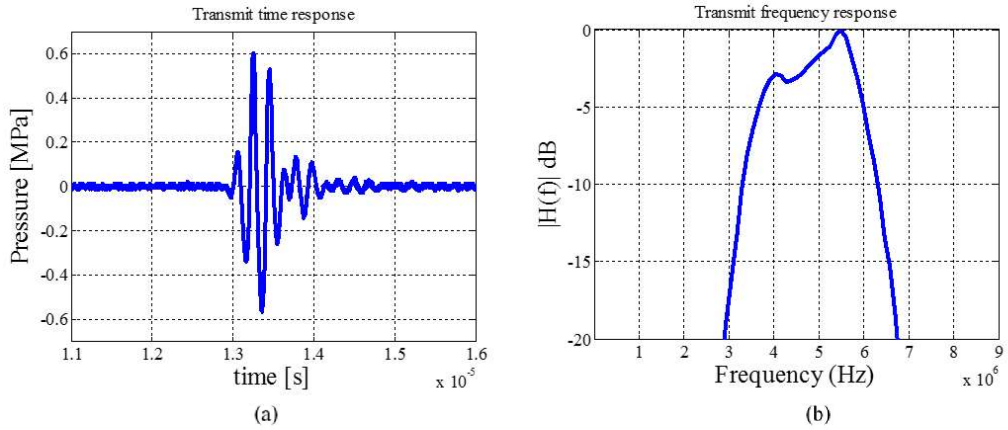


Figure 8: (a) The time trace of the transmit array at 20 mm for the position of maximum peak-to-peak pressure signal received by the hydrophone, (b) the frequency response of the transmit array

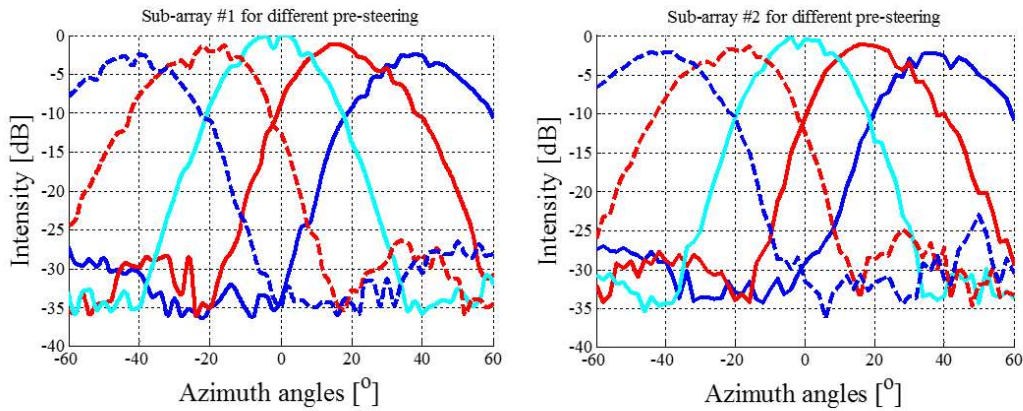


Figure 9: Receive beam profiles of two sub-arrays for 5 pre-steering angles

Fast volumetric imaging using a matrix TEE probe

The receive sensitivity variation among the sub-arrays for pre-steering to $(0^\circ, 0^\circ)$ is shown in Figure 10. From this figure, it can be observed that the sub-arrays have almost a uniform receive sensitivity (variation of ~ 2 dB).

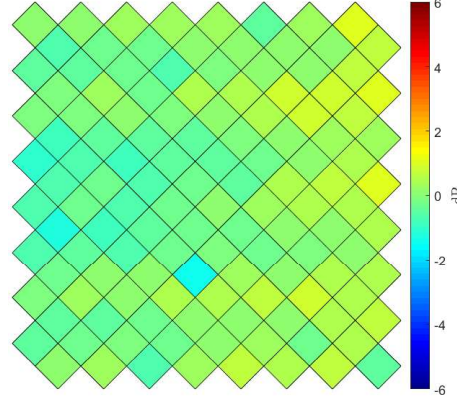


Figure 10: Receive sensitivity variation among the sub-arrays for pre-steering to $(0^\circ, 0^\circ)$

To measure the beam profiles of the complete receive array, for each pre-steering angle, delays were computed based on the center position of each sub-array for that steering angle and applied to the RF signals. Figure 11 depicts the beam profiles of the receive array for 5 pre-steering angles $(-40^\circ:20^\circ:40^\circ)$. From this figure, it can be observed that by applying different pre-steering to the sub-arrays, it is possible to achieve good sensitivity over a wide sector in 3D space (opening angle at least 60 degrees). The mean FWHM of the received beam for the receive array was $\sim 2.5^\circ$ which is similar to the theoretical value of $\sim 2.3^\circ$. The peaks of the beam profiles for all the 5 pre-steerings were shifted by -2° . This may have been caused by a misalignment in the measurement setup. Based on the symmetry of the receive array, the beam profiles in the elevation direction are expected to be the same as in the azimuth direction.

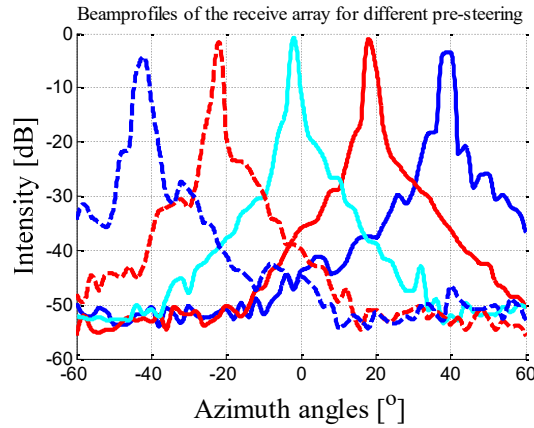


Figure 11: Beam profiles of the receive array for 5 pre-steering angles

Chapter 7

7.3.2. Effect of the diagonal dicing and the transmit-receive layout on the PSF

To estimate the effect of the diagonal dicing we have simulated the pulse-echo beam profile for a $(30^\circ, 30^\circ)$ steering angle. In Figure 12 we show the 2D beam profiles of the transmit array, receive array and the pulse-echo on a C-plane at 20 mm for a steering angle of $(30^\circ, 30^\circ)$. From this figure, it can be concluded that the grating lobes of the transmit and receive array are non-overlapping. Due to the diagonal dicing and the eccentric transmit array, the receive grating lobes do not overlap with the wide transmit sidelobes in the elevation direction. Thus, in the pulse-echo beam profile, the off-axis energies are greatly suppressed. The FWHMs in azimuth and elevation directions were 2.3° and 2.6° , respectively. Due to the wider transmit beam profile in elevation direction, the FWHM in elevation direction was slightly wider compared to the azimuth direction.

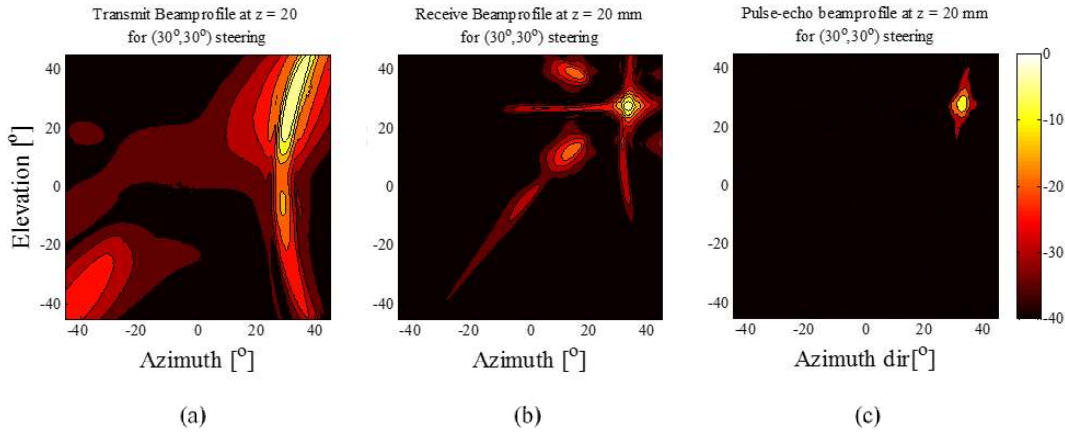


Figure 12: 2D Beam profiles on the C-plane at $z = 20$ mm. (a) Transmit, (b) Receive and (c) Pulse-echo

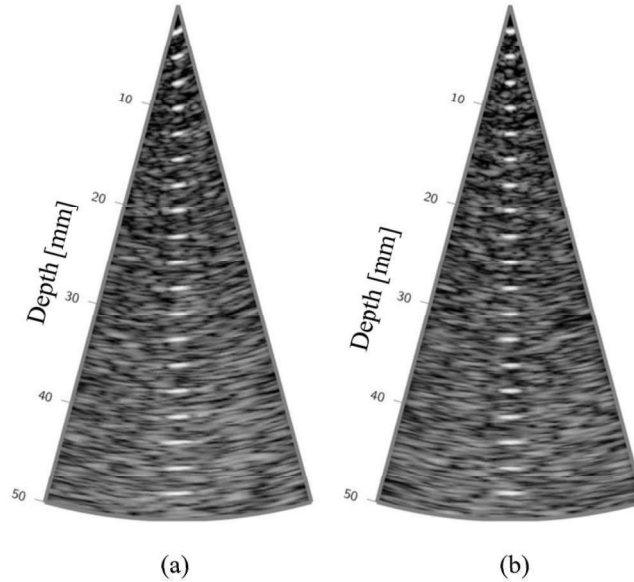


Figure 13: 2D slices of the simulated point scatterers. (a) central elevation plane and (b) central azimuth plane.

To further estimate the effect of the separated transmit and receive array, we simulated imaging of 18 point scatterers placed at different depths (starting from 2.5 mm to 50 mm with an interval of 2.5 mm) in the central region. Figure 13 shows the central elevation and central azimuth planes of the volume with the point scatterers. The dynamic range of the displayed images is 40 dB. From this figure, it can be observed that the PSFs at depths <20 mm are tilted. This is caused by the non-aligned transmit and receive beams close to the transducer. However, this effect was not at all visible at larger depths.

7.3.3. 3D beamforming

7.3.3.1. Volume images of phantom

Figure 14 shows the three volume rendered images of the phantom produced using the proposed 3D beamforming scheme for the three orientations of the prototype probe: azimuth plane perpendicular to the wires and hyperechoic cyst (shown in Figure 3) and by rotating the probe to $\sim 45^\circ$ and $\sim 90^\circ$ with respect to the first position. In this figure, the structures (wires at different depths and hyperechoic cylinder) of the CIRS phantom are clearly visible in all the three volumes. The color in the rendered volume changes from white to blue as we move from the front to the back. Because of the specular reflections from the wires, only the reflections perpendicular to the wires are visible. For the three probe orientations, the rendered volumes were rotated to get the same view of the hyperechoic cylinder and the wires. From this figure, it can be observed that the reflection patterns of these three images are slightly different. As expected, the orientation of the tilted PSFs at the shallower depths changes depending on the orientation of the probe. However, the hyperechoic cylinder and the wires at a larger depth appear very similar in all three images. This suggests that the separated transmit-receive array and diagonal dicing have no severe effect on the volume images.

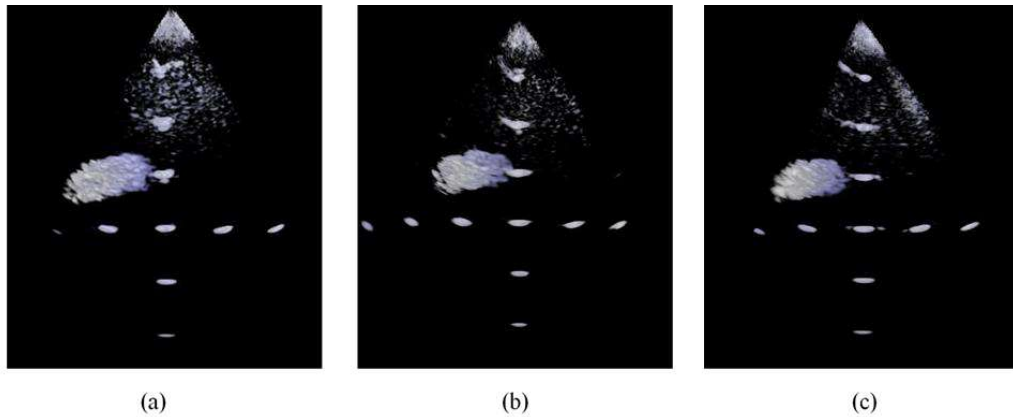


Figure 14: Volume rendered 2D images of the CIRS phantom for the three orientations of the probe. The angles between the azimuth plane and the structures in the phantom were (a) $\sim 90^\circ$, (b) $\sim 45^\circ$ and (c) $\sim 0^\circ$. The volumes were reconstructed until 60 mm depth with $60^\circ \times 60^\circ$ field of view.

Chapter 7

Figure 15 shows the azimuth plane at $y = 4$ mm and the elevation planes at $x = 12$ mm and $x = 3$ mm of the volume produced for the imaging setup as depicted in Figure 3. The azimuth plane is almost perpendicular to the wires and to the axis of the hyperechoic cylinder. As a result, in Figure 15(a) the wires appear as points, and the hyperechoic cylinder as a hyperechoic circular region (cross-sectional area) at $z = 30$ mm. The hyperechoic cylinder is clearly visible in the elevation plane shown in Figure 15(b). Although the wires are parallel to the elevation plane shown in Figure 15(c), they do not appear as elongated intensity lines. In Figure 15(c), the wires at 10 mm and 20 mm appear as tilted similar to the simulation results in Figure 13. This is caused by the eccentric transmit array.

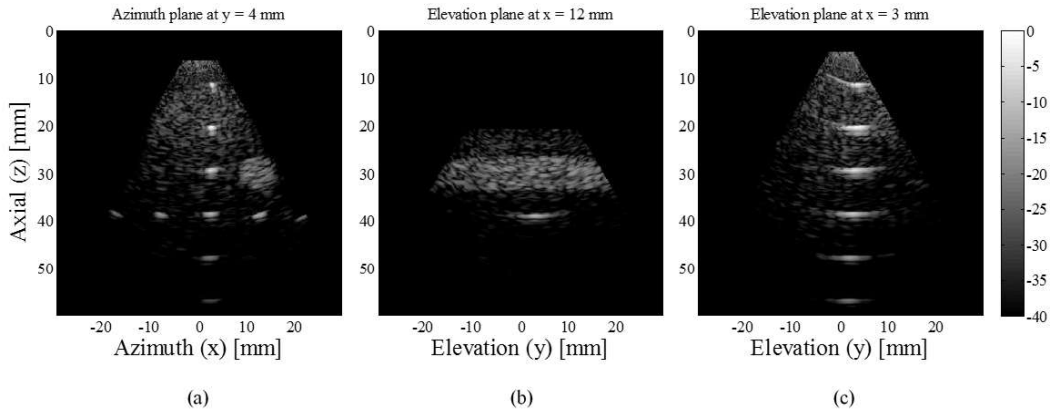


Figure 15: 2D images in (a) Azimuth plane at $y = 4$ mm, Elevation plane at (a) $x = 12$ mm and (b) $x = 3$ mm

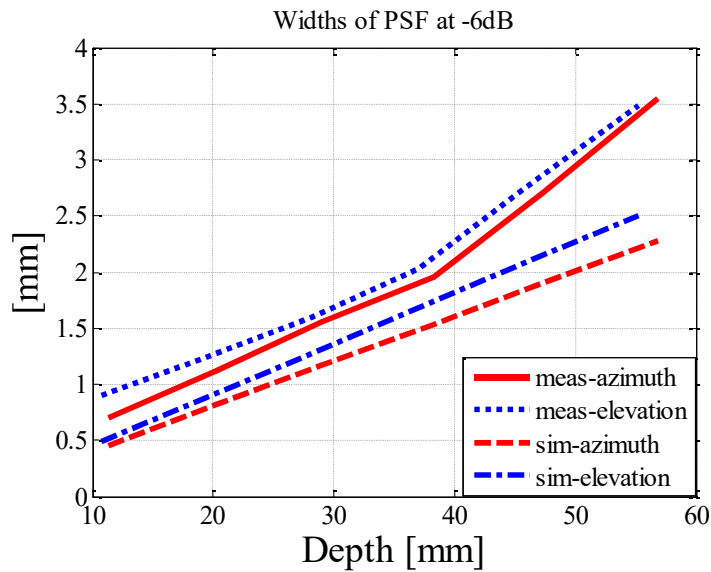


Figure 16: Width of PSF for simulation and measurement in azimuth and elevation directions.

7.3.3.2. Width of PSF in azimuth and elevation directions

Figure 16 shows the width of the PSF at different depths in azimuth and elevation direction for the simulation and experiment. In both elevation and azimuth directions, the width of the PSF at -6 dB averaged over the different depths is a factor 1.4 of the simulation with the slow but ideal DAS beamforming. Both in experiment and simulation, the widths of PSFs in elevation direction were slightly (average ~8%) broader than in the azimuth direction. This was expected because of the smaller aperture size in the elevation direction of the rectangular transmit array (as also visible in Figure 12).

7.3.3.3. 3D imaging of an anechoic stepped cylinder in the CIRS phantom

To estimate the imaging performance of the prototype probe on cysts, the anechoic stepped of the CIRS phantom was imaged. Figure 17 shows the 2D azimuth and elevation planes of the volume produced by the proposed 3D beamforming scheme, where the azimuth plane was perpendicular to the anechoic cylinder axis. In Figure 17(a), the anechoic cylinder appears at 20 mm as a circular cystic region and in Figure 17(b) the stepped radius of the cylinder is visible. To quantify the imaging performance of the proposed beamforming scheme on the cyst, we computed CNR and CR as defined in Eq. (2) and (3) for both simulation and experiment, using a circular window of radius 1.5 mm [shown in Figure 17(a)]. The CNR values for the simulation and experiment were 2.8 and 2.5, respectively. The CR value for the simulation was 1.6 compared with 1.18 in the experiment. From these CNR and CR values, we can conclude that the image quality of the volume produced in the experiment is similar to the simulation with ideal DAS beamforming.

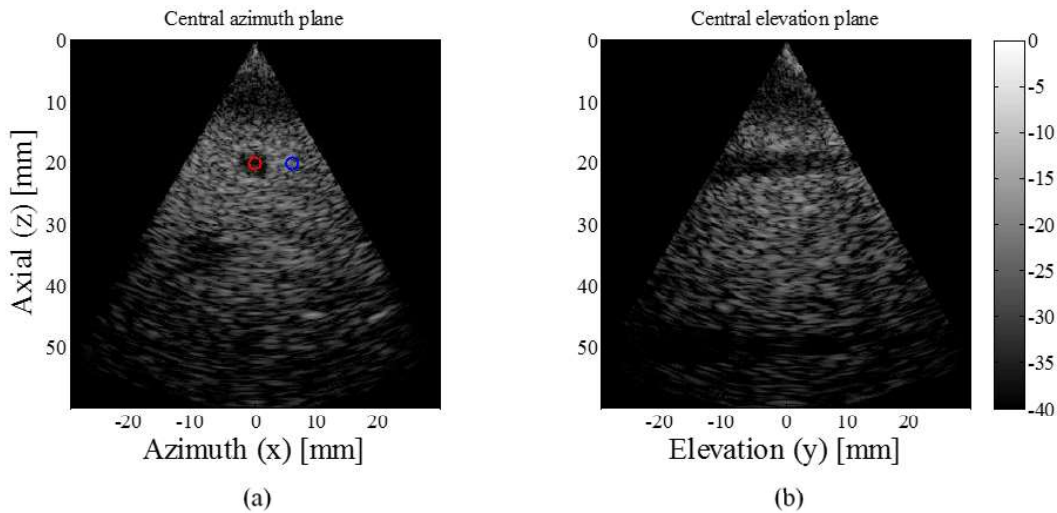


Figure 17: 2D images of the anechoic stepped cylinder, (a) central azimuth plane and (b) central elevation plane

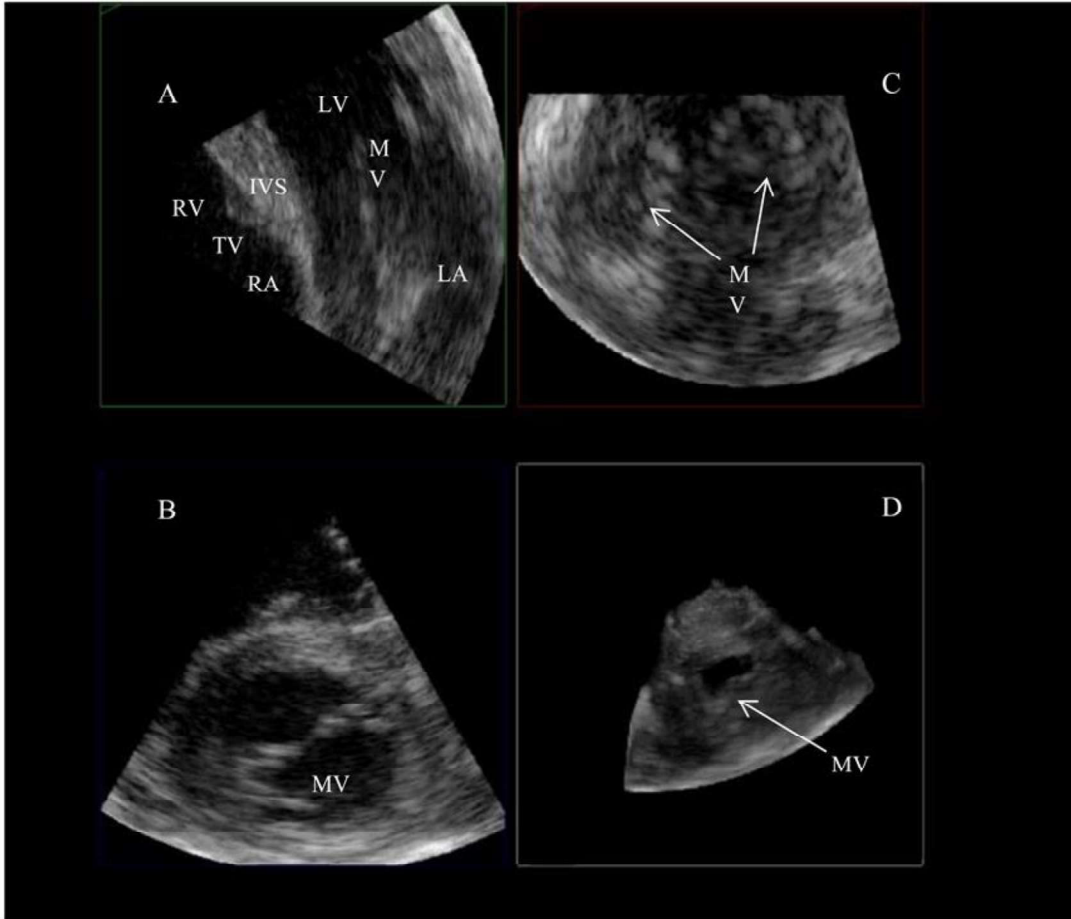


Figure 18: 3D in vivo imaging of the porcine heart. A. azimuth plane, B. elevation plane, C. C-plane sliced to focus on the mitral valve and D. volume rendered image in 2D

7.3.3.4. *In vivo* imaging of the porcine heart

Figure 18 shows three 2D slices and a volume rendered 2D image from the volume reconstructed using the *in vivo* acquisition of the healthy adult pig focused on mitral valve (with the SAX-like view). The reconstructed volume was sliced at specific oblique planes for better visualization of the mitral valve. In this figure, several structures of the heart such as the left atria (LA) and the right atria (RA), the left ventricle (LV) and the right ventricle (RV) are visible along with the interventricular septum (IVS). The tricuspid valve (TV) and the two leaflets of the mitral valve are prominently visible in Figure 18B. For better visualization of the

3D image sequences, two videos are available as multimedia attachments ([Video 1.avi](#) , [Video 2.avi](#)). Both the videos were generated from the 3D acquisition through the diaphragm at a volume rate of 22 Hz during 2-3 heart cycles (2.5 secs). The first video is focused on the mitral valve motion and the second video is focused on the aortic valve motion. These results confirm that with the prototype matrix probe using the proposed 3D beamforming scheme we can produce 3D images

with good image quality at a volume rate of >20 Hz. The acquisition scheme was using 85 tx-rx events per volume, resulting in a minimal volume acquisition time of $85 \times 200 \mu\text{s}$ for a depth of up to 15 cm, which corresponds to a theoretical volume rate of 59 Hz. The achieved acquisition rate of 22 Hz was purely limited by the USB data communication issues of the used data acquisition setup, not by the hardware of the prototype probe.

7.4. Discussion

In this paper, we presented 3D beamforming using a prototype TEE matrix probe featuring a separated transmit-receive aperture and diagonal element dicing. To obtain acceptable image quality at a high volume rate (>20 Hz), a previously introduced 3D parallel beamforming method [17] was extended in this paper to utilize the capabilities of the prototype matrix probe. The proposed 3D beamforming scheme, based on the acoustic characteristics of the probe, was validated using Field II simulations, phantom experiments and an *in vivo* experiment; the results established the capabilities of the prototype matrix transducer and the performance of the proposed 3D beamforming.

The unique architecture of the separated transmit-receive arrays of the prototype matrix probe allows good image quality and high volume rate in combination with a low electric power budget. By separating high-voltage transmit circuitry from the low-voltage receive electronics, it is possible to use low-power, higher-density CMOS technology for the implementation of the ASIC. The split-array architecture also eliminates the need for transmit/receive switches to separate the high voltage transmit signals from the low voltage receive electronics. Moreover, directly wiring out all transmit elements eliminates the need for any transmit electronics in the probe head, which further reduces power dissipation and provides freedom in choosing any complex arbitrary transmit waveforms for transmission. The possible disadvantages of this split-array architecture were proven to be very limited. The limited transmit aperture was able to produce sufficient pressure for adequate imaging. The asymmetric aperture resulted in slightly wider PSFs in elevation direction, but in the *in vivo* tests, this was not noticeable. The eccentric transmit aperture causes a tilt in the elevational PSF and speckle pattern, only observed at shallow depth (< 20 mm). This is not important for diagnostics, and at larger depth, this effect was not at all visible. Thus, it can be concluded that the separated transmitter-receiver design can be advantageous to the transducer characteristics without significant degradation in image quality and speckle pattern beyond depths of a few centimeters.

One aspect of the separated architecture that could be explored further is the possibility of optimizing the transmit array and receive arrays separately for a specific imaging technique. For example, for second harmonic or subharmonic imaging, the center frequency and pitch of the transmit array could be chosen differently from the receive array. This possibility has not yet been explored in this prototype.

The diagonal dicing proves to be very beneficial for the performance. The small rectangular

Chapter 7

transmit aperture produces wide transmit beams with higher sidelobes, especially in elevation direction. A full volume that would be created from only a single pre-steering setting would result in high grating lobe levels. This can be understood by considering the pre-beamformed RF signal of each sub-array as the output of a large, tilted element. Thus, the sub-arrays represent a large effective pitch ($> 2\lambda$) resulting in strong receive grating lobes. In a classical matrix transducer diced parallel to azimuth and elevation directions, these receive grating lobes would be oriented in azimuth and elevation direction. Consequently, the PSFs would severely degrade because of the overlap of these grating lobes with the wide transmit main beams and associated sidelobes. But by dicing the transducer at 45° , the receive grating lobes are positioned at 45° degrees, whereas the transmit sidelobes are still parallel to azimuth and elevation directions (see Figure 12). Thus, diagonal dicing for the prototype probe helps greatly in achieving a good PSF.

The results from the transmit acoustic characterization measurements were in good agreement with the simulated results. However, the measured transmit beam profiles in both azimuth and elevation directions were narrower than the simulation. One possible reason could be a misalignment of the scan plane with respect to the transmitted beam.

Based on the results in the *in vivo* imaging, the transmit efficiency of the prototype probe in terms of producing acoustic pressure is suitable for sufficient depth (~ 90 mm) of penetration. The central frequency of 4.8 MHz with 50% bandwidth is well suited for fundamental cardiac imaging.

To achieve sufficient overlap between the transmit beams, the number of tx-rx events (85, 17×5) for the proposed beamforming scheme was determined using the FWHMs of the transmit beam in azimuth and elevation directions. The FWHM of the measured receive beam profiles in the experiment matched closely with the simulated values. The sub-arrays showed a very uniform directivity pattern. The drop in intensity for pre-steering of the sub-arrays from 0° to 40° was only 3 dB. Thus, the combined directivity pattern of a single sub-array for different pre-steering angles is comparable with the directivity pattern of a single element. The sensitivity variation among the sub-arrays was very low, showing an excellent yield of the transducer manufacturing process.

The proposed 3D beamforming scheme with 85 tx-rx events has shown nice performance in terms of image quality and volume rate for both phantom and *in vivo* experiment. The widths of the PSFs in the phantom experiment were slightly wider than in the simulations. The CNR and CR values in the phantom experiment were lower than in the simulation. The image quality of the simulated volumes differs from the experimental volumes, as in simulation, we use ideal DAS beamforming to produce the best quality volume images. The results confirm the performance of the transducer and the 3D beamforming scheme in terms of the image quality. Due to the rectangular transmit array, the PSFs are asymmetric, they are narrow in azimuth direction and wide in elevation direction. However, it has not introduced any noticeable

artifacts in the 3D images. In the real-time 3D volumes of the *in vivo* experiment, the 3D cardiac structures (chambers and valves) and their motion were clearly visible. These results show the capability of the prototype probe to produce image quality at an adequate volume rate of 22 Hz, making it suitable for real-time 3D imaging.

The 3D images produced by the proposed beamforming scheme have good image quality; the 85-tx-rx events scheme was chosen for good image quality at a sufficiently high frame rate. However, the volume acquisition rate of 22 Hz is lower than what is expected for the 85-tx-rx events scheme (59 Hz). This low volume acquisition rate is only determined by practicalities in the triggering and the communication between the host computer and the probe, which would have been overcome if the probe would have been addressed in its native SPI communication protocol. The probe itself poses no limitations to achieve a 59 Hz full volume acquisition rate for 85 tx-rx events (or higher if depth is limited). Much higher volume rates can be easily achieved by employing broader and lesser transmissions per volume, presumably at the cost of some image quality. In the future, we will explore such high frame rate volumetric imaging for advanced applications such as 3D particle image velocimetry or speckle tracking. Considering the FWHMs ($\sim 30^\circ$) and the intensity profiles of the sub-arrays for different pre-steering, a volume of $90^\circ \times 90^\circ$ can be covered with only 9 tx-rx events. This will improve the volume rate at least by a factor of 9.

7.5. Conclusions

This paper presents 3D beamforming with a prototype volumetric TEE probe. The prototype probe has two key design features. First, it has separated, adjacent transmit and receive arrays with rectangular transmit aperture. Second, it consists of oblique square elements produced by diagonal dicing. The separated arrays, while offering important implementational advantages, did not lead to any noticeable artifacts at larger depth (> 20 mm). The diagonal dicing helped in improving the image quality by separating the diagonal receive grating lobes from the transmit sidelobes in elevation direction. The *in vivo* experiment showed that the prototype matrix probe can produce good quality 3D images with $60^\circ \times 60^\circ$ field of view at a volume rate of 22 Hz using the proposed 3D beamforming scheme with 85 transmit-receive events. The 22 Hz currently is limited by communication overhead, and can, in principle, be increased to 59 Hz with the proposed scheme. Adaptations to this scheme will allow much higher framerates. Hence, this matrix TEE probe with adapted 3D beamforming schemes will open up possibilities for new applications like 3D speckle tracking and particle image velocimetry in the heart.

Acknowledgements

We like to acknowledge M. Baas from Oldelft Ultrasound, Delft, The Netherlands for help with the prototype matrix TEE probe. We also acknowledge H.M.M. van Beusekom, M. te Lintel Hekkert and M. Strachinaru from Erasmus MC, Rotterdam, The Netherlands for their help during the *in vivo* imaging. This work is part of the Open Technology Programme with project

Chapter 7

number 12405 which is (partly) financed by the Netherlands Organisation for Scientific Research (NWO).

References

- [1] B. Khandheria, J. Seward, and A. Tajik, “Transesophageal echocardiography,” *Mayo Clin. Proc.*, vol. 69, no. 9, pp. 856–863, 1994.
- [2] M. D. Cheitlin et al., “ACC/AHA/ASE 2003 guideline update for the clinical application of echocardiography: Summary article,” *J. Am. Soc. Echocardiogr.*, vol. 16, no. 10, pp. 1091–1110, 2003.
- [3] P. M. Kapoor et al., “An update on transesophageal echocardiography views 2016: 2D versus 3D tee views,” *Ann. Card. Anaesth.*, vol. 19, no. Supplement, pp. S56–S72, 2016.
- [4] M. Montealegre-Gallegos, F. Mahmood, K. Owais, P. Hess, J. S. Jainandunsing, and R. Matyal, “Cardiac Output Calculation and Three-Dimensional Echocardiography,” *J. Cardiothorac. Vasc. Anesth.*, vol. 28, no. 3, pp. 547–550, 2014.
- [5] L. H. Frank, A. Chelliah, and C. Sable, “Evaluation of a second-generation microtransesophageal echocardiography transducer and software,” *World J. Pediatr. Congenit. Heart Surg.*, vol. 5, no. 4, pp. 565–70, 2014.
- [6] L. Sugeng et al., “Real-Time Three-Dimensional Transesophageal Echocardiography in Valve Disease: Comparison With Surgical Findings and Evaluation of Prosthetic Valves,” *J. Am. Soc. Echocardiogr.*, vol. 21, no. 12, pp. 1347–1354, 2008.
- [7] I. S. Salgo, “Three-Dimensional Echocardiographic Technology,” *Cardiology Clinics*, vol. 25, no. 2, pp. 231–239, 2007.
- [8] Siemens Healthineers, “ACUSON S3000 TM Ultrasound System,” 2012.
- [9] GE Healthcare, “Vivid TM E9 XDclear TM,” 2013.
- [10] Philips, “X7-2t Live 3D TEE xMATRIX array transducer with PureWave crystal technology.” [Online]. Available: <http://www.usa.philips.com/healthcare/product/HC989605414121/x72t-live-3d-tee-xmatrix-array-transducer-with-purewave-crystal-technology>. [Accessed: 20-Nov-2017].
- [11] S. Blaak, C. T. Lancée, J. G. Bosch, C. Prins, A. F. W. Van Der Steen, and N. De Jong, “A matrix transducer for 3D transesophageal echocardiography with a separate transmit and receive subarray,” in *IEEE Ultrasonics Symposium*, 2011, pp. 2341–

2344.

- [12] Z. Yu, “Low-Power Receive-Electronics for a Miniature 3D Ultrasound Probe,” PhD Thesis, Delft University of Technology, Delft, The Netherlands, 2012.
- [13] D. P. Shattuck, M. D. Weinshenker, S. W. Smith, and O. T. von Ramm, “Explososcan: a parallel processing technique for high speed ultrasound imaging with linear phased arrays,” *J. Acoust. Soc. Am.*, vol. 75, no. 4, pp. 1273–1282, 1984.
- [14] T. Hergum, T. G. Bjåstad, K. Kristoffersen, and H. Torp, “Parallel Beamforming Using Synthetic Transmit Beams,” *IEEE Trans. Ultrason. Ferroelectr. Freq. Control*, vol. 54, no. 2, pp. 271–280, 2007.
- [15] H. Hasegawa and H. Kanai, “High-frame-rate echocardiography using diverging transmit beams and parallel receive beamforming,” *J. Med. Ultrason.*, vol. 38, no. 3, pp. 129–140, 2011.
- [16] L. Tong, A. Ramalli, R. Jasaityte, P. Tortoli, and J. D’Hooge, “Multi-transmit beam forming for fast cardiac imaging-experimental validation and in vivo application,” *IEEE Trans. Med. Imaging*, vol. 33, no. 6, pp. 1205–1219, 2014.
- [17] D. Bera et al., “Three-dimensional beamforming combining micro-beamformed RF datasets,” in *IEEE Ultrasonics Symposium*, 2016, pp. 1–4.
- [18] J. A. Jensen, “Field: A Program for Simulating Ultrasound Systems,” *Med. Biol. Eng. Comput.*, vol. 34, no. 1, pp. 351–353, 1996.
- [19] M. C. Van Wijk and J. M. Thijssen, “Performance testing of medical ultrasound equipment: Fundamental vs. harmonic mode,” *Ultrasonics*, vol. 40, no. 1–8, pp. 585–591, 2002.

Chapter 8

Discussion and Conclusions

Chapter 8

8.1. Discussion

8.1.1. Achievements towards the aim of this thesis

In this thesis, we studied beamforming techniques that offer opportunities for 3D TEE imaging, especially to achieve higher frame rates. The main focus was on 3D beamforming suitable for the prototype miniaturized matrix transducer for pediatric 3D TEE to produce volumes with good image quality at a sufficiently high volume rate (>200 Hz). To solve the challenge of connecting the huge number of elements in matrix transducers to a standard ultrasound system, we first explored the possibilities of receive channel count reduction using dual-stage beamforming techniques. Despite the improved imaging performance of the proposed dual stage beamforming techniques, their use is limited in the case of the targeted miniaturized matrix transducer due to the small aperture size. Hence, 3D parallel beamforming techniques are explored to achieve high frame rate volumetric imaging using the matrix transducers with micro-beamforming capabilities. The techniques have been tested both on the miniaturized matrix transducer as well as on a prototype adult matrix TEE transducer. The experimental results showed that the proposed 3D parallel beamforming technique can produce volumes with acceptable image quality at a volume rate as high as ~ 300 Hz using the prototype miniaturized matrix transducer. Furthermore, the experimental results for the phantom and *in vivo* imaging study using the prototype adult matrix TEE probe indicate that the proposed 3D beamforming technique can be adapted for other matrix probes with micro-beamforming capabilities to produce good quality volume images at a high volume rate, even for a very different layout of the transmit and receive arrays.

8.1.2. Extensions of dual-stage beamforming

One of the major challenges in volumetric imaging with matrix transducers is connecting the huge number of elements to the external ultrasound system. Accordingly, we first explored the possibilities of channel count reduction in 2D imaging using 1D transducers. In Chapter 2 and Chapter 3, we present two dual stage beamforming techniques (PSASB, NDSB) to reduce channel count and RF data transfer rates. The proposed beamforming techniques are significant extensions of the dual-stage beamforming technique as described in [1] for linear array imaging. The proposed PSASB is applicable to the phased array imaging setup and the proposed NDSB is applicable to the linear array imaging setup. These techniques improve the lateral resolution compared to DRF even though only fixed delays (for fixed focusing) or no delays at all are used in the receive front-end. This simplification in the front-end can potentially reduce power budget and silicon area that can instead be used for implementing enriched functionalities, such as digitization, channel multiplexing/de-multiplexing, and signal compression. These functionalities can be very beneficial in the design of a matrix transducer to further reduce channel count and data transfer.

There are three possibilities for extending the proposed 2D dual stage beamforming techniques

to 3D imaging using matrix transducers. First of all, the simplified front-end architecture proposed in Chapter 3 can easily be extended from the 1D transducer to a 2D matrix transducer capable of performing either row- or column-wise summing, without any significant increase in the hardware complexity. This would apply e.g. to the 3D carotid transducer that our group is working on [2], [3]. Accordingly, 3D/4D imaging using a matrix transducer with such a front-end can be performed by applying NDSB in either row-wise or column-wise fashion depending on the possibilities available in the transducer. Secondly, NDSB is also suitable for the existing row-column-addressed matrix transducers [4], [5] where to reduce the channel count the elements are accessed by either their row or column index. In such matrix transducers, NDSB can directly be applied on the summed receive RF signals from the elements in the rows or the columns. Thirdly, PSASB can be applied for volumetric imaging using a matrix transducer with a slightly advanced front-end that is capable of applying fixed 3D focusing and steering. However, it might be challenging to realize a front-end with such 3D focusing functionalities.

Despite these advantages of the dual stage beamforming techniques, there are two main reasons that restrict the application of the proposed techniques in high frame rate volumetric imaging using small matrix transducers such as our 3D micro-TEE. The first reason is that the dual stage beamforming techniques require a large number of transmissions (typically in the order of the number of elements). For achieving high volume rate, however, a low number of transmissions is desired. The second reason is that there is little added benefit in using dual stage beamforming for transducers with small aperture size. In general, dual stage beamforming techniques can produce images with better lateral resolution than DRF. However, this improvement in lateral resolution can be achieved only until the depth of the natural focus of the transducer. Similar to DRF, beyond this depth no focusing can be achieved using these techniques. As a consequence, we have not studied any further extensions of dual stage beamforming for high frame rate volumetric imaging using our prototype miniaturized matrix transducer.

Finally, apart from the possibilities of these techniques for matrix arrays, the reduced data transfer rate enables the design of ultrasound transducers similar to [6] that can wirelessly transfer the beamformed receive RF data to a low-cost portable or handheld ultrasound system. Thus, the dual stage beamforming techniques can bring ultrasound diagnostic technology to remote or low-income regions, which can be beneficial especially for developing countries. Moreover, such portable ultrasound systems can be very useful in diagnostic imaging at the point of care in an ambulatory practice.

8.1.3. Design and acoustic characterization of the pediatric matrix TEE transducer

The relatively large probe heads ($\sim 10\text{ cm}^3$) of the present 3D TEE probes are not suitable for pediatric use and cannot be tolerated by adult patients during long-term procedures without a

Chapter 8

full anaesthesia. Until now, no matrix transducer has been designed for 3D TEE in pediatric patients. We have designed a matrix TEE transducer with dimensions similar to the μ TEE probe [7] can be used both as a pediatric 3D TEE probe as well as a transnasal adult 3D TEE probe for long-term monitoring.. In Chapter 4, we describe the design of a low-power, area-efficient front-end ASIC with integrated 32×32 elements PZT matrix transducer suitable for this pediatric 3D TEE. Apart from the micro-beamforming circuitry for channel reduction, the application-specific integrated circuit (ASIC) is also equipped with low-power low-noise amplifier (LNA), programmable-gain amplifiers (PGA) and a mismatch scrambler to improve the signal quality of the received RF signals.

The acoustic characterization of the designed prototype transducer is described in Chapter 5. From the measured transmit central frequency, the transmit efficiency, and the minimum detectable receive pressure it can be concluded that the prototype transducer can image up to a depth (~ 120 mm) sufficient for pediatric TEE. The experimental results confirm that the prototype miniaturized transducer can pre-steer reception in 25 fixed directions. The wide opening angle of the transmit beam ($\sim 20^\circ \times 20^\circ$) from the small transmit array and the receive beams ($\sim 40^\circ \times 40^\circ$) from individual sub-arrays together allow beamforming of many 3D scanlines from each tx-rx event. As a result, a volume with $90^\circ \times 90^\circ$ viewing angle can be covered by only 25 tx-rx events including overlaps between consecutive tx-rx events. Thus, the characteristics of the prototype transducer match the requirements for multiline 3D parallel beamforming techniques.

Although the prototype miniaturized transducer matches the required functionalities for high volume rate 3D TEE imaging, there are several limitations that could be addressed in future designs. The first limitation is the small central transmit array of the prototype transducer that restricts the generated transmit pressure, and hence, limits the depth of imaging/SNR. As the transmit voltage will be limited to a certain level, to produce higher transmit pressures, a larger transmit array would be desirable. Moreover, due to the split-array architecture and the specific layout of the prototype transducer, the central transmit array creates a receive aperture with a square hole in the center. This receive aperture causes increased side lobe levels (by ~ 2 dB) in the receive beamprofile compared to a full receive aperture. One obvious solution to these two limitations would be to use the entire aperture of the prototype matrix transducer in both transmit and receive. However, to control the larger number of transmit elements, an on-chip transmit beamformer will be needed, which might increase the size, power and cost of the ASIC. Obviously, such a change is not possible without a radical redesign of the ASIC. Careful design choices are necessary for such redesign to keep the area and power requirements within the desired limit.

The second limitation of the ASIC is the gain step of 6 dB for the discrete gain settings in the PGA (TGC/LNA). These 6 dB discrete changes in gain will cause abrupt intensity changes in the receive signals over depth that need to be compensated in the final reconstructed volume

image. In general, to produce a smooth image, a smooth transition in gain settings (continuous, or with steps of 0.2-0.3 dB) is desired. Therefore, it would be interesting to study possible improvements to the PGA design without exceeding the area and power budget.

The third limitation in the present design is the limited number of pre-steering angles (5 in azimuth and elevation) caused by the fixed number of delay steps. Employing delay lines with finer delay steps will enable the receive array to pre-steer in intermediate directions, and will increase the flexibility in designing 3D beamforming techniques suitable for the prototype transducer. However, the current delay line design requires a sample-and-hold capacitor for each step, which is rather chip area intensive, so it is not straightforward to change the number of delay steps.

Finally, the prototype transducer (in its present form) is still only suitable for performing *in vitro* imaging, since it is mounted on a big PCB in a bulky casing. To show the real-time imaging capability in an *in vivo* scenario, the prototype transducer has to be mounted in a gastroscopic tube. This requires further design optimization, especially considering the challenging interconnection to cable assemblies that fit a gastroscopic tube.

8.1.4. Multiline 3D parallel beamforming

In Chapter 6, we study 3D multiline parallel beamforming techniques suitable for the designed prototype miniature matrix transducer. None of the existing parallel beamforming techniques [8]–[11] was directly applicable to the prototype transducer because of the small aperture size, the split-array architecture and the layout of transmit and receive arrays. Therefore, in this chapter, we propose four beamforming schemes. The first scheme utilizes only 25 transmit-receive (tx-rx) events ($\mu\text{BF}25$) to produce volumes with good image quality at a high volume rate (~ 300 Hz) and the second scheme requires 169 ($\mu\text{BF}169$) tx-rx events to produce volumes with slightly better image quality at the cost of a reduced volume rate (~ 44 Hz). In the third and the fourth schemes, to achieve higher frame rate than the first scheme only 9 ($\mu\text{BF}9n$ and $\mu\text{BF}9w$) tx-rx events are used. All the proposed schemes create many image lines within a sub-volume from one transmit-receive event. They avoid the image artifact of sharp boundaries in the final volume by an angle-weighted linear combination of corresponding scanlines in the overlapping sub-volumes. Because of the higher heart rate in pediatric patients (80-150 BPM), volumetric cardiac imaging on them requires a higher frame rate than on adults. Although the proposed $\mu\text{BF}9$ schemes can produce images at a high volume rate, they are not suitable for producing B-mode images with acceptable image quality. Volume reconstruction using $\mu\text{BF}169$ is suitable for producing improved image quality at a volume rate sufficient for real-time B-mode volumetric imaging on pediatric patients. On the other hand, volume reconstruction using $\mu\text{BF}25$ is suitable for applications such as 3D Tissue Doppler Imaging, 3D speckle and flow tracking in pediatric patients where high volume rate is essential. The proposed volumetric imaging methods with micro-beamforming (for pre-steering only in the fixed 25 directions) show only a minor degradation in image quality in simulations compared

Chapter 8

to conventional single line acquisition using an ideal fully sampled matrix transducer. The experimental results of the point scatterer phantom validate the 3D imaging capability of the prototype transducer using the proposed 3D beamforming techniques.

Despite the advantages of the proposed beamforming schemes, there is still room for improvement. The simulation results for the lateral shift invariance test showed intensity drops in the regions between the pre-steering angles, as is expected from the combined transmit-receive beamprofile. Although the proposed intensity compensation works nicely to achieve a uniform intensity distribution, it lowers the SNR in the intermediate non-pre-steered regions. An alternative way to reduce the intensity drops is to transmit broader beams or to do additional transmits in the intermediate directions. However, the receive sensitivity will be anyway lower in those directions, due to the limited pre-steering capabilities of the ASIC of the prototype transducer. In Chapter 6, we have studied a few intuitive transmit-receive schemes for producing 3D images at a high volume rate and have studied their quality. However, it has not yet been investigated how the transmit-receive (tx-rx) scheme parameters can be optimized to achieve the best trade-offs between volume rate and image quality. A different pattern of transmit beams can change the volume rate and a better overlap between the transmit beams and the pre-steered receive beams may further improve the image quality. Therefore, the effects of transmit beam distributions, transmit beam opening angles, and the different weighting functions for combining the sub-volumes should be further studied.

8.1.5. Extension of the proposed multiline 3D parallel beamforming

To show the applicability of multiline 3D beamforming technique as proposed in Chapter 6, Chapter 7 describes an extension of the 3D beamforming technique to perform volumetric imaging with a different prototype matrix TEE probe, which was designed by Oldelft Ultrasound [12]. This prototype matrix probe for adult TEE imaging has two unique features: diagonal element dicing and separated transmit and receive arrays, with a small rectangular transmit aperture next to a square receive aperture. The diagonal dicing together with the separated transmit and receive array helps in reducing the overlap between the prominent receive grating lobes with the transmit main, side and grating lobes. Similar to the prototype miniaturized matrix transducer, the 128 transmit elements are directly wired out to an external ultrasound system. The receive ASIC supports micro-beamforming capabilities for sub-arrays of 4×4 elements to reduce the channel count. The sub-arrays can be pre-steered to any angle in the 3D hemisphere. The prototype is realized as a fully functional device, mounted in a standard gastroscopic tube with a manipulation handle.

The acoustic characterization measurements of the small rectangular transmit array show that the central frequency and transmit pressure are very suitable for TEE imaging. The rectangular transmit array produces an asymmetric transmit beam that is narrow in lateral direction and wide in elevation direction. The square receive aperture produces symmetric receive beams. The wide transmit beam and large opening angle of the receive beams from the sub-arrays

make this prototype probe suitable for the proposed multiline 3D beamforming scheme.

Based on the FWHM of the transmit and receive beams, and to achieve sufficient overlap between the transmit beams, the proposed beamforming technique for the prototype matrix probe uses 85 (17×5) tx-rx events to reconstruct a volume with a field of view of $60^\circ \times 60^\circ$ with 121×121 lines. The prototype matrix probe produces good quality volume images in an *in vivo* imaging experiment on a porcine heart using the proposed 3D beamforming scheme. The reconstructed volume images clearly show the 3D cardiac structures (chambers and valves) and their motions.

Although the 3D images produced by the prototype TEE probe are of good quality, they exhibit two effects linked to the specific layout of the transmit and receive arrays. The split-array architecture of the prototype matrix probe causes misaligned transmit and receive beams close to the transducer. Due to this misalignment, the prototype matrix probe produces tilted PSFs and speckle patterns at a shallower depth (< 20 mm). However, at larger depth, this effect is hardly noticeable. The rectangular transmit array produces asymmetric transmit beams that are wider in elevation direction than in azimuth direction. The square receive array produces symmetric receive beams, and therefore, the resultant pulse-echo PSFs are asymmetric and lateral resolution in azimuth direction is slightly better than in elevation direction. Despite the presence of these two unavoidable effects, the cardiac structures and their motions were clearly recognizable in the *in vivo* volume images. Thereby, it can be concluded that the effects related to the transducer layout do not deteriorate the interpretability of the produced volume images.

Further investigation is needed to increase the volume rate for the 3D imaging using the prototype matrix probe. The present volume acquisition rate (22 Hz) does not reach the intended rate of the 3D beamforming tx-rx scheme, but it is limited by the slow USB communication between the host PC and the interface box. With 85 tx-rx events and an acquisition time of $200 \mu\text{s}$ per tx-rx event, a volume acquisition rate of ~ 60 Hz could easily be achieved. However, for advanced applications such as 3D flow or speckle tracking for a much higher volume rate is desirable. Thereby, it will be interesting to explore volume reconstruction using a lesser number of tx-rx events by using transmit beams that are wide in both azimuth and elevation directions. A volume imaging scheme with lesser tx-rx events will, of course, sacrifice some image quality in terms of SNR and PSF.

8.2. Conclusions

This thesis presents beamforming techniques suitable for 3D TEE imaging, especially to achieve higher frame rates ($> 80\text{Hz}$). The proposed Phased array Synthetic Aperture Sequential Beamforming can improve the lateral resolution compared to conventional DRF without transferring the raw channel data (Chapter 2). The proposed Non Delayed Sequential Beamforming provides, in general, a better lateral resolution than conventional DRF, even with simplified front-end electronics (Chapter 3). However, both synthetic aperture beamforming

Chapter 8

techniques are not directly suitable for high frame rate 3D imaging. To enable pediatric 3D TEE, a miniaturized matrix transducer containing a highly compact and power-efficient ASIC with micro-beamforming is designed (Chapter 4). The designed prototype matrix transducer shows sufficient transmit efficiency, receive dynamic range, transmit steering capability and receive pre-steering capability required for high frame rate 3D TEE imaging (Chapter 5). The proposed 3D multiline parallel beamforming schemes suitable for the designed prototype miniaturized matrix transducer are capable of producing volume images with good image quality by avoiding artifacts introduced by parallel beamforming at a volume rate >40 Hz (Chapter 6). The extension of the 3D multiline beamforming scheme proposed in Chapter 6, adapted for the prototype adult matrix TEE probe produces real-time *in vivo* volume images with good image quality at an acceptable volume rate of 22 Hz (theoretically 60 Hz), despite the separated transmit and receive array with small rectangular transmit aperture (Chapter 7). The proposed 3D beamforming schemes can easily be adapted for matrix probes with micro-beamforming capabilities to produce good quality volume images at a high volume rate, even for a very different layout of the transmit and receive arrays.

References

- [1] J. Kortbek, J. A. Jensen, and K. L. Gammelmark, "Sequential beamforming for synthetic aperture imaging," *Ultrasonics*, vol. 53, no. 1, pp. 1–16, 2013.
- [2] E. Kang, Q. Ding, M. Shabanimotlagh, P. Kruizinga, Z. Y. Chang, and E. Niothout, "A Reconfigurable 24×40 Element Transceiver ASIC for Compact 3D Medical Ultrasound Probes," pp. 211–214, 2017.
- [3] P. Kruizinga, E. Kang, M. Shabanimotlagh, Q. Ding, E. Niothout, and Z. Yao, "Towards 3D ultrasound imaging of the carotid artery using a programmable and tileable matrix array," in *IEEE Ultrasonics Symposium*, 2017, pp. 1-3,.doi: 10.1109/ULTSYM.2017.8091570.
- [4] T. L. Christiansen, M. F. Rasmussen, J. P. Bagge, L. N. Moesner, J. A. Jensen, and E. V. Thomsen, "3-D imaging using row-column-addressed arrays with integrated apodization-part ii: Transducer fabrication and experimental results," *IEEE Trans. Ultrason. Ferroelectr. Freq. Control*, vol. 62, no. 5, pp. 959–971, 2015.
- [5] K. Chen, H. S. Lee, and C. G. Sodini, "A Column-Row-Parallel ASIC Architecture for 3-D Portable Medical Ultrasonic Imaging," *IEEE J. Solid-State Circuits*, vol. 51, no. 3, pp. 738–751, 2016.
- [6] M. C. Hemmsen *et al.*, "Implementation of synthetic aperture imaging on a hand-held device," in *IEEE Ultrasonics Symposium*, 2014, pp. 2177–2180.
- [7] Oldelft Ultrasound, "MicroMulti TEE probe." [Online]. Available:

<http://www.oldelft.nl/products/multimicro-tee-probe/item18>. [Accessed: 04-Oct-2017].

- [8] T. Hergum, T. G. Bjåstad, K. Kristoffersen, and H. Torp, "Parallel Beamforming Using Synthetic Transmit Beams," *IEEE Trans. Ultrason. Ferroelectr. Freq. Control*, vol. 54, no. 2, pp. 271–280, 2007.
- [9] L. Tong, A. Ramalli, R. Jasaityte, P. Tortoli, and J. D'Hooge, "Multi-Transmit Beam Forming for Fast Cardiac Imaging — Experimental Validation and In Vivo Application," vol. 33, no. 6, pp. 1205–1219, 2014.
- [10] H. Hasegawa and H. Kanai, "High-frame-rate echocardiography using diverging transmit beams and parallel receive beamforming," *J. Med. Ultrason.*, vol. 38, no. 3, pp. 129–140, 2011.
- [11] P. Santos, G. Haugen, L. Løvstakken, E. Samset, and J. D'hooge, "Diverging Wave Volumetric Imaging Using Subaperture Beamforming," *Ultrason. Ferroelectr. Freq. Control. IEEE Trans.*, vol. 63, no. 12, pp. 2114–2124, 2016.
- [12] Z. Yu, "Low-Power Receive-Electronics for a Miniature 3D Ultrasound Probe," PhD Thesis, Delft University of Technology, Delft, The Netherlands, 2012.

Summary

In this thesis, we study beamforming techniques that offer opportunities for 3D transesophageal echocardiography (TEE) imaging, especially to achieve higher frame rates. A number of matrix transducers are already available in the market for performing 3D TEE in adults; however, they are not suitable for pediatric patients. In 3D TEE with a matrix transducer, two main challenges are to connect a large number of elements to a standard ultrasound system and to achieve a high volume rate (>200 Hz).

To reduce the channel count in 1D array transducers, dual-stage beamforming solutions are proposed in Chapter 2 and Chapter 3. In Chapter 2, we apply dual-stage beamforming in phased array imaging. The primary advantage of using dual-stage beamforming is achieving an improved lateral resolution without storing the raw channel data, which can be realized on ultrasound systems with a relatively simple front-end. The proposed dual-stage beamforming for phased array imaging significantly outperforms the conventional DRF in improving the lateral resolution. In Chapter 3, we develop a dual-stage beamforming technique for linear array imaging which is able to produce images from scanlines that are produced with focused transmit, and simple summation in receive (no delays). The proposed dual-stage beamforming is useful for miniaturized linear/matrix array and/or wireless systems with a large number of elements and simple front-end electronics. The quality of the image is comparable to conventional imaging which uses e.g. dynamic receive focusing.

To fulfil the unmet need of a pediatric matrix transducer, in Chapter 4, we present the design of a front-end ASIC for a miniaturized matrix transducer suitable for real-time 3D TEE. The ASIC uses micro-beamforming to reduce the receive channel count. The front-end ASIC is designed with a compact form factor and a low power budget to satisfy the requirements of a pediatric TEE probe as well as a transnasal adult probe for long-term monitoring. In Chapter 5, we describe the acoustic design, fabrication and characteristics of a prototype 3D TEE transducer built on the designed ASIC. The combined transmit-receive beams are successfully steered to the 25 pre-defined angles in 3D space. The wide opening angle of the transmit beams and the receive beams from individual sub-arrays together allow beamforming of many 3D scanlines from each transmit-receive event.

Despite the improved imaging performance of the proposed dual-stage beamforming techniques, their use is limited in the case of transducers with small aperture size. Hence, in Chapter 6, we propose 3D parallel beamforming schemes to perform high frame rate volumetric imaging with improved image quality using matrix transducers having micro-beamforming capabilities. In the proposed 3D beamforming, the image quality of the produced volumes is enhanced by suppressing the crossover artifacts that are typical for parallel-beamforming. To suppress these crossover artifacts an angle-weighted combination of overlapping sub-volumes is used. The proposed schemes are tested both on the miniaturized matrix transducer in

Summary

Chapter 6 as well as on a prototype adult matrix TEE transducer in Chapter 7. The experimental results show that the proposed 3D parallel beamforming scheme using the prototype miniaturized matrix transducer can produce images at a sufficiently high volume rate (~ 300 Hz) with an acceptable image quality. In Chapter 7, we perform an *in vivo* imaging study using a prototype adult matrix TEE probe with diagonally diced elements and separated transmit and receive arrays. The results indicate that to produce good quality volume images at a high volume rate the proposed 3D beamforming scheme can be easily adapted for other matrix probes with micro-beamforming capabilities, even for a very different layout of the transmit and receive arrays.

In the final chapter, we discuss the overall findings, challenges and scopes for future research. The beamforming techniques presented in the thesis are focused towards transesophageal echocardiography imaging. We believe that these techniques may contribute to a better diagnosis and treatment of patients with cardiac problems.

Samenvatting

In dit proefschrift bestuderen we technieken voor bundelvorming ten behoeve van driedimensionale (3D) transoesofagale echocardiografie (TEE), in het bijzonder voor het bereiken van een hogere beeldsnelheid. Er is al een aantal matrixtransducers op de markt voor 3D TEE in volwassenen, maar deze transducers zijn niet geschikt voor pediatrische patiënten. In 3D TEE met een matrixtransducer zijn er twee belangrijke uitdagingen: het aansluiten van het grote aantal elementen op een standaard-ultrageluidssysteem, en het bereiken van een hoge beeldsnelheid (>200 beeldvolumes per seconde).

Om het aantal kanalen van 1D-arraytransducers te beperken, stellen we in Hoofdstuk 2 en 3 tweetraps-bundelvormingstechnieken voor. In hoofdstuk 2 passen we een dergelijke tweetrapsstechniek toe in *phased array imaging*. Het belangrijkste voordeel hiervan is een betere laterale resolutie, zonder dat de onbewerkte data per kanaal opgeslagen hoeft te worden. Dit maakt deze techniek geschikt voor standaard echosystemen met relatief eenvoudige ingangscircuits (*front-ends*). De voorgestelde tweetraps-bundelvorming voor *phased array imaging* levert een significant betere laterale resolutie dan de conventionele *Dynamic Receive Focusing*. In Hoofdstuk 3 ontwikkelen we een tweetraps-techniek voor beeldvorming met lineaire arrays. Deze kan beelden vormen uit scanlijnen die zijn geproduceerd met een gefocusseerde transmissie en een ontvangst waarbij de elementsignalen simpelweg worden gesommeerd, zonder onderlinge vertraging. Deze techniek is geschikt voor miniatuurtransducers (lineair dan wel matrix) en/of draadloze systemen met grote aantallen elementen en simpele *front-end* circuits. De beeldkwaliteit is vergelijkbaar met die van een conventionele aanpak, zoals *Dynamic Receive Focusing*.

Om in de behoefte aan pediatrische 3D TEE te voorzien, presenteren wij in Hoofdstuk 4 het ontwerp van een *front-end* geïntegreerd circuit (*ASIC* oftewel *Application Specific Integrated Circuit*) voor een miniatuur-matrixtransducer voor *real-time* 3D TEE. De ASIC gebruikt micro-bundelvorming om het aantal ontvangstkanalen te beperken. De ASIC heeft een zodanig laag vermogen en kleine afmeting dat hij geschikt is zowel voor een pediatrische TEE probe als voor een transnasale probe voor volwassenen, ten behoeve van patiëntbewaking gedurende langere tijd. In Hoofdstuk 5 beschrijven we het akoestisch ontwerp, de assemblage en de gemeten eigenschappen van een 3D TEE-transducerprototype (micro-3D) dat is gebouwd op basis van de ontworpen ASIC. De door uitzending en ontvangst gevormde bundels kunnen volgens plan in de 25 gekozen ruimtelijke richtingen worden gestuurd. De grote openingshoek van de uitgezonden bundels en de ontvangen bundels van individuele sub-arrays maken het construeren van een groot aantal 3D beeldlijnen mogelijk voor elke zend-ontvangstcyclus.

De voorgestelde tweetraps-beeldvormingstechnieken leveren weliswaar betere beeldkwaliteit, maar ze zijn minder geschikt voor transducers met een kleine apertuur. Daarom stellen we in

Hoofdstuk 6 technieken voor die meerdere bundels tegelijk kunnen genereren (parallelle-

Samenvatting

bundelvorming). Voor een matrixtransducer met micro-bundelvorming kunnen deze technieken volumetrische (3D) beelden met een hoge beeldsnelheid en een betere beeldkwaliteit leveren. De beeldkwaliteit van de geproduceerde volumes wordt verbeterd door de onderdrukking van de *crossover* artefacten die typisch zijn voor parallelle-bundelvorming. Hiertoe wordt een gewogen combinatie van lijnen uit overlappende subvolumes gemaakt, met een weging op basis van de stuurhoek van de bundel. Deze technieken zijn getest zowel op de micro-3D TEE (Hoofdstuk 6) als op een prototype van een matrix TEE transducer voor volwassenen (Hoofdstuk 7). De resultaten uit experimenten laten zien dat de voorgestelde 3D parallelle-bundelvorming op het micro-3D prototype 3D beelden van acceptabele kwaliteit produceert met voldoende hoge beeldsnelheid (~ 300 Hz). In Hoofdstuk 7 voeren we een *in-vivo*-studie uit met een prototype van een matrix TEE voor volwassenen met diagonaal gezaagde elementen en een gescheiden zend- en ontvangstarray. De resultaten laten zien dat de voorgestelde 3D-bundelvorming eenvoudig kan worden aangepast voor een andere matrixprobe met micro-bundelvorming, zelfs voor een geheel andere verdeling van zend- en ontvangstelementen, en dan 3D beelden van goede kwaliteit met een hoge beeldsnelheid levert.

In het laatste hoofdstuk bespreken we de algemene bevindingen, uitdagingen en nog uit te voeren onderzoek. De technieken voor bundelvorming die we in dit hoofdstuk presenteren zijn gericht op transoesofagale echocardiografie. We zijn van mening dat deze technieken kunnen bijdragen aan een betere diagnose en behandeling van hartpatiënten.

Publications

Submitted papers

1. **D. Bera**, F. van den Adel, N. Radeljic-Jakic, B. Lippe, M. Soozande, M.A.P. Pertijs, M. Verweij, P. Kruizinga, V. Daeichin, H.J. Vos, A.F.W. van der Steen, J.G. Bosch, N. de Jong, “Fast volumetric imaging using a matrix TEE probe with partitioned transmit-receive array,” *Ultrasound in Medicine & Biology*. Forthcoming 2018.
2. V. Daeichin, **D. Bera**, S.B. Raghunathan, M. ShabaniMotlagh, Z. Chen, C. Chen, E. Noothout, H.J. Vos, M.A.P. Pertijs, J.G. Bosch, N. de Jong, M. Verweij, “Acoustic characterization of a miniature matrix transducer for pediatric 3D transesophageal echocardiography,” Manuscript submitted for publication, 2018.
3. C. Chen, Z. Chen, **D. Bera**, E. Noothout, Z.-Y. Chang, M. Tan, H.J. Vos, J.G. Bosch, M.D. Verweij, N. de Jong, M.A.P. Pertijs, “A Pitch-Matched Front-End ASIC with Integrated Subarray Beamforming ADC for Miniature 3-D Ultrasound Probes,” Manuscript submitted for publication, 2018.

Peer-reviewed papers

1. **D. Bera**, S.B. Raghunathan, H.J. Vos, C. Chen, Z. Chen, M.A.P. Pertijs, M.D. Verweij, N. De Jong, J.G. Bosch, “Multiline 3D beamforming using micro-beamformed dataset for pediatric transesophageal echocardiography,” *Phys. Med. Biol.*, vol. 63, no. 7, pp. 075015, 2018, DOI: 10.1088/1361-6560/aab45e.
2. **D. Bera**, J.G. Bosch, M.D. Verweij, N. de Jong, H.J. Vos, “Dual stage beamforming in the absence of front-end receive focusing,” *Phys. Med. Biol.*, vol. 62, no. 16, pp. 6631–6648, 2017.
3. C. Chen, Z. Chen, **D. Bera**, S.B. Raghunathan, M. Shabanimotlagh, E. Noothout, Z.-Y. Chang, J. Ponte, C. Prins, H.J. Vos, J.G. Bosch, M.D. Verweij, N. de Jong, M.A.P. Pertijs, “A Front-End ASIC With Receive Sub-array Beamforming Integrated With a 32 x 32 PZT Matrix Transducer for 3-D Transesophageal Echocardiography,” *IEEE J. Solid-State Circuits*, vol. 63, no. 1, pp. 1–13, 2017.
4. T. van Rooij, I. Skachkov, I. Beekers, K.R. Lattwein, J.D. Voorneveld, T.J. Kokhuis, **D. Bera**, Y. Luan, A.F. van der Steen, N. de Jong, K. Kooiman, “Viability of endothelial cells after ultrasound-mediated sonoporation: Influence of targeting, oscillation, and displacement of microbubbles,” *J. Control. Release*, vol. 238, pp. 197–211, 2016.

Conference proceedings

5. S.B. Raghunathan, **D. Bera**, C. Chen, S. Blaak, C. Prins, M.A.P. Pertijs, J.G. Bosch, N. De Jong, M.D. Verweij, “Design of a miniature ultrasound probe for 3D transesophageal echocardiography,” in *IEEE Ultrasonics Symposium*, 2014: pp. 2091–2094. doi:10.1109/ULTSYM.2014.0521.
6. **D. Bera**, J.G. Bosch, N. de Jong, H.J. Vos, “Synthetic Aperture Sequential Beamforming for phased array imaging,” in *IEEE Ultrasonics Symposium*, 2015: pp. 1–4. doi:10.1109/ULTSYM.2015.0499.
7. C. Chen, Z. Chen, **D. Bera**, S.B. Raghunathan, M. Shabanimotlagh, E. Noothout, Z.Y. Chang, J. Ponte, C. Prins, H.J. Vos, J.G. Bosch, M.D. Verweij, N. De Jong, M.A.P. Pertijs, “A Front-end ASIC with Receive Sub-Array Beamforming Integrated with a 32×32 PZT Matrix Transducer for 3-D Transesophageal Echocardiography,” in *2016 Symposia on VLSI Technology and Circuits*, 2016, vol. 63, no. 1, pp. 38–39.
8. **D. Bera**, H.J. Vos, S.B. Raghunathan, C. Chen, Z. Chen, M.D. Verweij, M.A.P. Pertijs, N. de Jong, J.G. Bosch, “Three-dimensional beamforming combining micro-beamformed RF datasets,” in *IEEE Ultrasonics Symposium*, 2016: pp. 1–4. doi:10.1109/ULTSYM.2016.7728449.
9. J.D. Voorneveld, **D. Bera**, A.F.W. van der Steen, N. de Jong, J.G. Bosch, “Particle image velocimetry on simulated 3D ultrafast ultrasound from pediatric matrix TEE transducers,” in *Proc. SPIE, Medical Imaging*, 2017, vol. 10139, pp. 1–9, doi:10.1117/12.2254436.
10. C. Chen, Z. Chen, **D. Bera**, E. Noothout, Z.Y. Chang, H. Vos, J. Bosch, M. Verweij, N. de Jong, M.A.P. Pertijs, “A front-end ASIC for miniature 3-D ultrasound probes with in-probe receive digitization,” in *IEEE Ultrasonics Symposium*, 2017. doi:10.1109/ULTSYM.2017.8091913.

Curriculum Vitae



Deep Bera was born in Kolkata, India on 19th April 1984. After finishing his secondary and higher secondary education at Hindu School, Kolkata, in 2002 he started with the undergraduate program of Computer Science and Engineering at Kalyani Government Engineering College, India. He received his B.Tech. degree from West Bengal University of Technology, Kolkata, in 2006. After that, he worked as a software consultant in Wipro Technologies, India until 2007. In 2007, he started with the master program in Electrical and Electronics Communication Engineering at Indian Institute of Technology, Kharagpur. He received his M.S. degree in 2011 for the thesis on “Implementation of Digital Scan Conversion and Speckle Reduction Imaging units in DSP for Ultrasound System”. During his masters, in December 2008, Deep married Aditi Mandal. He has served in Samsung Advanced Institute of Technology (2010-2012) and Philips Research (2012-2013) as a Scientist. In both Samsung South Korea and India, he worked on machine learning and real-time biomedical signal processing on physiological signals. In Philips, he was involved in research related to clinical decision support systems and risk prediction modelling for cardiovascular disease in the Chinese population.

In 2013, Deep joined the Biomedical Engineering Department of Thoraxcenter at Erasmus Medical Centre in Rotterdam as a PhD student under dr. ir. J.G. Bosch, dr. ir. H.J. Vos, Prof. dr. ir. N. de Jong and Prof. dr. ir. A.F.W. van der Steen. During his PhD, he was focused on 2D/3D beamforming for medical ultrasound, especially for transesophageal echocardiography (TEE). Since November 2017 he is working as a Senior Scientist at Philips Research, Bangalore, India on Ultrasound Elastography.

Acknowledgment

First and foremost, I would like to thank my eternal supporter, my late grandfather Rash Behari Bera: I owe it all to you. I miss your interesting and courageous stories of the independence war of India. I hope I can follow your ideology, inspiration, and motivation throughout my entire life. In 2013, right after my departure to the Netherlands, I lost my grandmother: Kamala Bera. She was always keen to know where was I and what I was doing and how I was proceeding, although it is likely that she had never realized what it was all about! I will miss your complaints and momentous presence and most importantly your general impudence.

I am grateful to my wife and son: Aditi and Rishaan and my other family members and friends who have always provided moral and emotional support to me from a distance. A special thanks to Aditi especially for her immense contributions to my family in the last four years. At times when I was busy with everything other than the family, Aditi was silently raising Rishaan and passing through sleepless nights. I owe a lot to Aditi for all her help and sacrifices towards my success.

This thesis represents not only my work in front of the inanimate objects like oscilloscopes, water tanks, monitors, and keyboards, but also a milestone in more than one decade of work performed by various researchers at the Department of Biomedical Engineering, Thoraxcenter in ErasmusMC. My experience at the department has been extraordinarily fulfilling. Since my first day on October 17th, 2013 I have felt at home here. The results presented in this thesis were achieved by the joint effort of dozens of people, whom I wish to thank. But this thesis is also the result of many experiences I have encountered at ErasmusMC and all over the world from many remarkable individuals whom I also wish to acknowledge.

I want to thank my supervisors: Hans and Rik. They have been supportive since the days I began playing with the hydrophone and transducers without knowing much about them. They taught me the best practices of performing research in experimental physics. Their criticism, involvement, and ideas to make my Ph.D. experience productive and stimulating are unmatched. Their advice on both research as well as on my career have been priceless. I received all the support from them both academically and emotionally through the rough road to finish this thesis. They helped me to be well equipped and guided me over the last four years of development. Hans deserves a special thanks especially for giving me the moral support and the freedom I needed to move on during the most difficult times when writing this thesis.

My heartiest thanks goes to Nico and Ton for being my promoters and guiding me through all these years. Nico taught me many concepts of acoustics and most importantly the four governing equations that I am going to use forever. Nico had always been supportive throughout the last four years whenever I was in need of help. He deserves a big thanks especially for listening to all my complaints and dealing with my stubbornness. In most of the

Acknowledgment

cases, I calmed down after a discussion with Nico, which helped me to continue again. I admire Ton's contribution towards maintaining an impressive international work environment in the department. A special thanks to Ton for sponsoring the table tennis table for the department. I really hope that future students make a good use of the table.

During the last four years, I have also worked in TU Delft for a significant portion of the time. Among all the people I met in TU Delft, Shreyas and Maysam deserve their own share of acknowledgment. Shreyas has played the role of my acoustic-guru when I joined the MICA project. He paved the path which I later followed and attained success. I would like to share a special thanks to Shreyas for all the intense time we spent together both inside the lab and at the bar. Although I was not in the same project with Maysam, I never felt it. We always discussed and shared our problems and opinions as if we are solving a greater problem. Chao and Zhao from TU Delft also have a huge contribution towards the success of my work. Additionally, they have been always supportive and available whenever it was in need. I would also like to thank Martin and Michiel for their help in the MICA project and especially for their comments on our manuscripts.

Robert, Gerard, and Frits are the main pillars of our side of the BME. Robert is an extraordinary personality to discuss music, politics, history, emotions and what not. Robert always amazed me with his sheer common sense. I am happy that we have spent plenty of good times together both inside the department as well as outside. I am thankful to Gerard for all the tools you have shared with me. One can imagine any image/video tweaking tool and guess what? Gerard has it. Thanks to Frits for sharing his cool ideas and knowledge. It is good to know for the future BME students: if you are stuck, talk to these guys. I am sure they will have a solution or they will make one for you.

From TU Delft Emile has tremendously contributed to the MICA project and thus to my thesis. His relentless effort in manufacturing the transducers was the key to the success of the project. Henry and Edo also shared their expertise as and when required to expedite the success of the MICA project

Thank you to Gracia, Sharon and Mrs. Degenaar for helping me with all the administrative paperwork. A special thanks to Gracia for being so patient and answering all my queries.

Thank you to Ilya and Sophinèse for being wonderful colleagues and friends. I can almost write a book about my experience with them. I consider Ilya as my friend, philosopher, and guide. His personality and human qualities are unmatched. I feel blessed to have him as my roommate. Again Sophinèse is the definition of friendship for me. She can go beyond her limits to help anyone. Both of them were there with me for all the ups and downs during the last few years. I feel honoured to be a friend of both of them. I will miss their companions throughout the rest

of my life.

Jovana, Reza, Martin are the people with whom I had lots of fun. May it be a conference, may it be a summer school, we all enjoyed our companion and sense of humor. I would like to thank Jovana for being a wonderful colleague. I liked the discussions we had both technical and personal. With Martin, we re-discovered the true meaning of hope. I guess, if we both implement that mindset in our life none can defy our success. I would like to request Reza to keep on smiling and having the apple-lunch!

Thank you to Jason and Jena for being nice friends. Although my thesis was far from Jena's interest, Jena took the effort of correcting my thesis introduction. I really appreciate her effort and time. Jason is a wonderful colleague. We have spent hours inside and outside the department. I enjoyed your company a lot. Our trips to Maastricht and Tours are memorable. Hope we can do it again in future.

Thank you to Peter van Gelder for being my mentor in English writing. Hope I can continue writing manuscripts with the consciousness and confidence imbibed by him.

Jacopo, Tianshi, Alex, Zeynettin, Varya, Pieter are wonderful colleagues to work with. Although I had a small overlap with Mr. Italian (Jacopo), we had a wonderful time together in Rotterdam. Our reunion in Florence was also great. I will try to do it again. I missed Mr. German (Alex) a lot after he left to the US. There is no one left in the lab whom I can annoy to have fun. A special thanks to Pieter for his support with fast beamforming scripts. A big thanks to Varya for supporting the MICA project.

The work atmosphere would not have been so pleasant without Gijs, Min, Klazina, Ying, Ruoyu, big Tom, small Tom, Inés, and Kirby. They made each of my days enjoyable and productive with their smiles and cheerful attitudes. A special thanks to Klazina for supplying plants from her parents. At times those plants were more productive than me. I had experienced the sense of fulfillment and success by nurturing them. Many many thanks to Mom Min for taking good care of us in Taiwan. Because of her we all were nourished well there and came back safe and sound. Without Inés, I could have been in trouble at Tours. I want to thank her for hanging my poster at the right place. That was hilarious.

Thank you to Nikola and Franc from Oldelft for their help in understanding the adult TEE probe and further support to do the experimentation with it.

Thank you to Saikat, Thomas, Mahipal, Muthu, Jeremy, Arif, Jelle, Sourish and Raja for their stimulating companions. Words will never be enough to explain what these guys mean to me. In one sentence they made Rotterdam a second home for me. I feel extremely lucky to get the opportunity of having the acquaintance of Thomas, a sociologist, philanthropist and a friend. Our meetings were always charming and enthusiastic for both of us. With Thomas, I have spent

Acknowledgment

hours in discussing politics, society, philosophy, culture and lot more. These discussions opened up many different perspectives which I was not aware of before. My childhood buddy Saikat has never let me down in my life. He has been always supportive no matter what it cost to him. I am grateful to him forever. A special thanks goes to Mahipal and Muthu for being such wonderful friends. Our road-trips were miraculously rejuvenating.

I would also like to thank my friend Elise and her parents for their hospitality. In the last few years, I have visited them multiple times as I felt like meeting my family. Their contribution to my emotional health is immense.

Last but definitely not the least, I would like to thank Georgio Mosis, my former supervisor in Philips for his constant support and guidance throughout my carrier.

Summary of PhD training

PhD training	Date	ECTS
International Conference attendance		
19th European Symposium on Ultrasound Contrast Imaging, Rotterdam, The Netherlands	Jan 2014	0.6
Sense of Contact 16 - Making the World More Sensitive, Utrecht, The Netherlands	Apr 2014	0.3
2014 IEEE International Ultrasonics Symposium , Chicago, IL, USA	Oct 2014	1.2
20th European Symposium on Ultrasound Contrast Imaging, Rotterdam, The Netherlands	Jan 2015	0.6
ARTIMINO, Helsingborg, Sweden	Jun 2015	1.2
Conference on Functional Imaging and Modeling of the Heart, Maastricht, Netherlands	Jun 2015	0.9
2015 IEEE International Ultrasonics Symposium , Taipei, Taiwan	Oct 2015	1.2
21st European Symposium on Ultrasound Contrast Imaging, Rotterdam, The Netherlands	Jan 2016	0.6
2016 IEEE International Ultrasonics Symposium , Tours, France	Sep 2016	1.2
21st European Symposium on Ultrasound Contrast Imaging	Jan 2017	0.6
2017 Artimino, Artimino, Italy	Jun 2017	1.2
Courses		
PZFlex course at TUDelft	Oct 2013	1
MUT 2014 Summer School, Denmark Technical University	May 2014	3.5
Ultrafast Imaging in Biomedical Ultrasound: Principles and Applications, 2014 IEEE IUS	Oct 2014	0.15
COEUR: Cardiovascular imaging and diagnostic	Feb 2015	1.5
Summer School on Advanced Ultrasound Imaging, DTU	Jun 2016	2.5
Medical Transducers (with Electronics), 2015 IEEE IUS	Oct 2015	0.15
COEUR: English Biomedical Writing and Communication	Feb 2016	2
Ultrasonic Therapy: Mechanism, Methods, and Application, 2016 IEEE IUS	Sep 2016	0.15
Conference presentations		
Poster presentation-19th European Symposium on Ultrasound Contrast Imaging	Jan 2014	1
Poster presentation-2014 Sense of Contact 16	Apr 2014	1
Poster presentation-2014 IEEE International Ultrasonics Symposium	Oct 2014	1
Oral presentation- ARTIMINO, Helsingborg, Sweden	Jan 2015	1
Oral presentation-Dutch Society for Medical Ultrasound Autumn meeting, Leuven	Oct 2015	1

PhD Portfolio

Poster presentations-2015 IEEE International Ultrasonics Symposium	Oct 2015	2
Poster presentation-2016 IEEE International Ultrasonics Symposium	Sep 2016	1
Oral presentation-2017 ImPhys PhD meeting, Delft	Jan 2017	1
Oral presentation-2017 Artimino	Jun 2017	1
Research seminars		
Dutch Society for Medical Ultrasound Autumn meeting, Leuven	Oct 2015	0.15
Dutch Society for Medical Ultrasound Spring meeting, Rotterdam	Apr 2016	0.15
Echography: New recipe, better than ever! Nijmegen	Jun 2016	0.15
Dutch Society for Medical Ultrasound Spring meeting, Delft	May 2017	0.15
Total		31.15